

Lake Tahoe Clarity Analysis and Modeling Phase I: Biogeochemical and Ecological Modeling

Alicia Cortés, S. Geoffrey Schladow, Lidia Tanaka, Sean C. Trommer, Sergio A. Valbuena,
Shohei Watanabe
UC Davis Tahoe Environmental Research Center

John M. Melack
Earth Research Institute & Bren School of Environmental Science and Management, UC Santa Barbara

Sudeep Chandra, Erin K. Suenaga
Department of Biology, University of Nevada, Reno

Luciana De Souza Cardoso
Instituto de Biociencias, Universidad Federal do Rio Grande do Sul, Porto Alegre, RS, Brazil

August 17, 2022

Report Prepared for the Tahoe Science Advisory Council

Table of Contents

1. Background	4
1.1. Project Charge	4
1.2. Project tasks	4
2. Introduction	5
2.1. Site description.....	5
2.2. Modeling approaches.....	5
2.3. Organization of the report	6
3. Data description and availability	7
3.1. Stream data	7
3.2. Meteorological stations and thermistor chains	7
3.2.1. On-shore meteorological stations.....	7
3.2.2. Meteorological stations and thermistor chains on buoys.....	7
3.2.3. Thermistor chains.....	8
3.3. Physico-chemical parameters	8
3.3.1. Water sampling, CTD profiling, and clarity measurement	8
3.3.2. Laboratory analyses	8
3.3.2.1. TP and THP (Persulfate Digestion and Phosphomolybdate Method).....	8
3.3.2.2. TKN (Kjeldahl Digestion and Indophenol Method).....	9
3.3.2.3. NO ₃ + NO ₂	9
3.3.2.4. NH ₄ (Indophenol Method).....	9
3.3.2.5. SRP (Phosphomolybdate method)	9
3.3.2.6. Chlorophyll-a	9
3.4. Phytoplankton and primary productivity	10
3.5. Zooplankton densities	10
3.6. Data availability	10
4. Phytoplankton	11
4.1. Overview	11
4.2. Functional groups.....	11

4.3.	Phytoplankton abundance and biomass	12
4.4.	Physiological characteristics.....	13
4.5.	Phytoplankton Primary Productivity	13
5.	Zooplankton	16
5.1.	Overview	16
5.2.	Zooplankton density: Methods	17
5.3.	Literature review of model constants	17
5.3.1.	Direct values from the literature.....	19
5.3.2.	General regression models to obtain reasonable approximations	21
6.	One-Dimensional Model	23
6.1.	One-Dimensional Model Description	23
6.2.	1-D Model Improvements to the Lake Clarity Model for plankton food web model.....	23
6.2.1.	<i>Conversion and Expansion of Phytoplankton Model</i>	23
6.2.2.	<i>Addition of Zooplankton Model</i>	24
6.2.3.	<i>Addition of a Simple Phytoplankton Settling Model</i>	24
6.3.	Mechanistic Equations of the Plankton Food Web Model.....	24
6.3.1.	<i>Phytoplankton Model Equations</i>	24
6.4.	Use of the Lake Clarity Model to Develop the Plankton Food web Model	26
6.4.1.	<i>Calibration Strategy</i>	26
6.4.2.	<i>Key Calibration Parameters</i>	28
6.4.3.	<i>Limitations of Model Calibration</i>	28
6.4.4.	<i>Calibration Assessment</i>	28
6.4.5.	<i>Calibration Parameters</i>	29
6.4.6.	<i>Calibration Results</i>	30
6.4.7.	<i>Sensitivity Analysis of LCM with calibrated plankton food web model</i>	33
6.5.	Transitioning to 3D implementation	34
6.5.1.	<i>Atmospheric Nutrients and Groundwater Nutrients</i>	34
6.5.2.	<i>Stream Inflows and Nutrient Concentrations</i>	34
6.5.3.	<i>Optical-Model and Lake Clarity</i>	34
7.	Three-Dimensional Model.....	35
7.1.	Hydrodynamic Model.....	35
7.1.1.	Overview of the Numerical Model	35
7.1.2.	Model Simulation Periods	35

7.1.3.	Field Observations for Model Calibration and Validation	36
7.1.4.	Surface Boundary Condition, Initial Conditions, and Grid Size of the Numerical Model	37
7.1.5.	Statistical Metrics of Model Performance	38
7.1.6.	Calibration and Validation of the Model (Spring 2018)	39
7.2.	Biogeochemical and Ecological Model: PSi3D-AEM	47
7.2.1.	Overview of PSi3D-AEM	47
7.2.2.	Phytoplankton and Nutrient Dynamics: Conceptual Models, Equations & Parameters	48
7.2.2.1.	<i>Phytoplankton</i>	49
7.2.2.2.	<i>Carbon</i>	52
7.2.2.3.	<i>Nitrogen</i>	55
7.2.2.4.	<i>Phosphorus</i>	57
7.2.3.	Field measurements: Data for Initial Conditions and Calibration	59
7.2.3.1.	<i>Phytoplankton, Zooplankton and Carbon</i>	59
7.2.3.2.	<i>Nitrogen</i>	61
7.2.3.3.	<i>Phosphorus</i>	61
7.2.4.	Model results: Phytoplankton and Nutrients	62
7.2.5.	Model results: Developing Scenarios	72
8.	Conclusions	74
9.	Recommendations	75
9.1.	Data-related	75
9.2.	Model-related	77
10.	Appendix A: Literature review of physiological parameters of phytoplankton	79
11.	Appendix B: One-dimensional Model Results	85
12.	Appendix C: Three-dimensional Hydrodynamic Model Validation Scenarios	95
12.1.	Validation of Summer 2018	95
12.2.	Validation of Fall 2018	99
12.3.	Validation of Spring 2011	103
12.4.	Validation of Summer 2011	107
12.5.	Validation of Fall 2011	110
13.	Appendix D: Biogeochemical and ecological data available for Lake Tahoe	114
14.	Appendix E: PSi3D-AEM Model Results	120
15.	References	125

1. Background

1.1. Project Charge

The Lake Tahoe ‘Science to Action Plan’ (TSAC 2019) recommended several activities pertinent to clarity analysis and modeling. As articulated in the Science to Action Plan, considerable effort is needed to update and improve the Lake Clarity Model and related models of watershed inputs, and to conduct further data collection, data organization, and data analyses.

The project was explicitly charged to explore priority initiatives identified in recent model assessments by organizing relevant datasets, enhancing the ecological algorithms used in clarity modeling, linking those algorithms to a 3-D hydrodynamic modeling framework, and applying a separate empirical dynamic model to existing data to explore non-linear dynamic interactions.

1.2. Project tasks

- i. Data Management: Organizing relevant datasets
- ii. Ecological Model Refinement
 - Include phytoplankton functional groups in a carbon-based framework
 - Include multiple zooplankton groups (new foodweb model)
 - Evaluate the relative role of biological processes in determining lake clarity
- iii. Initial 3-D Model Development
 - Calibrate and validate a 3-D hydrodynamic model
 - Link ecological algorithms into 3-D hydrodynamic modeling framework
 - Integrating the clarity algorithms into 3-D framework
- iv. Empirical Dynamic Modeling

John M. Melack and Ethan R. Deyle. 2022. Lake Tahoe Clarity Analysis and Modeling: Empirical Dynamic Modeling. Separate report

2. Introduction

2.1. Site description

Lake Tahoe (39° N, 120° W) is a deep (501 m maximum depth, 313 mean depth), sub-alpine lake, situated at 1897 m asl on the border of California and Nevada, USA. The lake is warm-monomictic, meaning it does not freeze, and winter mixing only extends over the whole water column every 3-7 years (Sahoo et al. 2016). The lake's exceptional water clarity continues to be a key indicator of watershed and lake health.

Long-term monitoring has revealed that Secchi depth transparency has declined by approximately 10 m since the early 1960s and that primary productivity continues to increase (TERC 2021). Reductions in lake clarity are mainly driven by fine inorganic (sediments) and organic (phytoplankton) particles (Naranjo et al. 2022). This project is designed to improve understanding of clarity by revising and testing a simulation model of the lake's physical and ecological processes.

2.2. Modeling approaches

The application of numerical water quality models to evaluate aquatic management strategies is widely used for lakes, reservoirs, and coastal zones to provide both system understanding and a predictive tool for management to evaluate actions and future trends. A range of modeling approaches is available to evaluate aquatic ecosystems as summarized in Jorgensen and Bendoricchio (2001) and Mooji et al. (2011). For this project, we built upon the previous work at Lake Tahoe (see for example Losada (2001); Swift et al. 2006; Sahoo et al. 2011) as well as adopted more recent approaches from the literature.

We have implemented a coupled aquatic ecological model (AEM) to a parallelized three-dimensional (3D) hydrodynamic model (PSi3D) that we will refer to as PSi3D-AEM. The AEM component simulates the cycling of carbon (C), nitrogen (N), and phosphorus (P), and phytoplankton dynamics including shifts regulated by zooplankton grazing. For details about the 3D hydrodynamic model, refer to Section 7. The main features of the current version of PSi3D-AEM are:

- Phytoplankton are represented as particulate carbon
- Four phytoplankton functional groups, differentiated by cell size with particular attention to *Cyclotella* spp., are included:
 - o Group 1: Size < 2 µm (representative of picoplankton)
 - o Group 2: Size 2-6 µm (exemplified by *Cyclotella*)
 - o Group 3: Size 6-30 µm (exemplified by *Cryptomonas*)
 - o Group 4: Size > 30 µm (exemplified by *Synedra*)
- A Tahoe-specific grazing model driven by the zooplankton counts for those years when data existed for Lake Tahoe and literature-based grazing rates.

Due to the paucity of zooplankton data, plus the time limitations, the adopted approach was to model the hydrodynamics and ecology in two different years that represented two types of conditions: 1) 2011 had large inflows, cool surface temperatures, and full water column mixing; 2) 2018 had low inflows and only partial mixing (to a depth of 285 m), which likely contributed to the warm surface temperatures. The contrasts observed between the two years allowed for the evaluation of the performance of the numerical model under different conditions. To address the seasonality of Lake Tahoe's clarity, we separately simulated spring, summer, and fall. The three seasons allowed analyses of dynamics such as

spring/summer onset of stratification, lake mixing and fall thermocline deepening and sharpening. Calibration of the coupled hydrodynamic-ecological model was conducted for spring 2018. Validation of the hydrodynamic model was completed for the two years and three seasons.

2.3. Organization of the report

The report is organized as follows:

- Section 3: Data description and availability
- Section 4: Phytoplankton
- Section 5: Zooplankton
- Section 6: 1D Model
- Section 7: 3D Model
- Section 8: Conclusions
- Section 9: Recommendations
- Appendices and References

3. Data description and availability

3.1. Stream data

The United States Geological Survey (USGS) maintains stream gauges at seven streams flowing into Lake Tahoe: Incline Creek (1020), Third Creek (1030), Upper Truckee River (5010), Trout Creek (5050), General Creek (6010), Blackwood Creek (7010), and Ward Creek (8060). Stream discharge and water temperature are measured at 15 min intervals (Turnipseed and Sauer 2010, Wagner et al. 2006). Water samples are collected from Upper Truckee, Trout, General, Blackwood, and Ward creeks approximately 20 times per year, usually near peak flow during snowmelt or after rain events. Water samples are analyzed for total phosphorus (TP), soluble reactive phosphorus (SRP), total Kjeldahl nitrogen (TKN), nitrate (NO₃), and ammonium (NH₄) (Turnipseed and Sauer. 2010, Richard et al. 2006).

3.2. Meteorological stations and thermistor chains

3.2.1. On-shore meteorological stations

A meteorological monitoring station installed at the pier of the US Coast Guard (USCG) station, Tahoe City, collects air temperature and relative humidity (Campbell EE181), wind speed and wind direction (Campbell WIndSonic4), barometric pressure (Campbell CS100), shortwave and longwave radiation (Campbell NR01) at 10 min intervals. Five additional meteorological stations collecting wind speed and wind direction (Campbell WindSonic4), air temperature and relative humidity (Campbell HMP45c), precipitation (Campbell 52202), and barometric pressure (Campbell CS105) every 10 min are distributed around the basin (Table 3-1).

Table 3-1. Meteorological stations and measured variables. Air Temp = Air temperature, Wind Spd = Wind speed, Wind Dir = Wind direction, RH = Relative humidity, Precip = Precipitation, Atm Press = Atmospheric pressure, SW = Short waveradiation, and LW = Longwave radiation.

Station	Coordinates (°N,°W)	Variables							
		Air Temp	Wind Spd	Wind Dir	RH	Precip	Atm Press	SW	LW
USCG	39.181, -120.119	X	X	X	X	X	X	X	X
Cave Rock	39.044, -119.949	X	X	X	X	X	X		
Rubicon	39.010, -120.113	X	X	X	X				
Sunnyside	39.139, -120.153	X	X	X	X	X			
Tahoe Vista	39.237, -120.043	X	X	X	X	X			
Timber Cove	38.948, -119.967	X	X	X	X				

3.2.2. Meteorological stations and thermistor chains on buoys

NASA-JPL and TERC maintain four buoys on the lake. Each buoy is equipped with sensors measuring wind speed and wind direction (RM Young 05106), air temperature and relative humidity (RM Young 41382VC + 41003P), barometric pressure (RM Young 61302V + 61002), and water temperatures at 8 depths (0.5, 1.0, 1.5, 2.0, 3.0, 4.0, 5.0, and 5.5 m, using RBR XR-420 T8 thermistors; Table 3-2).

Table 3-2. List of buoys equipped with meteorological stations and thermistor chain

Buoy	Coordinates (°N,°W)
TB1	39.155, -120.004
TB2	39.110, -120.008
TB3	39.111, -120.073
TB4	39.155, -120.071

3.2.3. Thermistor chains

A thermistor chain, installed in the southeast of the lake where water depth exceeds 450 m (39.113, -119.977), has 13 thermistors (approximately at 5, 20, 25, 30, 40, 60, 80, 100, 120, 160, 200, 240, 280, 320, 360, 400, 440, and 460 m, using RBR Solo and TR-1060 thermistors) and a sensor (CTD; RBR Concerto) at the bottom. Thermistors record water temperature every 30 sec, and CTD records water temperature, pressure, conductivity, and dissolved oxygen every 10 min. The system was deployed in 2018 and was not in the lake from 2018-04-04 to 2018-04-09 and from 2018-10-29 to 2018-12-07 due to downloading and maintenance.

3.3. Physico-chemical parameters

3.3.1. Water sampling, CTD profiling, and clarity measurement

Routine limnological monitoring has been conducted in Lake Tahoe since the 1960s at the index station (LTP, approximately 150 m deep) and since the 1980s at the mid-lake station (MLTP, approximately 450 m deep). The index station is visited approximately every 13 days and the mid-lake station monthly. Water samples are collected from 13 depths (0, 2, 5, 10, 15, 20, 30, 40, 50, 60, 75, 90, and 105 m) at LTP site and 11 depths (0, 10, 50, 100, 150, 250, 300, 350, 400, and 450 m) at MLTP by a Van-Dorn sampler. Samples are transferred to 250 mL Nalgene HDPE bottles and stored on ice in an insulated container. Sub-samples are filtered through Whatman GF/C glass fiber filters (25 mm) within 1-3 hours of sample collection and stored at 4°C. Assays are performed within one week of sample collection.

Secchi depth is measured by lowering the 25 cm (10 inches) matte white disk from the shaded side of the boat. The depth where the disk disappears when lowering and re-appears when recovering is recorded and then averaged. Water temperature and conductivity profiles are taken with a Seabird CTD 25plus on each visit. The CTD instrument is also equipped with a photosynthetically available radiation (PAR) sensor. The diffuse attenuation coefficient of downward PAR ($K_d(PAR)$, m^{-1}) is calculated by regressing log-transformed PAR against depth.

3.3.2. Laboratory analyses

Raw water samples are analyzed for total phosphorus (TP) and total Kjeldahl Nitrogen (TKN). Filtered samples are analyzed for total hydrolysable phosphorus (THP), soluble reactive phosphorus (SRP), nitrate (NO_3+NO_2), and ammonium (NH_4).

3.3.2.1. TP and THP (Persulfate Digestion and Phosphomolybdate Method)

The unfiltered sample is digested with acid-persulfate that converts organic phosphorus and most particulate inorganic phosphorus to SRP and is referred to as TP. Acid hydrolysis caused by the reagents

used for the phosphomolybdate assay releases soluble orthophosphate from some inorganic and organic phosphorus compounds and is referred to as THP. The method is applicable for samples ranging from 0 – 500 µg/L. The method detection limit (MDL) is 2 µg/L. The precision of the 20 mL method (99% confidence intervals) is ±0.5 µg/L (Fishman and Friedmann 1985, Goldman 1974, Strickland and Parsons 1972, EPA 365.3).

3.3.2.2. TKN (Kjeldahl Digestion and Indophenol Method)

The unfiltered samples are heated in the presence of sulfuric acid for 2.5 hours, the residue cooled, diluted to 25 mL, and analyzed for ammonium with the indophenol method (see section 3.3.2.4). Total Kjeldahl nitrogen (TKN) is the sum of free-ammonia and organic nitrogen compounds. Organic Kjeldahl nitrogen is the difference between the free ammonia and the total Kjeldahl nitrogen. The detection limit is 40 µg/L for Kjeldahl N. Total nitrogen (TN) is obtained as the sum of TKN and $\text{NO}_3 + \text{NO}_2$ (Fishman and Friedman 1985, Liddicoat et al 1975, Solorzano 1969, EPA 351.2).

3.3.2.3. $\text{NO}_3 + \text{NO}_2$

The analysis method utilizes a hydrazine-copper solution that reduces nitrate to nitrite followed by color development using a diazotization-coupling reaction. The method assumes a 1:1 stoichiometric reduction of nitrate to nitrite. The total nitrite present is then measured. The method's detection limit is 2.0 µg/L; the precision is ± 0.3 µg/L (Kamphake et al 1967, Strickland and Parsons 1972).

3.3.2.4. NH_4 (Indophenol Method)

This method is a modification of the methods reported by Liddicoat et al.(1975), Solorzano (1969), and Brzezinski (1987). A blue indophenol reaction between ammonium, phenol, and hypochlorite takes place using potassium nitroferricyanide as a catalyst. The final concentration is reported as µg $\text{NH}_4\text{-N/L}$. Calcium and magnesium interference is eliminated by complexing with sodium citrate. Interferences include matrices with high concentrations of Ca^+ and Mg^+ , turbidity, and color in the samples that absorb in the photometric range being used. The method is applicable in the range from 0-500 µg/L $\text{NH}_4\text{-N}$ although it yields the best results on samples containing less than 50 µg/L. The method detection limit is 1.0 ± 0.3 µg/L. The precision of the 10 mL method (95% confidence intervals) is ±2 µg/L (Brzezinski 1987, Liddicoat et al 1975, Solorzano 1969, EPA 350.1).

3.3.2.5. SRP (Phosphomolybdate method)

Orthophosphorus is converted to a phosphomolybdate complex by acidified ammonium molybdate. When the phosphomolybdate complex is reduced with ascorbic acid in the presence of antimony, an intense blue complex develops. Concentrations are reported as µg $\text{PO}_4\text{-P/liter}$. The method is applicable in the range from 0-200 µg/L and the detection limit is 1.0 µg/L. The precision of the 30 mL method (99% confidence intervals) is ±0.6 µg/L (Murphy and Riley 1962, Greenberg 1995).

3.3.2.6. Chlorophyll-a

Water samples are collected with a Van-Dorn sampler, transferred to 250 mL Nalgene HDPE bottles, and stored on ice in an insulated container. 100 mL is filtered through Whatman GF/C glass fiber filters (25 mm) within 1-3 hours of sample collection. Filters are kept frozen until analysis. Pigments are extracted by methanol, and chlorophyll concentration is determined using a Turner Designs 10-AU fluorometer (a method currently being adapted for a Turner Trilogy fluorometer). The final concentration of chlorophyll-

a is determined by correcting for pheophytin by adding a small amount of hydrochloric acid (0.05 mL of 0.3 N HCl to 5 mL of extractant) to the sample and fluorescence remeasured after acidification. The detection limit is 0.05 ug/L +/- 1.4%. The fluorometer is calibrated annually with the use of *Anacystis nidulans* chlorophyll *a*.

3.4. Phytoplankton and primary productivity

See section 4.3.

3.5. Zooplankton densities

See section 5.2.

3.6. Data availability

Monitoring data used in the present work are publicly available with supporting documents. All stream data are downloadable from the National Water Information System, USGS (waterdata.usgs.gov). Onshore meteorological station data and other limnological data are temporarily available at a password-protected shared web folder (<https://ucdavis.box.com/v/2022-Tahoe3D>, pass: laketahoe3d). They will be permanently available through TERC's data portal on a public data sharing platform (Note: details will be provided once it is established - estimated end of summer 2022). Meteorological data and water temperature data collected at four buoys (TB 1-4) are available through NASA-JPL (web link will be provided once data are uploaded to JPL's data server - estimated to be completed by end of summer 2022).

4. Phytoplankton

4.1. Overview

The free-floating microalgae, or phytoplankton, are photosynthetic organisms that form the base of aquatic food webs by acting as the energy source for all higher trophic levels. Hence, phytoplankton play a key role in the function of aquatic systems and are a critical component in lake modeling studies. Further, in the context of the management of the Tahoe watershed, one of the major concerns revolves around the elucidation of the mechanisms driving phytoplankton dynamics in the lake, and the aim to better understand the extent of phytoplankton contribution to the variability of water clarity.

Phytoplankton are represented by many taxonomic groups and comprises a diverse assemblage of organisms in terms of size, shape, life cycle, physiology, growth form (unicellular/colonial), nutritional mode, and nutrient requirements, as well as edibility and nutritional value among other traits. Thus, they can be classified following different functional systems.

4.2. Functional groups

Among different traits and classifications, cell size is considered a ‘master trait’ – so-called because many physiological performances and morphometric features are regulated by cell/organism size (Litchman et al. 2010). For instance, phytoplankton size affects light-harvesting, nutrient uptake, growth rates, sinking properties, and grazing susceptibility, among others. Therefore, the concept of functional trait-based approach (Lavorel et al. 1997, McGill et al. 2006) focused on cell size provides a robust tool to distinguish planktonic community structure and species interactions. The intrinsic complexity of living organisms, however, poses challenges for modeling studies and requires several assumptions. These include aspects of diversity in growth form in natural phytoplankton communities. The model treats phytoplankton as single celled organisms and assumes that each algal species can be categorized within one size class, without regard to the ability of certain cells to form colonies of different sizes and shapes that allow individual taxa to cover a wide size spectrum.

Phytoplankton varies over several orders of magnitude from submicron species such as picoplankton that are smaller than 2 micrometers to diatoms measuring over one millimeter (Reynolds 1984). In our model, four phytoplankton cell size classes were assigned as functional groups according to their maximum linear dimensions (MLD) (Table 4-1). These ranges differ from the typical phytoplankton size classification, but they were adopted because we are particularly interested in exploring the fate of small size phytoplankton (2-6 μm) which is likely to affect Lake Tahoe’s clarity. The number of functional groups or species can readily be increased in the model, dependent on the questions being posed and on the availability of data on the characteristics of such groups and of their abundance in the water column.

Table 4-1. Size-based functional groups are used in the model based on their maximum linear dimensions (MLD). Each functional size group is characterized by one representative taxon from Lake Tahoe.

Group #	Size class	Representative taxa
1	MLD <2 μm	picoplankton*
2	MLD 2 – 6 μm	<i>Cyclotella</i>
3	MLD 6 – 30 μm	<i>Cryptomonas</i>
4	MLD >30 μm	<i>Synedra</i>

* Data were obtained from published work by Winder (2009) who reports a study conducted at the index Station in Lake Tahoe between 2006 and 2008.

4.3. Phytoplankton abundance and biomass

A subset of phytoplankton cell counts generated from discrete-depth collections taken from the index station (LTP) in 2011 and 2018 are used. Samples were taken monthly using a Van Dorn bottle. Aliquots of 100-mL collected at depths of 5, 20, 40, 60, 75, and 90 m were preserved with Lugol's solution for phytoplankton analysis. Phytoplankton data from the mid-lake station (MLTP) were not included in the model because only depth-integrated composite samples from the upper 150 m and between 150-450 m were collected for microscopic analysis.

Examination of preserved phytoplankton samples was conducted on an inverted light microscope (Zeiss Axio Observer A1, Germany) following Utermöhl technique (Utermöhl 1958, Hasle 1978). Phytoplankton was identified to the lowest possible taxonomic level (for groups with MLD > 2 µm). The counting unit was mostly single-celled individuals, but also filaments or colonies were measured, depending on the organization of the algae. Broken or dead cells (without protoplasm), as well as debris, were not counted, as per the adopted criterion for recording only viable (living) cells at the time of collection but were noted. Picoplankton (<2 µm diameter) were not quantified because other techniques, such as flow cytometry and epifluorescence microscopy, are needed for their reliable detection and enumeration.

Linear measurements of representative individuals were taken and biovolume calculations were performed using a set of equations based on equivalent geometric shapes. For some species, simple shapes such as a sphere, cylinder, elliptical, and cone were assigned, while for others it was necessary to assign two or more different geometric shapes for different parts of a cell, to obtain accurate biovolumes (Smayda 1978).

The numerical model developed in this project uses phytoplankton biomass expressed as units of carbon (µg/L). The biomass carbon was determined from recorded abundances (cell counts) of phytoplankton and calculated biovolumes. Conversion of the phytoplankton cell counts to carbon was based on species-specific cell volume (biovolume) using the following equation for freshwater algal species (Rocha and Duncan 1985):

$$\text{Phytoplankton Carbon } \left(\frac{\mu\text{g}}{\text{L}} \right) = \text{Cell count } \left(\frac{\text{cell}}{\text{L}} \right) \cdot [a \cdot \text{CellBiovolume } (\mu\text{m}^3)]^b \cdot 10^{-6} \left(\frac{\mu\text{g}}{\text{cell}} \right) \quad (4-1)$$

Here a and b are the coefficients of a regression whose values are 0.1204 and 1.051, respectively (Figure 4-1). Calculations were made either for the entire phytoplankton assemblage or as the contribution by functional groups.

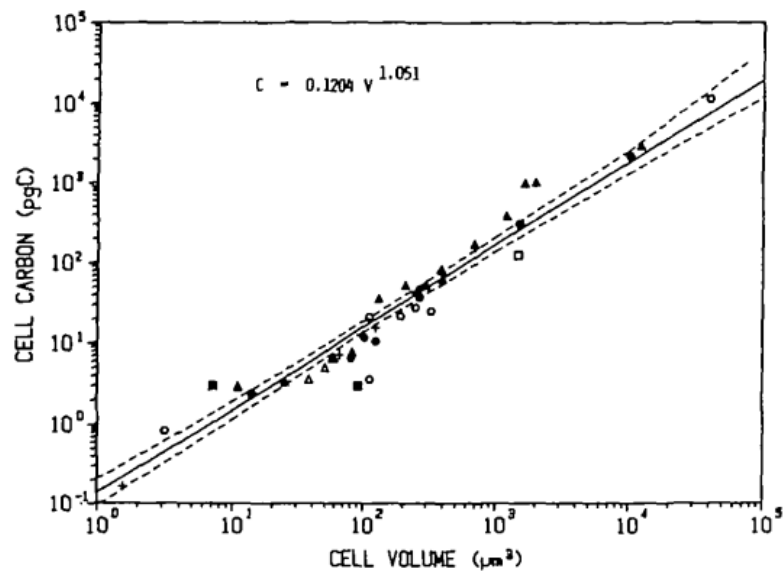


Figure 4-1. Relationship between cell carbon and cell volume of freshwater species of algae. For more details, see Figure 1 in Rocha and Duncan (1985).

4.4. Physiological characteristics

Physiological parameters of phytoplankton used in the model are based on data compiled from peer-reviewed literature, many of them established from laboratory culture. It is known that phytoplankton rarely performs in the natural environment as they do in culture. This approach was necessary due to the limited data available on physiological properties based on field observations, particularly for oligotrophic systems, such as Lake Tahoe.

Model constants and parameter values used in the model are given in Table 7-5 (section 7.2.2) and are derived from literature values, as summarized in Appendix A (section 10).

Phytoplankton Primary Productivity

Primary production (PPr) is the production of organic compounds from dissolved inorganic carbon (DIC) by photosynthesis. PPr varies with nutrient availability, light conditions, and water temperatures. In Lake Tahoe, PPr is measured as the rate of inorganic carbon uptake by phytoplankton using the radioisotope carbon-14 (^{14}C) as a tracer. To determine the PPr, the concentration of DIC in the water, the amount of ^{14}C -DIC added, and the amount of ^{14}C retained in particulate matter (^{14}C -POC) are required. PPr measures the rate of production during an incubation period, but not phytoplankton growth because carbon loss due to respiration during the nighttime is not included. Differences among algal species or taxonomic groups are not distinguished.

PPr measurements in Lake Tahoe have been made at least monthly since 1967 following methods described by Goldman (1963). Lake water is collected at the index station (LTP) from 13 depths that span the photic zone (0, 2, 5, 10, 15, 20, 30, 40, 50, 60, 75, 90 and 105 m). Lake water from each depth is transferred into two 125-mL clear glass reagent bottles (light bottles) and one opaque bottle (dark bottle). Dark bottles are included to determine non-photosynthetic carbon uptake. Each bottle is injected with 0.5 mL of approximately 10 $\mu\text{Ci/mL}$ activity ^{14}C in the form of sodium bicarbonate. The bottles are tightly

capped and returned to the lake at the depths from which the samples were collected for a 4-hour incubation period usually from 10:00 h to 14:00 h. They are then retrieved, and their contents filtered at low (10-15 mm Hg) vacuum pressure through HA Millipore membrane filters (0.45 µm pore size). The filters are air-dried for at least 24 hours, packed in labeled containers, and sent for counting with a Tennelec LB 5100 Series III Low Background Alpha/Beta/Gamma Planchet Counting System.

Once the data are collected, we follow a two-step calculation procedure:

1) Calculation of hourly rates of PPr

For each sample, PPr is calculated as follows:

$$PPR = \frac{{}^{14}C_{Assim} \times 1.06 \times {}^{12}C_{Avail} \times (10^3 L / m^3) \times Vol_{Bottle}}{{}^{14}C_{Added} \times (2.22 \times 10^6) \times Effic \times Hours_{Incub} \times Vol_{Filtered}} \quad (4-2)$$

Where,

PPr = primary productivity measured as carbon assimilation rate [mg C m⁻³ h⁻¹]

¹⁴C_{Assim} = ¹⁴C assimilated within each bottle (activity of filtered volume) [cpm or counts per minute]

¹²C_{Avail} = ¹²C available (concentration of DIC at respective depth) [mg C liter⁻¹]. A DIC value of 9.5 mg C/L is used.

1.06 = isotopic discrimination factor of ¹⁴C

¹⁴C_{Added} = ¹⁴C injected (ml) x relative activity [µmicro Curies/ml] = amount of ¹⁴C added per bottle [µCi]

2.22x10⁶ = factor used to convert µCi into disintegrations per minute [dpm]

Effic = Planchet counter efficiency (to convert ¹⁴C_{Assim} from counts per minute [cpm] to disintegrations per minute) [percent]. Reference sample for efficiency calculation is measured with each sample set.

Hours_{Incub} = duration of incubation period [hours].

Vol_{Bottle} = total volume of incubation bottle [ml].

Vol_{Filtered} = volume filtered [ml] (usually 125 mL).

2) Method for computing estimate of daily PPr

Each dark bottle value is subtracted from the average of the two light bottle values.

Measurements of hourly rates of PPr (mg C m⁻³ h⁻¹) at 13 discrete depths (0, 2, 5, 10, 15, 20, 30, 40, 50, 60, 75, 90, 105 m) are integrated over depth using linear interpolation to derive an estimate of hourly PPr for a water column extending from 0 m to 105 m.

Values can also be considered on a volumetric basis for each depth individually (mg C m⁻³ h⁻¹).

The integrated total hourly PPr (mg C m⁻² h⁻¹) is then scaled upward to reflect the total daily PPr (mg C m⁻² d⁻¹) as follows:

$$PPR_{day} = PPR_{hour} * (h_{inc}) * (s_{day} / s_{inc}) \quad (4-3)$$

Here,

PPR_{day} = daily PPr (mg m⁻² d⁻¹)

PPR_{hour} = hourly PPr (mg C m⁻² h⁻¹)

h_{inc} = number of hours during the incubation period

s_{day} = total solar insolation during the day

s_{inc} = total solar insolation during the incubation period

Solar radiation data are collected at the meteorological station located on the Tahoe City US Coast Guard Station pier. Total global or diffuse sky, solar radiation is measured using a high-precision Kipp & Zonen CM21 pyranometer sensor (radiant-flux, 305-2800 nm waveband, 10-min averages in units of Watt/m^2).

5. Zooplankton

5.1. Overview

In Lake Tahoe, there is considerable knowledge about particle sizes and distributions, the contribution of the size of the particles which contribute to the clarity, the phytoplankton community composition, and the rates of primary productivity within the water column. There are few recent publications about the zooplankton community and their effects on clarity with most studies from the 1970s and 1980s plus one in 2021. Despite the lack of information, there is some information from these Tahoe-focused studies and the literature from lakes or experiments with similar ecological conditions that can be used to provide an initial understanding of the influence of zooplankton on phytoplankton and particle grazing. In the following section, we review the literature for Lake Tahoe and selected relevant studies to incorporate food web (zooplankton to phytoplankton) dynamics into our model to understand what factors are influencing water clarity.

Lake Tahoe supports zooplankton populations at low density and few species with only one endemic species (*Capnia lacustra*). The typical seasonal patterns of zooplankton have larger abundances of copepods in the spring and summer, with cladocerans and rotifers becoming more prevalent in the fall and winter (Goldman 1981), and abundances fluctuate as environmental conditions change (Byron et al. 1984). The zooplankton community has been relatively consistent since the 1980s, after the introduction of *Mysis diluviana* (formerly *M. relicta*), and is currently dominated by the copepod species *Diaptomus tyrrelli* and *Epischura nevadensis*, and the rotifers *Kellicottia* spp., *Keratella* spp. and *Polyarthra* spp. (Winder & Hunter 2008; Winder et al. 2009).

The establishment of *Mysis* in Lake Tahoe, which occurred between 1969 and 1971, was the main factor that contributed to the disappearance of the cladocerans *Daphnia pulicaria*, *D. rosea*, and *Bosmina longirostris* from the pelagic community in 1970-1971 (Threlkeld et al. 1980) documented by Goldman (1974) and Richards et al. (1975). Since the decline of cladocerans, mean annual zooplankton densities have generally been inversely related to *Mysis* density, suggesting the importance of *Mysis* predation in the regulation of non-cladoceran zooplankton population dynamics as well (*Epischura nevadensis*, *Diaptomus tyrrelli*, and *Kellicottia longispina*). The remains of non-cladoceran zooplankton have been observed in *Mysis* stomach contents collected from the lake (Threlkeld et al. 1980). Regular *Mysis* monitoring was discontinued in 1995 but resumed in 2012.

Zooplankton species in Lake Tahoe have different grazing rates depending on the species, size, foraging behavior, and competitive interactions. Zooplankton are food-limited, and grazing rates will vary with phytoplankton productivity and abundance (Folt 1982, Byron et al. 1986, Elser et al. 1990, Elser and Goldman 1991, Bess et al. 2021). Grazing rates by copepods vary over time, and these rates are altered by interspecific competition (Folt et al. 1981). The observed pulses of small cladocerans (*Bosmina*) may have impacts on particles and algal biomass during periods when they occur (Byron et al. 1984). The ciliate and rotifer communities of Lake Tahoe are not well documented due to the zooplankton collection methods used. The role of native *Daphnia* in the low productivity waters of Lake Tahoe compared to their influence in neighboring Emerald Bay has been debated within the Tahoe scientific community. Recent measurements of *Mysis* and zooplankton were made in Emerald Bay between 2011 and 2017. During the first four years of that period when *Mysis* was absent, cladocerans reached densities approaching their pre-*Mysis* values, and the clarity in Emerald Bay increased by 10 m, exceeding the clarity in Lake Tahoe (Schladow et al. 2018). Dynamics of native zooplankton and interactions with *Mysis* have yet to be tested, aside from correlations within field data and experiments by Bess et al. (2021).

5.2. Zooplankton density: Methods

The zooplankton samples were collected monthly with a 0.75 m diameter net of 80 µm mesh size and equipped with a TSK flowmeter for calibration, at the index station (LTP) during 2011 and 2018. Samples were preserved in sucrose formalin substituted by ethanol after counting. At each sampling station, vertical net tows were made from 150 m to the surface. Zooplankton densities were expressed on a cubic meter after all collections had been standardized for calibrated filtration efficiency, net size, and tow depth. The filtrated water volume was calculated by coefficient between different flow-meter readings (before and after collecting the sample) (APHA, 1998).

Adults within the zooplankton samples were enumerated into species, and copepods were enumerated by sex and life stages (juvenile, copepodite, nauplii). For each sample, at least 500 individuals of the major taxonomic group were counted (USEPA, 2003). Copepods and cladocerans were examined using a plexiglass Ward's counting wheel in aliquots under a stereoscopic microscope. Rotifers and nauplii were examined in two equal volume sub-samples under a compound microscope Sedgwick-Rafter counting cells. Adult calanoids were identified according to Balcer et al. (1984). Cladocerans were classified according to Brooks (1959) and De Melo & Hebert (1994). Rotifers were identified using Koste (1978).

Mysis were collected using a 0.75 m diameter net with a 500 µm mesh. Samples were preserved in 10% sucrose buffered formalin. Replicate vertical tows were collected at each site. Vertical net tows were made from 100 m to the surface at the LTP site and from 200 m to the surface at MLTP and south shore site (Table 5-1). *Mysis* were collected between one hour after dusk when they enter the upper water column to feed and one hour before dawn as they migrate to deeper depths.

Table 5-1. List of sites and GPS coordinates where *Mysis* were collected in Lake Tahoe

Site	GPS coordinates
Mid-lake station (MLTP)	039 07 52 N; 120 00 10 W
Index station (LTP)	039 07 18 N; 120 04 39 W
South Shore	038 57 32 N; 120 00 31 W
Emerald Bay	038 57 18 N; 120 05 50 W

Mysis densities were expressed on a per square-meter basis by aggregating the total number of individuals and dividing by the net area. *Mysis* body length was determined by measuring from the tip of the rostrum to the cleft in the telson under a dissecting microscope fitted with a calibrated ocular micrometer. Individuals were identified as male if an extra-long fourth pleopod was present (Morgan and Beeton 1978). All *Mysis* in both replicate samples were enumerated and measured. Zooplankton densities were expressed on a per cubic-meter basis after all collections have been standardized for calibrated filtration efficiency, net size, and tow depth. The filtrated water volume was calculated by coefficient between difference flow-meter readings and revolutions (See APHA).

5.3. Literature review of modeled processes

Estimations of grazing for each taxon are based on the following strategies:

1. Grazing on three particle sizes (5 µm or less, 5-30 µm, and 30 µm or larger) (Figure 5-1). The bins were selected to accommodate particle sizes known to contribute to the lake's clarity decline (e.g. 6 µm or less), while also accounting for the dominant sizes that zooplankton can graze, and to allow for

efficient computational time of the model since evaluating many grazing combinations slows the computational time of the model. Previous laboratory studies indicate that *Daphnia* and copepods can ingest smaller particles (6 μm or less) with high concentrations of particles in the water, but the dominant grazing is on larger particles.

2. Grazing estimates were determined from Tahoe-specific studies where possible, and when local estimates were not available, we used published literature from other oligotrophic ecosystems with similar taxa, or experiments using taxa of similar size. Zooplankton body size has been shown to have scale-dependent influences on grazing and excretion estimations (Peters 1975). Understanding Lake Tahoe's clarity would benefit from targeted studies using Tahoe waters and plankton.
3. Grazing rates were determined for three modeled periods: spring, summer, and fall.

Assumptions are associated with the rates used for our model. Zooplankton distribution is patchy in Lake Tahoe (Folt & Shulze 1993, Bürgi et al. 1993), but we are assuming an even distribution of zooplankton across the pelagic and littoral zones of the lake. We do not account for diel vertical or horizontal movements. Diel movements have not been quantified in Lake Tahoe, except for vertical-horizontal movements of mysids, and would be an important focus of future studies along with experiments or models to understand community and species level growth and grazing influences around the lake.

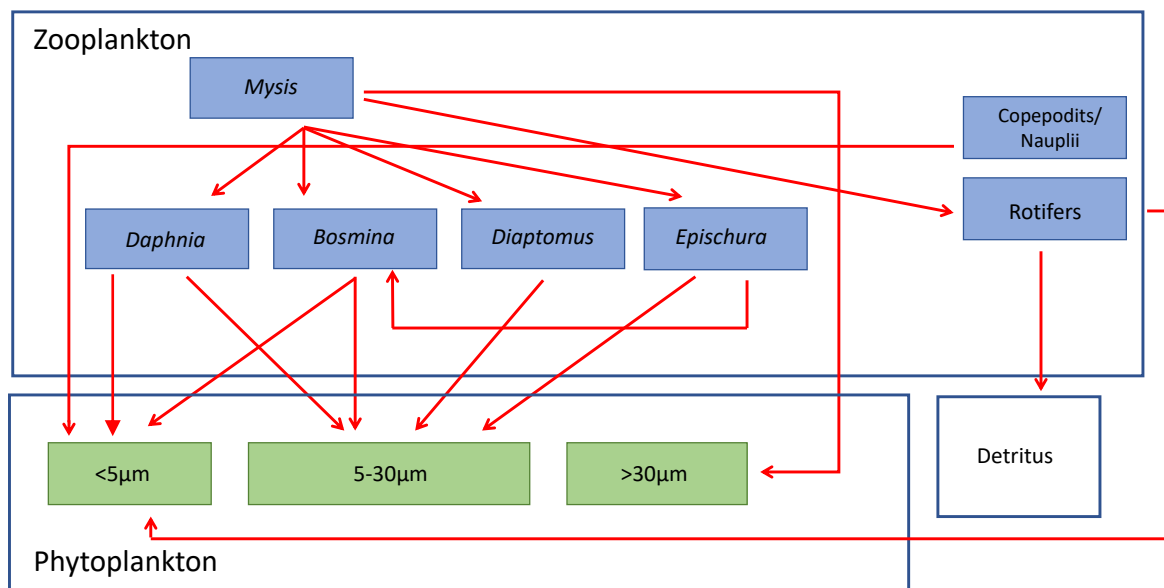


Figure 5-1. Zooplankton food web connection to particle size classes in Lake Tahoe.

Table 5-2. Grazing rates, respiration rates, and excretion rates taken from the literature for zooplankton taxa in Lake Tahoe.

Taxa	Season	Grazing rates [$\mu\text{g C indv}^{-1} \text{ day}^{-1}$]			Respiration rate [$\mu\text{g O}_2 \text{ indv}^{-1} \text{ day}^{-1}$]	Excretion rate [$\mu\text{g N indv}^{-1} \text{ day}^{-1}$]
		< 5 μm	5-30 μm	> 30 μm		
<i>Epischura</i>	Spring		0.014		1.6	0.07
	Summer		0.15			
	Fall		0.07			
<i>Diaptomus</i>	Spring		0.06		0.8	0.04
	Summer		0.3			
	Fall		0.32			
<i>Daphnia</i>	Spring	To be determined	0.046		0.5	0.1
	Summer		0.046			
	Fall		0.046			
<i>Bosmina</i>	Spring	0.005	0.005		0.16	0.04
	Summer	0.005	0.005			
	Fall	0.005	0.005			
<i>Kellicottia</i>	Spring	3.936×10^{-4}	2.035×10^{-3}	1.96×10^{-3}	N/A	3.920e-06
	Summer	3.936×10^{-4}	2.035×10^{-3}	1.96×10^{-3}		
	Fall	3.936×10^{-4}	2.035×10^{-3}	1.96×10^{-3}		

5.3.1. Direct values from the literature

Diaptomus tyrelli and *Epischura nevadensis* are the dominant component of the zooplankton community in Lake Tahoe, along with rotifers (Goldman 1981, Byron et al. 1984). The abundance of *Epischura* in Lake Tahoe is highest in June through August, and the abundance of all instars declines in September-October (Folt 1982). *Epischura* adults are predaceous during the summer when nauplii abundance is high, and maximum filtering rates were measured during the winter months (Folt 1982). Algal ingestion rates for adults are 0.8 $\mu\text{g C}$ per animal per day at most and is most likely subsidized by predation on nauplii and *Kellicottia* (Folt 1982). *Diaptomus* filtering rates are seasonal, and *Diaptomus* filter at a greater rate than *Epischura* (Folt 1982). *Diaptomus* filtering rates increased during warmer, summer months, but their population declines in the fall resulting in a decrease in filtering and ingestion rates. In Tahoe, *Diaptomus* are food-limited (Folt 1982).

Grazing rates on phytoplankton by *Epischura* and *Diaptomus* were determined using rates ($\mu\text{g C individual}^{-1} \text{ day}^{-1}$) measured by Folt (1982) from August 1979 to October 1980. Folt conducted experiments using natural assemblages of lake seston inoculated with radioactively labeled phosphorus-32, and after a set feeding period, individual zooplankton were heat-killed and measured for radioactivity. Zooplankton were assumed to filter at a constant rate. Correction factors were applied to grazing rates to account for an underestimation in filtering rate from inedible particles in the natural assemblage used and to account for filtering rates at depths corresponding to specific temperatures in the epilimnion.

Predation rate by *Epischura* on nauplii was determined using data from Folt (1982) and converted to number of nauplii $\text{individual}^{-1} \text{ day}^{-1}$. Rates were averaged for prey densities of less than 5 [prey $\text{predator}^{-1} \text{ liter}^{-1}$] and 5 or more [prey $\text{predator}^{-1} \text{ liter}^{-1}$] and applied to seasons depending on densities in Lake Tahoe. In the spring and fall, *Epischura* predation rate on nauplii is 1.52 [prey $\text{individual}^{-1} \text{ day}^{-1}$], and in the summer it is 0.41 [prey $\text{individual}^{-1} \text{ day}^{-1}$].

The grazing rate for copepod nauplii in Tahoe was determined from measurements of natural assemblages of marine copepod nauplii by Uitto (1996) in the northern Baltic. Very limited literature exists on grazing, excretion, and respiration rates of nauplii in freshwater systems. Since nauplii are numerically dominant in the ecosystem, a Tahoe focused understanding of nauplii dynamics including population changes, particle grazing, and interactions with the microbial community is warranted.

Cladoceran zooplankton populations in Lake Tahoe have fluctuated since the introduction of *Mysis relicta* in the 1960s, with disappearance of all pelagic cladocerans in 1970 (Byron et al. 1986). Reappearances of *Daphnia* and *Bosmina* have been observed in years with high primary productivity (Goldman 1985, 1986). In the years of interest for this model, 2011 and 2018, *Daphnia* and *Bosmina* were not found in the pelagic region of the lake.

Ability of *Daphnia rosea* and *D. pulicaria* to influence phytoplankton depends on trophic status, with these taxa generally serving as less effective grazers on phytoplankton in oligotrophic ecosystems due to their indiscriminate filter-feeding strategies and limited ability to consume phytoplankton in low densities (DeMott et al. 1982). *Daphnia* spp. have been observed in embayments and nearshore areas of Lake Tahoe where productivity is presumably higher than offshore. Though there are many site-specific studies about *Daphnia* feeding, few published studies have examined the role of *Daphnia* in Tahoe waters. *Daphnia* filtering and feeding rates are dependent on the food particle concentrations, temperature, and the size of *Daphnia* (Burns 1969). Experiments support the ‘mesotrophic maximum hypothesis’ which suggests lower feeding impacts of *Daphnia* in Tahoe waters compared to lakes with more phytoplankton (Elser and Goldman 1991, Bess et al. 2021). The size of *Daphnia* in Emerald Bay, which we assume is the same size that can be found in Tahoe is 1.1 ± 0.16 mm (Bess et al. 2021). We used this size of *Daphnia* to develop estimations for filtration rates using a study of *D. rosea* by Burns and Rigler (1967). However, since there were no *Daphnia* during the years we modeled, the grazing estimations are zero.

Bosmina spp. are small cladocerans that currently exist primarily in Emerald Bay of Lake Tahoe, but also reappear in pulses in the pelagic zone of the main lake with increases in primary productivity and decreased predation by *Epischura nevadensis* (Byron et al. 1984) and *Mysis diluviana* (Cooper & Goldman 1980). Unlike *Daphnia*, *Bosmina* spp. have been able to persist in Lake Tahoe at low abundances. *Bosmina* has been observed to feed at rates 1.6-4.8 times higher than *Daphnia* (DeMott et al. 1982).

The grazing rate for *Bosmina* was calculated from the filtering rate, $0.45 \text{ [mL individual}^{-1} \text{ day}^{-1}]$, measured on individuals from Lake Michigan (Jorgensen 1979). *Bosmina* prefers to feed on particles $>30 \text{ }\mu\text{m}$ in length (Bleiwas & Stokes, 1985). According to the phytoplankton measurements in Lake Tahoe, approximately $11 \text{ }\mu\text{gC L}^{-1}$ of phytoplankton occur in the size preference of *Bosmina*; therefore, multiplying the filtering rate by carbon concentration produces a grazing rate:

$$\begin{aligned}\text{Grazing rate} &= 0.45 \text{ mL individual}^{-1} \text{ day}^{-1} * 0.011 \mu\text{gC mL} \\ &= 0.00495 \mu\text{gC individual}^{-1} \text{ day}^{-1}\end{aligned}$$

In a study using adult Lake Tahoe *Mysis* ranging from 15 to 16.2 millimeters in length, Cooper and Goldman (1980) calculated the prey preferences of *Mysis*. The study found that each *Mysis* consumed a mean of 1 *Bosmina* day^{-1} , 3.5 *Daphnia* day^{-1} , 2.5 *Epischura* day^{-1} , 0.25 *Diaptomus* day^{-1} , and 0.5 *Kellicottia* day^{-1} . Therefore, the prey preferences ranked as follows: *Daphnia* > *Epischura* > *Bosmina* > *Kellicottia* > *Diaptomus*. These findings indicate that *Mysis* was effective at extirpating *Daphnia* from Lake Tahoe despite having a less pronounced effect on the other zooplankton taxa in the lake (Richards et al. 1975;

Goldman et al. 1979). Cooper and Goldman (1980) attributed the limited preference for *Diaptomus* to the agility and predator avoidance of *Diaptomus*. However, this finding may just reflect the inability of *Mysis* to see red light (Beeton 1959) and, consequently, its limited ability to prey on red zooplankton.

In a study by Bowers and Grossnickle (1978), laboratory mysids were fed resuspended phytoplankton to determine the selectivity of *Mysis* grazing. The study found that for algae smaller than 53 μm in diameter, pre-trial and post-trial chlorophyll-*a* concentrations did not differ. This suggests that mysids are not able to filter phytoplankton with diameters smaller than 53 μm . We have applied the grazing rate of larger phytoplankton to the largest size bin in this model. Additionally, Sierszen and Brooks (1982) measured the ingestion of ^{14}C -labeled *Staurosirella pinnata* (formerly *Fragilaria pinnata*) from Lake Michigan by *Mysis* in the laboratory. This study found that *Mysis* ingested 0.39 [$\mu\text{g mg-dry-weight-of-mysid}^{-1} \text{ hr}^{-1}$]. In foregut analyses of *Mysis* from the Baltic Sea, Lehtiniemi and colleagues (2009) found that detritus accounted for 18% of the volume of ingested contents.

Using mysids ranging from 20 to 30 millimeters collected from the Gulf of Finland, Linden & Kuosa (2004) found that mysids excreted $4.5 \pm 0.7 \text{ nmol SRP hr}^{-1}$ and $123.6 \pm 31.6 \text{ nmol ammonium hr}^{-1}$.

Filtering rates for *Kellicottia* were determined using rates estimated by Ross and Munawar (1980) in an *in situ* experiment conducted in the Burlington Canal, Lake Ontario. Ross and Munawar found that *Kellicottia longispina* preferred smaller-sized plankton (1-20 μm), with 94% of ingested particles in this size range. This experiment excluded phytoplankton larger than 64 μm since Ross and Duthie (1978) showed that these were not eaten by herbivorous zooplankton. Rotifers are assumed to filter at a constant rate.

Filtering rates were then converted to a carbon-based grazing rate by multiplying the filtering rate by the *in situ* estimates of phytoplankton carbon in Tahoe within the preferred size range of *Kellicottia*:

0-6 μm size filtering rate is 8.2 cells individual $^{-1} \text{ min}^{-1}$

6-30 μm size filtering rate is 3.7 cells individual $^{-1} \text{ min}^{-1}$

>30 μm size filtering rate is 0.7 cells individual $^{-1} \text{ min}^{-1}$

We calculated that there are approximately 1 $\mu\text{g C L}^{-1}$ of cells 2-6 μm in size and 10 $\mu\text{g C L}^{-1}$ of cells 6-30 μm in size in Lake Tahoe. These values were used to convert *Kellicottia* grazing rates into units of carbon for use in the model.

5.3.2. General regression models to obtain reasonable approximations

The respiration rates for *Epischura* and *Diaptomus* were estimated using regression equations for calanoid copepods found in Mauchline (1998):

$$\log R = 0.787 \log W + 0.245$$

where R is respiration rate in $\mu\text{g O}_2 \text{ indv}^{-1} \text{ hour}^{-1}$ and W is the dry weight in milligrams. The equation describing respirations rate was determined using data (n=31) from Ikeda (1974, 1978) and Marshall (1973) for calanoid copepods in temperate regions (temperature range of 11.7°C-17.5°C). The dry weight of *Epischura nevadensis* was measured by Bess (2021) as 0.01607 mg individual $^{-1}$ and the dry weight of *Diaptomus tyrelli* was 0.00696 mg individual $^{-1}$, which is an average weight from regressions by McCauley (1984). Copepod respiration increases by 6.7% per °C increase in temperature (Heine et al. 2019). This meta-analysis included 32 studies and included 50 copepod species from three orders.

Excretion rates of nitrogen for *Epischura* and *Diaptomus* were estimated using regression equations for calanoid copepods found in Mauchline (1998). The equation describing excretion rates was calculated from data from Ikeda (1974) in boreal ecosystems (n=28).

$$\log E = 0.644 \log W - 1.395$$

where R is respiration rate in [$\mu\text{g N indv}^{-1} \text{ hour}^{-1}$] and W is the dry weight in milligrams.

The following equation was taken from Yurista (1999) to calculate respiration rates of *Daphnia* and *Bosmina* relative to dry weight and temperature (Kelvin):

$$R = (\text{Temperature} * e^{(6735(1/289 - 1/\text{Temperature}))} * 0.0000573 * W^{0.816}) / (1 + e^{-39639/(0.003642 - 1/\text{Temperature})} + e^{65296/(0.003247 - 1/\text{Temperature})})$$

Where R is respiration rate in $\mu\text{g O}_2$ per hour, the temperature is in Kelvin, and W is dry weight of the organism in micrograms. We used a water temperature of 278.15°K (5°C) and a dry weight 0.00456 mg. This equation was developed using experiments with *Daphnia*, but due to limited literature on *Bosmina*-specific respiration rates, we applied it to this group as well. The equation is weight-based, hence appropriate to use on a smaller cladoceran species.

The excretion rates for *Daphnia* and *Bosmina* were taken from Wen and Peters (1994). The models defining excretion were constructed using marine and freshwater crustacean zooplankton data. The model describing nitrogen excretion of zooplankton using body weight explained 72% of the variation and the regression was highly significant ($p < 0.001$).

$$\log E_n = -1.38 + 0.67 \log W$$

T is the temperature in Celsius and W is weight in μg .

The following is a relationship between mysid respiration and water temperature based on bioenergetics equations for *Mysis* provided in Rudstam (1989):

$$W = 5.926 * D^{0.83}$$

$$R = 0.00182 * W^{-0.161} * e^{0.0752 * T}$$

where W is wet weight in grams, D is dry weight in grams, T is temperature in Celsius, and R is respiration rate in [$\text{grams O}_2 \text{ individual}^{-1} \text{ day}^{-1}$].

In a laboratory experiment, Boscarino et al. (2010) examined *Mysis* temperature preferences using a water column with a vertical temperature gradient. The study found that *Mysis* congregated mostly at 6 °C. Furthermore, *Mysis* did not migrate into water with temperatures less than 3 °C or greater than 14 °C. This suggests that these are the minimum and maximum temperatures that the species prefers.

The excretion rate for *Kellicottia* was taken from Wen and Peters (1994). The models for excretion were constructed using marine and freshwater crustacean zooplankton data. The model describing nitrogen excretion of zooplankton using body weight explained 72% of the variation and the regression was highly significant ($p < 0.001$).

$\log E_n = -1.38 + 0.67 \log W$, where T is the temperature in Celsius and W is weight in μg .

6. One-Dimensional Model

One challenge with developing the 3-D model was the number of parameters that were unknown or unconstrained. To address this, a one-dimensional (1-D) model, DLM-WQ, was used to take advantage of its far lower computational time to develop and calibrate the new sub-models before incorporating them into the 3-D model. However, even with the computational benefits of using a 1-D model to determine a viable set of parameters, the process of assigning values to the multiple parameters (or calibration) is time consuming and will need to be repeated as modeling develops. The complexity comes from the need to assign values to thirty model parameters (ten for each phytoplankton group) that control the phytoplankton dynamics driven by growth, mortality, and grazing. In this section, we described the model, the calibration strategy and the model results obtained both from a sensitivity analysis and the calibration of the 1-D model.

6.1. One-Dimensional Model Description

We utilized the Lake Clarity Model (LCM) developed by Sahoo et al. (2010) as a physical and chemical foundation for testing of parameters and further implement the new plankton food web model. The hydrodynamic component of the model is based on DYRESM model (Imberger et al. 1978; Yeates and Imberger 2003), with further modifications conducted in recent decades. DLM uses a hydrodynamic-thermal model that parameterizes the individual transport and mixing processes in a lake and predicts the lake's density structure over time. Fleenor (2001) modified the hydrodynamic module by adding river plunging algorithms. The hydrodynamic model is one-dimensional using horizontally homogeneous Lagrangian layers (Hamilton and Schladow 1997); however, the treatment of stream inflows and mixing due to stream entrainment at the river mouth is two-dimensional. Thus, the combination of the relevant physics makes the model quasi-two-dimensional. The assumption of one-dimensionality means that variations in density, temperature, and water quality parameters in the lateral directions are assumed to be small when compared with variations in vertical directions. Hamilton and Schladow (1997) combined the ecological sub-model and water quality sub-model that described the numerical description of phytoplankton production, nutrient cycling, the oxygen budget, and particle dynamics with DYRESM. Perez-Losada (2001) refined the ecological modules. An optical module was incorporated in DLM-WQ to estimate Secchi depth based on scattering and absorption characteristics of particles, algae, colored dissolved organic matter (CDOM), and water itself (Swift 2004, Swift et al. 2006). The ecological models were further refined during 2004-2007 as part of the Lake Tahoe TMDL development (Sahoo et al. 2010).

6.2. 1-D Model Improvements to the Lake Clarity Model for plankton food web model

The phytoplankton model in LCM has been expanded to simulate four groups of phytoplankton classified by size, as described in section 4. Additionally, the model can simulate additional groups. Two groups of particular concern that are not incorporated in the current version are bacteria, a diverse assemblage, which play an important role in nutrient cycling, and picoplankton, which are a concern for both nutrient cycling and are a potential cause of lower water clarity as surface waters warm (Winder et. al. 2008).

6.2.1. *Conversion and Expansion of Phytoplankton Model*

The expanded phytoplankton model has been changed from being based on chlorophyll *a* concentration to be based on particulate carbon concentrations. This change has not modified the mechanistic equations of DLM's phytoplankton model since the processes that govern phytoplankton population dynamics. The

transition replaced the parameters of the model with new values that reproduced phytoplankton levels observed from discrete sampling while remaining in realistic parameter ranges. Initially, the plan was to use parameter values for the representative species identified in section 4.2, however, the literature review for relevant values for the mechanistic equations did not find enough values for these species in similar systems. Therefore, the model was run iteratively with manual adjustment to determine values for the key parameters that produced stable populations for the phytoplankton groups. Here stable refers to populations that do not disappear or increase excessively, depleting the nutrient pool available. These values are listed in section 6.4.1.

6.2.2. Addition of Zooplankton Model

A zooplankton grazing model was added to LCM to represent the dynamic effect of grazing on phytoplankton. This zooplankton model allows for grazing by seven categories of zooplankton on the four simulated phytoplankton groups. The model uses as an input daily concentration of zooplankton collected during monthly, 150-meter sampling trawls with values between trawls interpolated using MATLAB's shape preserving interpolation function. These values are then distributed uniformly across the upper 150 m of the water column – the tacit assumption is that the zooplankton are uniformly present across the upper 150 m of the lake. The amount of grazing by each group is determined by a combination of the abundance of each zooplankton group, grazing rates described in section 5.3 and shown in table 7-4, and an assumed set of preference factor to account for selective grazing between multiple phytoplankton groups. Due to the large uncertainty in the vertical distribution of zooplankton, the grazing rates were held constant during modeling except during the sensitivity analysis.

6.2.3. Addition of a Simple Phytoplankton Settling Model

A settling function was included in the updated model. The settling function uses a supplied settling rate and the width of each layer in LCM to determine what percentage of phytoplankton in each layer will settle into the layer below at each timestep.

6.3. Mechanistic Equations of the Plankton Food Web Model

The equations and parameters described below are adapted from the following sources: Hamilton and Schladow (1997); Losada (2001); Swift et al. (2006); Trommer et al. (2019), and Hipsey et al. (2019). A similar set of equations and parameters can be found in section 7.2.2.1 for the Si3D-AED equivalents.

6.3.1. Phytoplankton Model Equations

Phytoplankton biomass is represented as particulate carbon (PhytoC, µg/L), and we currently model four phytoplankton functional groups arranged by cell size: (1) size < 2 µm (picoplankton); (2) size 2-6 µm; (3) size 6-30 µm; (4) size > 30 µm. For each phytoplankton group, the source-sink equation that models the rate of change of phytoplankton carbon concentration ($d[\text{PhytoC}]/dt$) includes four processes: growth (source), mortality, settling and grazing (sinks).

$$\frac{d[\text{PhytoC}]}{dt} = \text{Growth} - \text{Mortality} - \text{Grazing} - \text{Settling} \quad (6-1)$$

Phytoplankton Growth: The rate of change of phytoplankton biomass (*Growth*) is proportional to the phytoplankton biomass in the previous time step (*PhytoC*) and the product of a series of constants. The

daily maximum potential growth (μ_{max}) rate is multiplied by a temperature function (f_T) and the minimum value of expressions for limitation by light (f_L), nitrogen (f_N), and phosphorus (f_P), as follows,

$$Growth \left[\frac{\mu g}{L d} \right] = \mu_{max} [d^{-1}] \cdot MIN(f_L, f_N, f_P) \cdot f_T \cdot PhytoC [\mu g/L] \quad (6-2)$$

Light limitation on phytoplankton growth is configured to be subject to photoinhibition, following the P-I curve described by Steele's (1982) equation:

$$f_L = \frac{I}{I_{sat}} \cdot e^{\left(1 - \frac{I}{I_{sat}}\right)} \quad (6-3)$$

where I is the photosynthetically active radiation (PAR) reaching a certain depth, I_{sat} is the PAR saturation value ($\mu E/m^2/s$). To compute PAR, we are using the incoming shortwave radiation values from the hydrodynamic model (SWin) and converted as $PAR = 0.47 \text{ SWin}$

Michaelis-Menten equations are used to model nutrient limitation on the growth (f_N for nitrogen, and f_P for phosphorus).

$$f_N = \frac{[NO_3 + NH_4]}{[NO_3 + NH_4] + K_{SN}} \quad (6-4)$$

$$f_P = \frac{[PO_4]}{[PO_4] + K_{SP}} \quad (6-5)$$

where K_{SN} and K_{SP} are a half-saturation constant for N and P

In addition, algal growth dependance on water temperature is determined by the following equations from (Lehman et al.1975).

$$f_T = \exp \left(-2.3 \cdot \left(\frac{T - T_{opt}}{T_{max} - T_{opt}} \right)^2 \right) \text{ for } T < T_{opt} \quad (6-6)$$

$$f_T = \exp \left(-2.3 \cdot \left(\frac{T - T_{opt}}{T_{max} - T_{opt}} \right)^2 \right) \text{ for } T \geq T_{opt} \quad (6-7)$$

where T is water temperature, T_{opt} is the optimal growth temperature for a phytoplankton group, and T_{max} and T_{min} are the maximum and minimum water temperatures for the species. The maximum and minimum temperatures are the point at which growth has been reduced to 10% of the optimal growth rate by temperature alone.

Phytoplankton Mortality: This term is assumed to be proportional to the daily rate of mortality (k_{mort}), and phytoplankton biomass in the previous time step, corrected by the complementary proportion of the temperature function as follows,

$$Mortality \left[\frac{\mu g}{L d} \right] = k_{mort} [d^{-1}] \cdot (1.13 - f_T) \cdot PhytoC [\mu g/L] \quad (6-8)$$

Phytoplankton Settling: This term is assumed to be proportional to the fixed species dependant settling velocity ($v_{settling}$) and phytoplankton biomass in the top of any two layers considered as follows,

Settling of a phytoplankton class

$$PhytoC_{i-1} \left[\frac{\mu g}{L} \right] = PhytoC_{i-1} \left[\frac{\mu g}{L} \right] + PhytoC_i \left[\frac{\mu g}{L} \right] \cdot \frac{v_{Settling-j} \left[\frac{m}{s} \right] \cdot t_{step} [s^{-1}]}{(d_i - d_{i-1}) [m]} \quad (6-9)$$

$$PhytoC_i \left[\frac{\mu g}{L} \right] = PhytoC_i \left[\frac{\mu g}{L} \right] - PhytoC_i \left[\frac{\mu g}{L} \right] \cdot \frac{v_{Settling-j} \left[\frac{m}{s} \right] \cdot t [s^{-1}]}{(d_i - d_{i-1}) [m]} \quad (6-10)$$

where $v_{settling}$ is the settling rate, t_{step} is the timestep of the model, d_i the depth of the current layer in the model, and d_{i-1} is the depth of the layer below the current layer. Finally, $PhytoC_i$ and $PhytoC_{i-1}$ are the concentrations of phytoplankton carbon at the current layer and the layer below it, respectively.

Phytoplankton Grazing by Zooplankton: This term is a function of the zooplankton counts for each group (*Rotifers*, *Copepodits & Nauplii*, *Diaptomus*, *Bosmina*, *Daphnia*, *Epishura*), which are used as inputs to the model, and group-specific grazing rates from the literature. Grazing rates used for the different zooplankton groups are summarized in Table 6-1.

Table 6-1. Grazing rates ($\mu g C \text{ indv}^{-1} \text{ day}^{-1}$) per zooplankton group and phytoplankton class (1 to 4) used in the model. Gray shading indicates that the zooplankton group does not graze on the corresponding phytoplankton class.

Phytoplankton Group (size)	Rotifers	Copepodits and Napulii	Diaptomus	Bosmina	Daphnia	Epischura
1 (0-2 μm)	0.0004	0.185		0.005		
2 (2-6 μm)	0.0004	0.185		0.005		
3 (6-30 μm)	0.0025		0.227	0.005	0.047	0.078
4 (>30 μm)	0.002					

As a result, the phytoplankton grazing term for each algae group was computed as follows:

$$\text{Grazing of a phytoplankton class} \left[\frac{\mu g}{L \cdot d} \right] = \sum_i \left(\frac{k_{graz-i} [d^{-1}]}{f_{pref}} \cdot N_{zoop_i} [\mu g/L] \right) \quad (6-11)$$

where k_{graz-i} is the zooplankton group-specific grazing rate for each phytoplankton class, f_{pref} is the preference factor of a zooplankton group for each phytoplankton class; we assumed equal preference of a zooplankton group for each phytoplankton class (i.e., f_{pref} ranges between 1 and 4).

6.4. Use of the Lake Clarity Model to Develop the Plankton Food web Model

The Lake Clarity Model was utilized to produce a calibrated phytoplankton food web model that can be supplied to Si3D-AEM. Throughout this section the effort to develop a set of parameters that produce phytoplankton abundances matching samples is referred to as calibration.

6.4.1. Calibration Strategy

Uncertainty in the vertical distribution of zooplankton is likely significant. Hence, zooplankton nutrient excretion and respiration were neglected in the current version of the model since the location of zooplankton in the water column would propagate uncertainty in the distribution of nutrients in the water column and bias phytoplankton nutrient uptake.

While the abundance of nutrients and phytoplankton are interlinked, after accounting for the inputs of nutrients from stream inflow and atmospheric deposition the remaining changes in nutrients concentration in the water column are broadly a result of phytoplankton uptake. As a result, phytoplankton dynamics can be roughly calibrated to in-situ sampling independent of nutrient cycling if nutrient concentrations are not excessively depleted. Consideration of whether and when nutrients are

excessively depleted is a qualitative assessment of how low the most limiting nutrients limitation function can be before it is too depleted for reasonable phytoplankton growth to occur. As a result of this strategy, calibration of different characteristics of the phytoplankton model can be calibrated by two parameters per phytoplankton group in any calibration simulation.

The magnitude of seasonal changes in phytoplankton is controlled by the growth rate and mortality rate. Hence, for the model to accurately produce the maximum and minimum phytoplankton abundances these two terms need to be balanced, that is, populations that do not disappear or increase excessively depleting the nutrient pool available. This category is also where the effect of zooplankton grazing on phytoplankton is applied.

The timing of seasonal changes in phytoplankton is controlled by the impact of the temperature limitation functions on growth and mortality. Within the phytoplankton model temperature limitation is controlled by group specific variables for optimal temperature and temperature range. In practical terms these are the optimal temperature for phytoplankton growth and the distance between the optimal temperature and the maximum or minimum temperature after which growth has been reduced to ten percent. Usually, the maximum and minimum temperatures would be set independently, however, to simplify the model, both variables have been replaced with a fixed offset from the temperature where maximum growth occurs and the maximum or minimum temperature where growth has been reduced to 10% by temperature alone. During calibration, the timing of phytoplankton blooms is determined by the optimal growth temperature while the length of the temperature range around it controls the duration of modeled phytoplankton blooms.

The distribution of phytoplankton in the water column is controlled by the light saturation value and settling rate for each phytoplankton group. Light saturation primarily determines the depth of peak phytoplankton growth in the water column. The settling rate influences the vertical distribution of phytoplankton below and is an important for removal for larger phytoplankton.

Once phytoplankton populations are reliably reproduced by simulations, nutrient dynamics can be calibrated. The water column concentration is changed by the phytoplankton model through the nutrient content ratio of carbon to nitrogen and carbon to phosphorus and the half saturation constant for each nutrient and storage in the phytoplankton.

The amount of phosphorus and nitrogen contained within phytoplankton is accounted for in the model through a nutrient to phytoplankton carbon mass ratio. The values supplied to the model for this were held constant for all phytoplankton groups at the values of the Redfield ratio. However, since the Redfield ratio is an atomic ratio whereas the model utilizes mass directly the values were first converted into a mass ratio.

Since water column nutrient changes from phytoplankton in the model primarily occur as nutrients are stored in phytoplankton as they grow, nutrient limitations on growth are another important tool for calibrating nutrient concentrations to in-situ conditions. In practical terms, when a nutrient is limiting, a concentration of the nutrient equal to the half saturation constant will reduce the maximum growth rate in half. Meanwhile, at concentrations below the half saturation constant, the growth rate decreases at an increasing rate as the concentration approaches zero. Inversely, as the concentration increases above the half saturation constant the decrease to the half saturation constant decreases asymptotically as the nutrient concentration increases. As a result, changing these values in oligotrophic lake Tahoe can

significantly align model and in-situ nutrient profiles by changing the timing, group, and depth at which nutrients are consumed by phytoplankton.

6.4.2. Key Calibration Parameters

While the strategy in the previous section describes the approach taken to calibrate the phytoplankton model, in practice most parameter changes during calibration of the model were adjustments to a maximum growth rate, half saturation constant, or maximum mortality rate of a specific phytoplankton group. Change were also made to either an optimal temperature or temperature range to adjust the timing of seasonal phytoplankton blooms.

6.4.3. Limitations of Model Calibration

Several data constraints limit the accuracy of the calibration.

While the simplified plankton food web model was developed to simulate grazing of six zooplankton groups on four phytoplankton groups, picoplankton were excluded from the calibration due to a lack of data. This group can contribute significantly to primary production (Winder et. al., 2009) and would be expected to have an influence on nutrient cycling. The four phytoplankton groups that were included were selected on the basis of size class, and several species belong to each of those classes. We selected a representative species for that size class, with specific biological characteristics. This is a clear oversimplification, but appropriate for this first phase of modeling.

The assumption that the zooplankton abundance, based on counts of a 150-meter vertical net tow, is evenly distributed through the water is likely incorrect.

Two limitations of the phytoplankton counts are that samples are only collected to a depth of 105 meters and are only available from the LTP monitoring site.

6.4.4. Calibration Assessment

The performances of the plankton food web model were measured using four statistical efficiency criteria: Nash-Sutcliffe efficiency (NSE), coefficient of determination (R^2), root mean square error (RMSE), and mean error (ME). R^2 measures the strength and the direction of a linear relationship between observed and predicted values. The NSE is an index used for assessing the predictive accuracy of a predictive model (Legates and McCabe 1999). The RMSE indicates an overall (global) discrepancy between the observed values and predicted values. The ME indicates the average of the total model errors and is used to measure how close model predictions are to observed values. The mathematical expressions for NSE, R^2 , RMSE, and ME are given as:

$$NSE = 1 - \frac{\sum_{i=1}^n (O_i - P_i)^2}{\sum_{i=1}^n (O_i - \bar{O})^2} \quad (6-122)$$

$$R^2 = \left[\frac{\sum_{i=1}^n (O_i - \bar{O})(P_i - \bar{P})}{\sqrt{\sum_{i=1}^n (O_i - \bar{O})^2 \sum_{i=1}^n (P_i - \bar{P})^2}} \right]^2 \quad (6-13)$$

$$RMSE = \sqrt{\frac{1}{n} \sum_{i=1}^n (O_i - P_i)^2} \quad (6-14)$$

$$ME = \frac{1}{n} \sum_{i=1}^n (O_i - P_i) \quad (6-15)$$

Here, O_i and P_i are observed and predicted values at time i , respectively; \bar{O} and \bar{P} are the mean of the observed and predicted values, respectively; and n = total number of observations. All these efficiency terms are unbiased as they use error statistics relative to the observed values. The model predictions are most precise if values NSE, R^2 , ME, and RMSE are close to 1, 1, 0, and 0, respectively while their ranges vary between $-\infty$ to 1, -1 to 1, $-\infty$ to ∞ , and $-\infty$ to ∞ , respectively.

6.4.5. Calibration Parameters

The following tables list the calibrated values and expected ranges of plankton food web model parameters for phytoplankton groups two through four. Phytoplankton group one may have parameter values similar to group two.

Table 6-2. Phytoplankton model parameters used in LCM simulations for phytoplankton group two, with their units, expected range, and calibrated values.

Phytoplankton Group Two			
Parameter	Units	Calibrated Value	Range
Maximum Growth Rate	µg Carbon/Day	0.41	0.2-8.0
Maximum Mortality Rate	µg Carbon/Day	0.014	0.003-0.17
Optimal Temperature	Celsius	7	0-30
Temperature Boundary Distance	Celsius	27	Unbound
Nitrogen Half Saturation Constant	-	1.5	1-400
Phosphorus Half Saturation Constant	-	1.9	1-25
Ammonia Half Saturation Constant	-	25	20-400
Nitrogen to Carbon Mass Ratio	-	0.176	Unbound
Phosphorus to Carbon Mass Ratio	-	0.024	Unbound
Settling Velocity for Phytoplankton	Meters/Day	0.03	0.1-1.0
Light Saturation for Phytoplankton	Watt/Square Meter	12	10-100

Table 6-3. Phytoplankton model parameters used in LCM simulations for phytoplankton group three, with their units, expected range, and calibrated values.

Phytoplankton Group Three			
Parameter	Units	Calibrated Value	Range
Maximum Growth Rate	µg Carbon/Day	0.44	0.2-8.0
Maximum Mortality Rate	µg Carbon/Day	0.038	0.003-0.17
Optimal Temperature	Celsius	8	0-30
Temperature Boundary Distance	Celsius	20	Unbound
Nitrogen Half Saturation Constant	-	1.5	1-400
Phosphorus Half Saturation Constant	-	5.0	1-25
Ammonia Half Saturation Constant	-	25	20-400
Nitrogen to Carbon Mass Ratio	-	0.176	Unbound
Phosphorus to Carbon Mass Ratio	-	0.024	Unbound
Settling Velocity for Phytoplankton	Meters/Day	0.05	0.1-1.0
Light Saturation for Phytoplankton	Watt/Square Meter	10	10-100

Table 6-4. Phytoplankton model parameters used in LCM simulations for phytoplankton group four, with their units, expected range, and calibrated values.

Phytoplankton Group Four			
Parameter	Units	Calibrated Value	Range
Maximum Growth Rate	µg Carbon/Day	0.46	0.2-8.0
Maximum Mortality Rate	µg Carbon/Day	0.136	0.003-0.17
Optimal Temperature	Celsius	8.5	0-30
Temperature Boundary Distance	Celsius	28	Unbound
Nitrogen Half Saturation Constant	-	1.5	1-400
Phosphorus Half Saturation Constant	-	1.2	1-25
Ammonia Half Saturation Constant	-	25	20-400
Nitrogen to Carbon Mass Ratio	-	0.176	Unbound
Phosphorus to Carbon Mass Ratio	-	0.024	Unbound
Settling Velocity for Phytoplankton	Meters/Day	0.1	0.1-1.0
Light Saturation for Phytoplankton	Watt/Square Meter	12	10-100

6.4.6. Calibration Results

Model results were compared with measured phytoplankton carbon (C) concentrations using two different approaches: time series at selected depths (Fig. 6-1) and vertical profiles on specific dates (Fig. 6-2). Modeled phytoplankton C near the surface for all groups yield a larger summer bloom than observed, with an RMSE that ranged between 6 and 15 µg/L. However, modeled phytoplankton C close to the deep chlorophyll maximum (~60 m) were closer to the measurements but still overestimating them, particularly in late summer and fall. Some of these discrepancies may be due to our selected values of calibration parameters, such as growth and grazing rates. These values have been found in the literature and may not be the most appropriate values although our current understanding of the phytoplankton dynamics in Lake Tahoe does not allow us to improve them. An extended set of plots with data at more depths and dates are provided in Appendix B (Section 11).

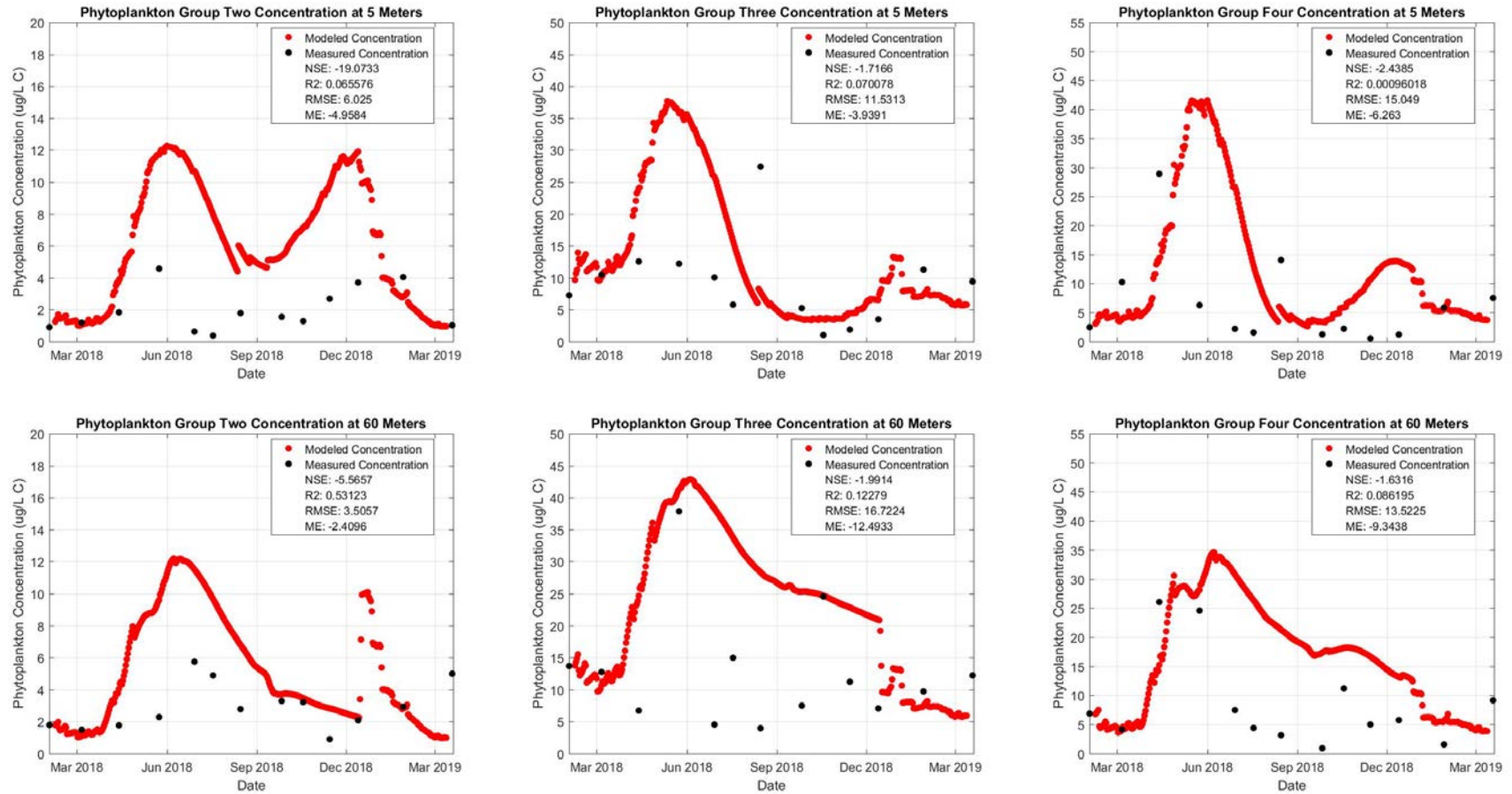


Figure 6-1. Comparison of measured and model simulated phytoplankton concentration for phytoplankton group two (left), group three (middle) and group four (right) at two constant depths from the surface of Lake Tahoe: 5 m (top) and 60 m (bottom). See Appendix B for more information.

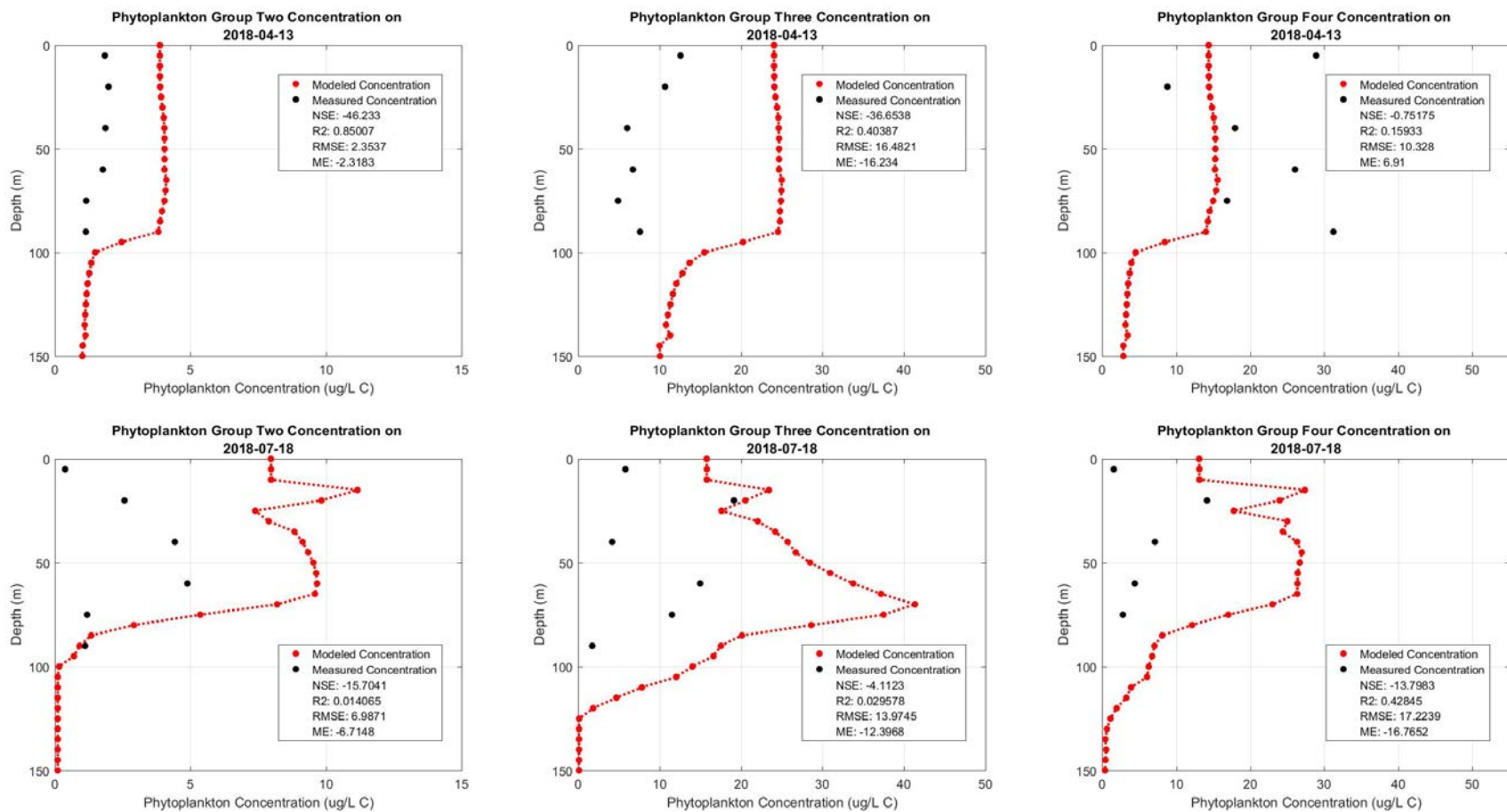


Figure 6-2. Vertical profiles of measured and modeled phytoplankton concentration for phytoplankton group two (left), group three (middle), and group four (right) in spring (top) and summer (bottom) 2019. See Appendix B for more information.

6.4.7. Sensitivity Analysis of LCM with calibrated plankton food web model

A quantitative sensitivity analysis was performed with seventy-three model runs in which we changed one at the time 12 variables for each of the phytoplankton groups two, three, and four. We compared the modeled phytoplankton concentration of the group in which variables were tested to modeled values without any changes in the variables (i.e., calibrated values). The change in each value was qualified as a depth-averaged mean of the median ratio between the changed and calibrated values for a parameter at a given depth (Table 6-5). Overall the relative change in phytoplankton concentration in our sensitivity analysis was larger in phytoplankton group two. This may be partially because relative changes for small concentration values may be large. It would be interesting to evaluate changes in cell numbers and not carbon concentration. For the three phytoplankton groups, we found that the most sensitive variables are optimal temperature, zooplankton grazing rate, phytoplankton maximum growth rate, phytoplankton maximum mortality rate, light saturation, and P and N half-saturation constants. Note that this uncertainty analysis exercise has been done using literature values based on our poor understanding of the different rates affecting the phytoplankton dynamics. An extended set of tables are provided in Appendix B (Section 11).

Table 6-5. List of phytoplankton model variables whose sensitivity was assessed, with their magnitude of change applied and resulting change in modeled phytoplankton concentration for the phytoplankton group which variable was modified. Gray areas indicate less than 10% of the change in the modeled phytoplankton concentration due to the change in the corresponding variable.

Variable Changed	Magnitude of Change	Change in Plankton Group Two	Change in Plankton Group Three	Change in Plankton Group Four
Optimal Temperature	-1 Degree			
	+1 Degree	-11%		
Temperature Boundary Distance	-1 Degree			
	+1 Degree			
Zooplankton Grazing	-10%	-75%		
	+10%	-75%		
Maximum Growth Rate	-10%	-64%	-17%	-31%
	+10%	40%	15%	41%
Maximum Mortality Rate	-10%		13%	53%
	+10%		-11%	-35%
Light Saturation	-10%	-11%		
	+10%			
Phosphorus to Carbon Mass Ratio	-10%			
	+10%			
Nitrogen to Carbon Mass Ratio	-10%			
	+10%			
Settling Velocity for Phytoplankton	-10%			
	+10%			
Nitrogen Half Saturation Constant	-10%	11%		14%
	+10%	-12%		-11%
Phosphorus Half Saturation Constant	-10%	14%		
	+10%	-16%		
Ammonia Half Saturation Constant	-10%			
	+10%			

6.5. Transitioning to 3D implementation

6.5.1. Atmospheric Nutrients and Groundwater Nutrients

The 1D model used the same atmospheric nutrient deposition and groundwater nutrient input rates as LCM. These values were included as the base case for nutrient inputs to Lake Tahoe. However, as described in section 9.2 these have not been implemented into Si3D-AED and should be updated before they are implemented.

6.5.2. Stream Inflows and Nutrient Concentrations

Stream inputs and nutrient data were developed and supplied to LCM to better represent seasonal phytoplankton changes. Stream discharges from the monitored streams listed in Section 3.1 were expressed as daily averages and interpolated to fill data gaps. These values with nutrient and suspended particle data available for these streams, were then processed with a weighted regression on discharge and season (WRTDS; Hirsch et. al, 2010) to produce estimates of daily average concentration for ammonium, nitrate plus nitrite, soluble reactive phosphorus, and total phosphorus for each stream from 2010 to 2020. These values were then expanded to the other fifty-six modeled streams in the Tahoe Basin by taking the nearest monitored stream and rescaling the load by the ratio of the watershed area for each stream.

6.5.3. Optical-Model and Lake Clarity

Due to the time constraints, the optical model of the lake clarity model was disabled and not updated. LCM runs for calibrating the plankton model have used the observed Secchi depths. However, as of the end of phase one of Si3D-AED development all datasets required to run the optical model have been generated. Once suspended particle simulations for LCM are validated it will be possible to recalibrate the model using the phytoplankton groups developed in phase one. A useful characteristic of the optical model is that it can be calibrated outside of the model in which it is used.

7. Three-Dimensional Model

7.1. Hydrodynamic Model

7.1.1. Overview of the Numerical Model

PSi3D is the parallelized version of the semi-implicit, 3D, free-surface hydrodynamic numerical model (Si3D) originally developed to address estuarine circulation (Smith, 2006) and extended to analyze lake hydrodynamics by Rueda (2001). The hydrodynamic model solves the continuity equation for incompressible fluids, the hydrostatic Reynolds-averaged form of the Navier-Stokes equations (the weight of the fluid balances the pressure) and assumes negligible density fluctuations except for the buoyancy term (i.e., the Boussinesq approximation). The numerical model also includes a transport equation for temperature, and an equation of state relating temperature, salinity, and pressure to fluid density (Rueda and Schladow 2003).

PSi3D solves the layer-averaged form of the above equations for stratified flows using a semi-implicit leapfrog-trapezoidal finite difference numerical scheme formulated on a staggered cartesian grid. Temperature is modeled with the advection-diffusion equation following a flux-limiter numerical scheme. Turbulence in the vertical direction is parameterized using the turbulence closure model Mellor-Yamada 2.5, to calculate the vertical turbulent kinetic energy (*TKE*) and a turbulent macroscale (*l*). In the horizontal plane, the turbulence is described following the eddy-viscosity method by either specifying constant values or by parameterizing the horizontal eddy coefficients following Blumberg (1986).

Due to the hydrostatic and Boussinesq approximations implemented on PSi3D-L, it is not able to predict nonlinear internal wave motions and high-frequency internal waves. Despite these model limitations, other 3D lake models with similar formulations have successfully described lake hydrodynamics with reasonable results (e.g., POM: Blumberg and Mellor 1987; MITgcm: Dorostkar et al. 2017; ELCOM or AEM3D: Hodges et al. 2000). Furthermore, lake systems often satisfy the requirement of the shallow water equations, $L \gg H$ (e.g., Lake Tahoe has $L = 35 \text{ km}$ and $H = 502 \text{ m}$). Finally, computational requirements of non-hydrostatic 3D numerical models and common simulations periods considered in 3D lake models (often on the order of weeks or months) are extremely high, and likely unfeasible in a timely manner considering today's technology. For instance, a recent non-hydrostatic 3D numerical model of Lake Cayuga undertaken by Dorostkar et al. (2017) required 7 months of wall-clock runtime for a 4-day period. Therefore, lake systems continue to be modeled by using hydrostatic numerical models. In particular, PSi3D has been used in Lake Tahoe and other lakes with reasonable results (e.g., Hoyer et al. 2015; Rueda and MacIntyre 2009; Rueda et al. 2005; Valbuena. et al. 2021).

Numerical simulations PSi3D require an initial temperature profile that describes the conditions of the lake at the beginning of the study period and a time series of meteorological conditions that include: the wind speed, wind direction, atmospheric pressure, air temperature, shortwave net radiation, incoming longwave radiation, relative humidity, and light attenuation. The initial condition of the velocity field of the numerical model is characterized as a stagnant fluid (i.e., $U = 0$) thus requiring a spin-up time of 3-4 days at the beginning of each simulation.

7.1.2. Model Simulation Periods

We performed the hydrodynamic calibration and validation by evaluating the numerical model performance during 2011 and 2018. While 2011 was a year of high inflows, cool surface temperatures,

and full water column mixing, the year 2018 had low inflows, partial mixing, and warm surface temperatures. The contrast observed between the two years allows evaluation of the performance of the numerical model. In addition, 2018 had a large number of instruments installed in the lake, providing a strong calibration and validation data set for the hydrodynamics.

To address the water clarity seasonality in Lake Tahoe, we divided the numerical simulations into the spring, summer, and fall seasons. The three seasons allowed examination of hydrodynamics during winter lake mixing, spring/summer onset of stratification, and fall thermocline deepening and sharpening. In addition, between May and June of 2018, three large upwelling events were observed. Upwelling of hypolimnetic waters is a potential source of nutrients to the photic zone increasing the pelagic productivity (Corman et al., 2010), and thus the ability of the model to represent these aperiodic events is of relevance for qualitative validation of the numerical model.

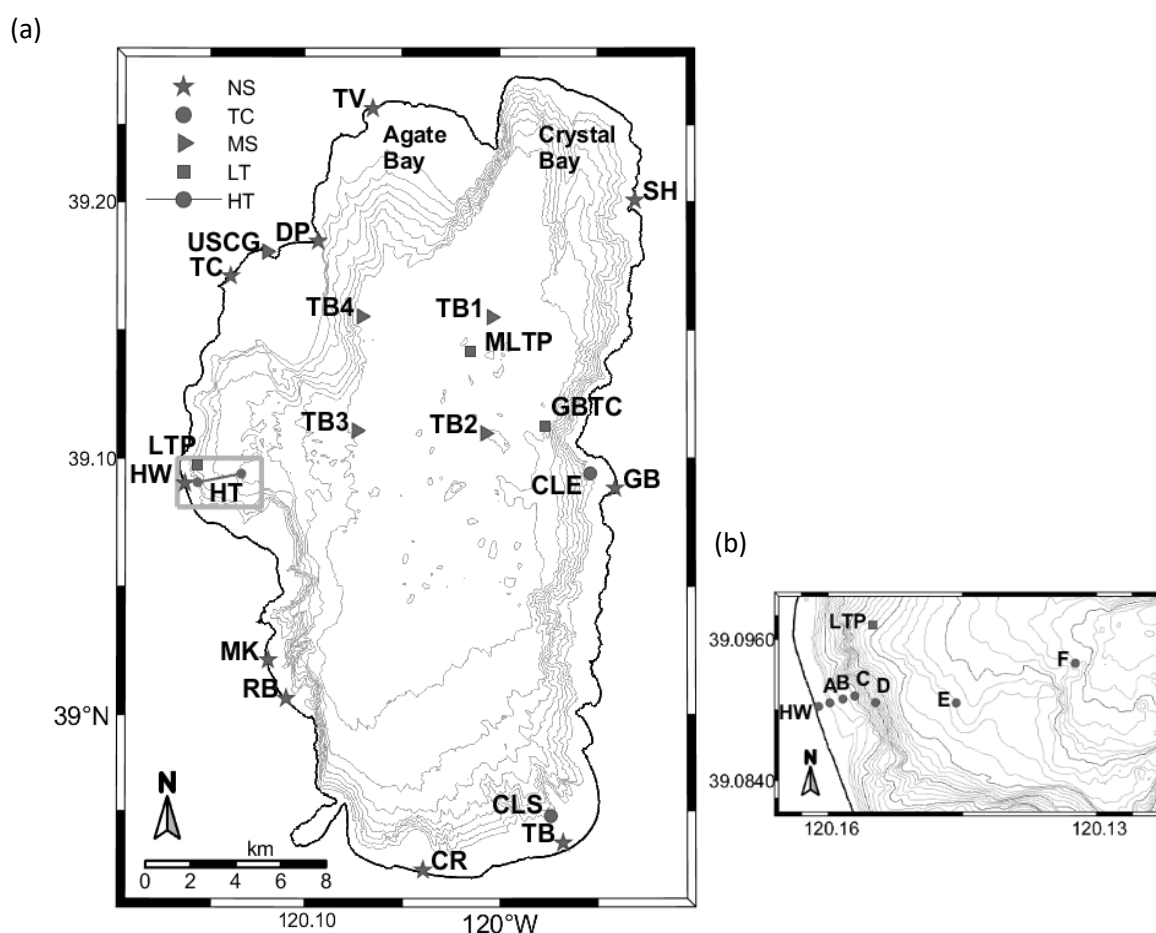


Figure 7-1. Map and an insert at Lake Tahoe with Nearshore Stations (NS), Thermistor Chains (TC), Meteorological Stations (MS), and Homewood Transect (HT). (a) Location of sub-map (HT; gray box) and long-term data available for numerical forcing and validation on a bathymetric map of Lake Tahoe with 50 m isobaths. (b) Zoomed view of the gray box on (a) showing location of moorings with thermistor chain and ADCP deployment during Spring of 2018 and described in Table 7-1.

7.1.3. Field Observations for Model Calibration and Validation

Data available for model calibration and validation are a combination of the long-term data collection network (LT sites in Figure 7-1 - a) and a field deployment between April 14 and June 14, 2018, called

“Upwelling 2018”. The long-term data consists of continuous nearshore measurements at 2 meters of depth at multiple sites around Lake Tahoe (NS sites in Figure 7-1-a), continuous collection on the east shore with multiple sensors (GBTC), and CTD profiles measured at LTP and MLTP. The Upwelling 2018 field experiment included thermistor chains on the west (A-F in Figure 7-1-b), south (CLS), and east shores (CLE) along with ADCP velocity profiles on the west side of the lake (A-E in Figure 7-1-b). A summary of the data available for the model calibration and validation is presented in Table 7-1, and a full description of the Upwelling 2018 project is provided by Roberts et al., (2021).

Table 7-1. Summary of long-term data collection framework and 2018 field deployment in Lake Tahoe available for the numerical model validation and validation

<i>Long-term Sites</i>	<i>Data Type</i>	<i>Instruments/Measurements</i>	<i>Data Range</i>	<i>Date</i>	
<i>NS</i>	Water Quality	Temperature, Conductivity, Pressure, Turbidity, Chl-a, CDOM	2014 – Present		
<i>USCG</i>	Meteorological	Air Temp, Wind Speed/Direction, Relative Humidity, Air Pressure, Shortwave, and Longwave radiation (incoming and outgoing)	1980 – Present		
<i>LTP</i>	CTD	Conductivity, Temperature, and Density	1980 – Present		
<i>MLTP</i>	CTD	Conductivity, Temperature, and Density	1980 – Present		
<i>TB1 – TB4</i>	Meteorological	Air Temp, Wind Speed/Direction, Relative Humidity, Air Pressure, and water temperature at 0.5 m, 1 m, 1.5 m, 2 m, 4 m, 5 m, 5.5 m	1980 – Present		
<i>Project Sites</i>	<i>Depth [m]</i>	<i>Temperature sensor distance from bottom [m]</i>	<i>Instruments/Measurements</i>	<i>Data Range</i>	<i>Date</i>
<i>A</i>	11.3	0, 4, 8	Thermistor Chain and velocity profile from ADCP	Spring 2018	
<i>B</i>	31.0	0, 5, 10, 15, 20, 24, 28	Thermistor Chain and velocity profile from ADCP	Spring 2018	
<i>C</i>	41.5	0, 5, 10, 15, 20, 25, 30, 34, 38	Thermistor Chain and velocity profile from ADCP	Spring 2018	
<i>D</i>	106.6	0, 25, 50, 60, 65, 70, 75, 80, 85, 90, 94, 98	Thermistor Chain and velocity profile from ADCP	Spring 2018	
<i>E</i>	225.4	0, 30, 60, 90, 120, 145, 170, 185, 190, 195, 200, 205, 210, 214, 218	Thermistor Chain and velocity profile from ADCP	Spring 2018	
<i>F</i>	277.4	0, 50, 80, 110, 141, 171, 197, 222, 237, 242, 247	Thermistor Chain	Spring 2018	
<i>CLE</i>	64.7	0, 25, 30, 35, 40, 45, 50, 58	Thermistor Chain	Spring 2018	
<i>CLS</i>	62.5	0, 25, 30, 35, 40, 45, 50, 58	Thermistor Chain	Spring 2018	

7.1.4. Surface Boundary Condition, Initial Conditions, and Grid Size of the Numerical Model

The initial condition for the temperature field is specified as uniform in the horizontal plane and variable in the vertical direction using CTD profiles measured at LTP or MLTP at the start date. Lake morphometry was determined from existing bathymetry data with 10 m × 10 m resolution (Gardner et al., 2000). We

adopted 200 *m* as the horizontal grid resolution for the hydrodynamic model and variable vertical resolution, and we oriented the mesh in the W-E, S-N, and h directions for *x*, *y*, and *z*, respectively. Following the mesh orientation, the velocity components *u*, *v*, and *w* are positive when flowing towards east, north, and up, respectively.

The horizontal grid size was chosen following computational requirements and mesh-independence test results done by Valbuena. et al. (2021), where the velocity field results for spring 2018 were compared among diverse mesh sizes. The grid size chosen also followed consideration of 20% of the internal Rossby radius of deformation as the minimum grid size to properly represent rotational lake hydrodynamics. The Coriolis force is dependent on the latitude of the lake. In particular, for Lake Tahoe, the Coriolis frequency is $f = 9.197e^{-5} s^{-1}$, and has a strong influence on the lake hydrodynamics. For instance, Rueda et al. (2003) identified Kelvin and Poincaré waves (i.e., rotational internal waves), and Valbuena. et al. (2021) described strong rotational effects on the water motions during upwelling and post-upwellings. The strong rotational influence in the lake dynamics supports the application of a 3D numerical lake model over a 1D or 2D model.

Following the Courant–Friedrichs–Lewy condition ($C = u\Delta t/\Delta x$), the time step of the simulations was defined as $\Delta t = 10 \text{ sec}$ to guarantee convergence on the numerical solution to the governing equations. The vertical resolution has a total of 172 layers with variable thicknesses, where 0.5 *m* thick layers are at the surface and increase with depth until reaching a maximum thickness of 5 *m* at 165 *m* of depth. Layer thickness for depths greater than 165 *m* was held constant at 5 *m*. The vertical distribution of the layer thicknesses follows the purpose of having a better representation of the dynamics in the top third of the lake, where heat exchange, biological processes, and fluid motions dominate.

Meteorological parameters from the USCG and the NASA buoys (TBx in Figure 7-1 – a) were used in all the model calibration and validation runs to generate a continuous time series as input for PSi3D. We defined spatially uniform surface boundary conditions across the lake with air temperature, atmospheric pressure, wind speed, and wind direction time series extracted from the four buoys. Specifically, continuous time series were generated using data from TB3, and gaps were filled using data from TB4, TB2, and TB1. Relative humidity, and solar shortwave and longwave radiation records were obtained from the USCG meteorological station. Gaps on the relative humidity time series were filled in sequence using data from TB3 and TB4, and solar irradiance missing records were completed using the statistical forward-moving hourly average. The data collection methods were applied to all seasons considered in this report, except for spring 2011 due to a lack of measurements at USCG (see Section 7.1.7). In addition, weekly measurements using the Secchi disk were used to estimate a time variable light attenuation coefficient following Martin and McCutcheon (1999) (equation (7-1)).

$$eta = \frac{C}{Secchi^{0.73}}, \quad (7-1)$$

where *eta* is the light attenuation coefficient, $C = 1.1$ is an empirical constant value and calibration parameter of this lake model. *Secchi* is the Secchi depth measurement in *m*.

7.1.5. Statistical Metrics of Model Performance

Along with the qualitative comparison of the numerical model and the field observations to corroborate the numerical results at Lake Tahoe, the lake model was statistically validated by computing common

model-performance metrics. We verified the agreement between measured and simulated velocity components by estimating the Root Mean Square Error (RMSE), and the water temperatures by estimating the Model Skill Score (SS) (Murphy and Epstein 1989), error norms I_1 and I_2 , and the RMSE according to the following definitions:

$$SS = 1 - \frac{\sum_{j=1}^N (x_{obsj} - x_{simj})^2}{\sum_{j=1}^N (x_{obsj} - \bar{x}_{obsj})^2}, \quad (7-2)$$

$$I_1 = \frac{\sum_{j=1}^N |x_{simj} - x_{obsj}|}{\sum_{j=1}^N |x_{obsj}|}, \quad (7-3)$$

$$I_2 = \frac{\left[\sum_{j=1}^N (x_{simj} - x_{obsj})^2 \right]^{\frac{1}{2}}}{\left[\sum_{j=1}^N (x_{obsj})^2 \right]^{\frac{1}{2}}}, \quad (7-4)$$

$$RMSE = \sqrt{\frac{\sum_{j=1}^N (x_{simj} - x_{obsj})^2}{N}}, \quad (7-5)$$

where x_{obs} are the field observations, \bar{x}_{obs} is the mean value of all field data points, x_{sim} are the simulated results, and N is the number of data records.

7.1.6. Calibration and Validation of the Model (Spring 2018)

The model was initially applied to simulate the temperature and velocity fields for April 14 to June 14, 2018 (61 days). This initial period was used to define constant parameters such as the bottom drag coefficient, wind drag coefficients, and C from equation (7-1). It was also used to examine the effects of model configurations and numerical schemes on the model results. The spring of 2018 was chosen due to the robust dataset available for the calibration of PSi3D-L. Besides existing long-term data (NS, and LT in Figure 7-1a), data from thermistor chains on the west, east, and south shores, and ADCP measurements on the west shore were available (A, B, C, D, E, F, CLS, CLE in Figure 7-1).

Calibration of the hydrodynamic model was undertaken by modifying the constant parameters, input parameters, and turbulent related configurations. A bottom drag coefficient of $C_{db} = 4.0e^{-3}$ and wind drag coefficient equivalent to $C_{dw} = 1.1e^{-3}$ provided the best prediction of flow and temperature fields in the overall comparison at all sites considered. While the value C_{db} falls on the upper limit of fairly typical values for the bottom drag coefficient (Smith 2006), the C_{dw} is the mean drag coefficient obtained by Amorocho and DeVries (1980) for wind speeds between 0 m s^{-1} and 15 m s^{-1} , the common wind speed range recorded at Lake Tahoe. In addition, the model results indicate a site specific light attenuation coefficient $C = 1.22$ for Lake Tahoe instead of the 1.1 constant suggested in Martin and McCutcheon (1999).

Horizontal diffusion was modeled following Blumberg (1986) where the eddy coefficients are related to the size of the largest eddies resolved by the model, a method proposed by Smagorinsky et al. (1965). This closure scheme provided better results than considering constant horizontal eddy diffusion and viscosity coefficients. We used the centered numerical scheme for the solution of the governing equations and the temperature transport equation.

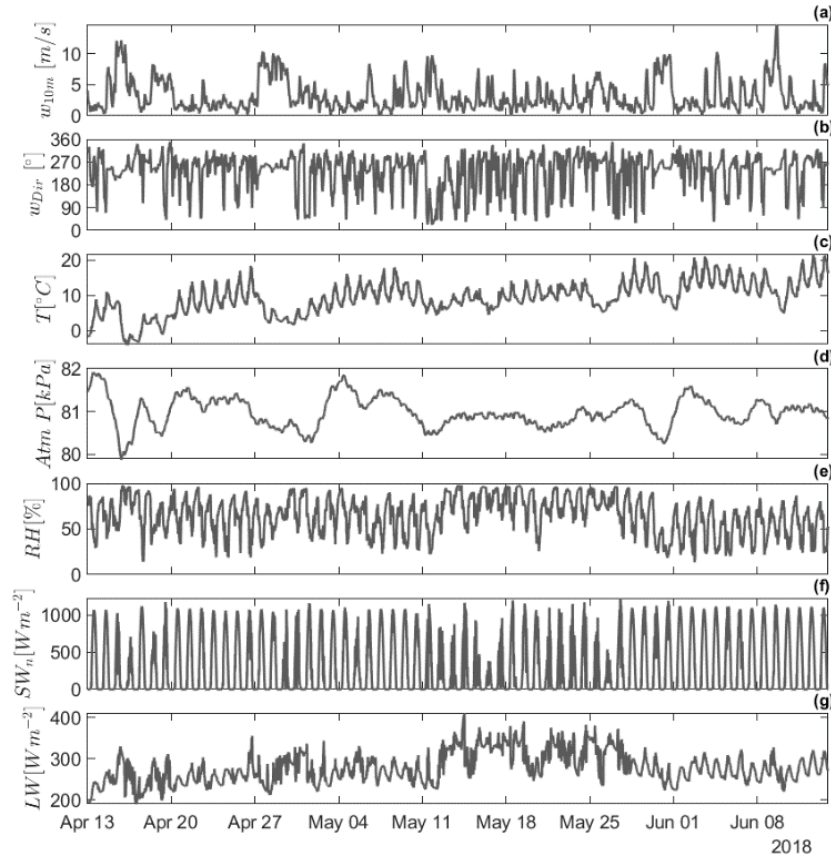


Figure 7-2. Numerical model surface boundary condition parameters from observed meteorological conditions for spring 2018. 0.9 and 1.1 factors applied to wind speed (a) and incoming shortwave, respectively. Time series plot of (a) wind speed, (b) wind direction, (c) air temperature, (d) atmospheric pressure, (e) relative humidity, (f) net shortwave radiation, and (g) incoming longwave.

After a sensitivity analysis and specifically for spring 2018 season, we observed that forcing parameters such as wind speed, and incoming shortwave provided a more accurate prediction of the temperature and flow structures when multiplied by factors of 0.9 and 1.1, respectively. Such adjustments are not unusual and reflect the inherent spatial variability across large lakes.

The applied surface boundary conditions of the numerical model for spring 2018 are shown in Figure 7-2. Comparison between the field measurements and numerical results using the previous configurations are shown in Figure 7-3 to Figure 7-7, where good agreement of the temperature and velocity fields can be observed.

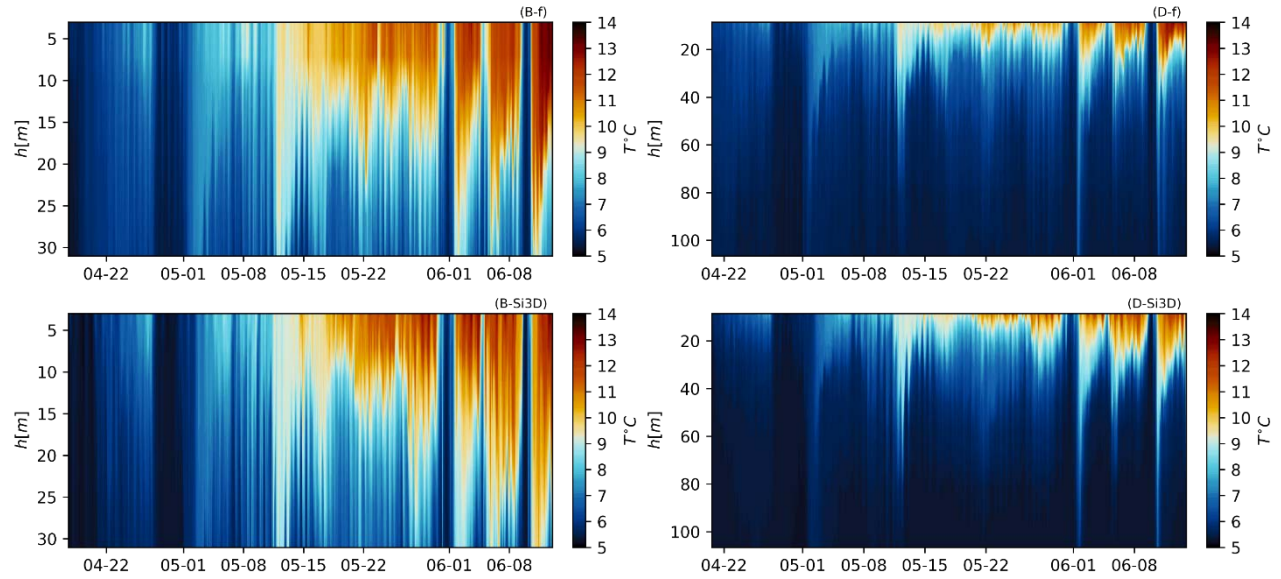


Figure 7-3. Calibration and validation of the numerical results regarding temperature; tile names indicate the site location from Figure 7-1. Time series color plot are named by site followed by -f and -Si3D for field and PSI3D results, respectively. The surface color plot shows the evolution of the temperature structure in time and depth.

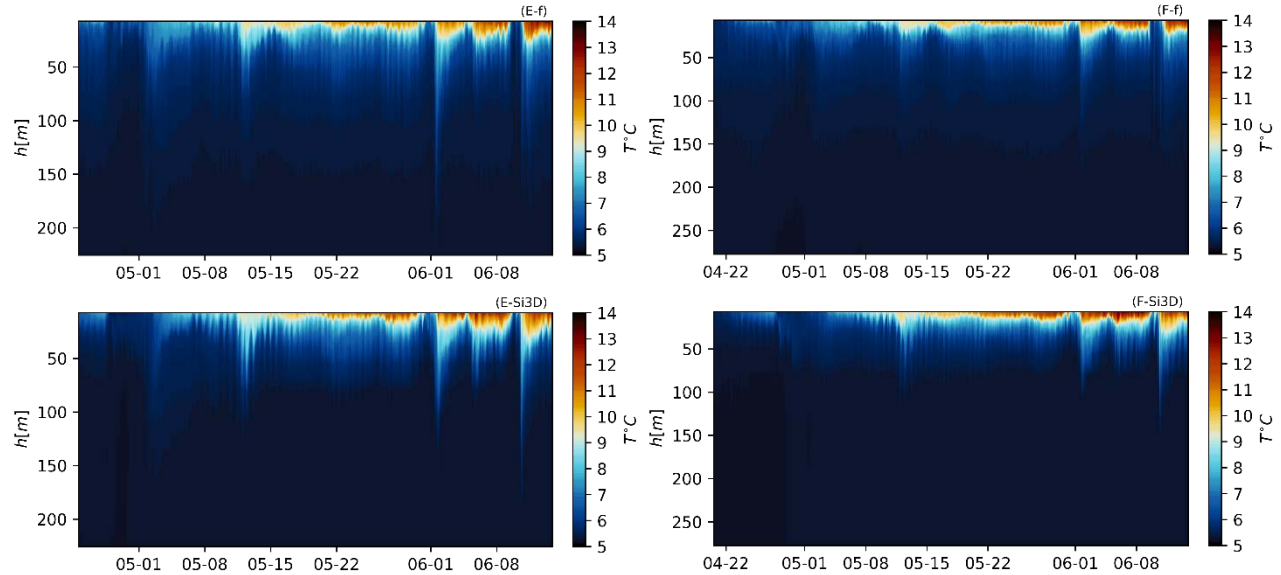


Figure 7-4. Calibration and validation of the numerical results regarding temperature; tile names indicate the site location from Figure 7-1. Time series color plots are named by site followed by -f and -Si3D for field and PSI3D results, respectively. The surface color plot shows the evolution of the temperature structure in time and depth.

During spring of 2018, we focused on the capacity of PSI3D to properly represent the onset of stratification and the annual partial/full lake mixing. The comparison done in Figure 7-3 and Figure 7-4 show that the lake model correctly represents in time and space (depth) and at multiple locations the partial lake mixing recorded on April 22, 2018, with a mixing depth of 285 m. The good agreement of the time and depth of the annual mixing is relevant to the ecology of the lake as this mixing enables upward fluxes of nutrients and downward flows of oxygen-rich surface waters. In addition, PSI3D correctly represents the surface

warming and the vertical temperature profile (Figure 7-3 and Figure 7-4) and the good agreement for individual profiles of the vertical temperature structure (Figure 7-5).

In Figure 7-6 we present the validation of multiple nearshore sites with lake surface records (NS in Figure 7-1-a). The numerical model results show daily temperature fluctuations at the lake surface, overall warming from 5 °C up to 14-16 °C, and rapid temperature decreases corresponding to upwelling events observed at the end of the simulation period. Therefore, overall, PSi3D adequately predicted the nearshore lake surface temperature dynamics. However, daily fluctuations from the numerical results are smoothed in comparison to the field observations. The underestimated temperature oscillations are likely a consequence of the combination of vertical resolution of the layer thicknesses at the surface of the model domain and the relatively coarse horizontal model resolution when applied at the boundaries. Using a nested grid approach in the boundary regions in the future would greatly improve model results in the littoral zone. Nonetheless, the overall warming of the epilimnion, the main driver of the ecology of the lake, is properly represented by this version of the numerical model.

At the end of May and the beginning of June, the lake experienced three upwelling events due to the combination of weak stratification and strong southwestern winds (upwelling on the western and southern shores). Upwelling of deep waters is a source of nutrients to the photic zone, increasing pelagic productivity (Corman et al. 2010). PSi3D results reproduce the timing of the upward movement of cold water and depict the depth of origin of deep waters (May 29 to June 11 in Figure 7-3, Figure 7-4, and Figure 7-6).

The performance metrics for temperature structure are generally good and comparable to results available in the literature (

Table 7-2). Following Scheu et al. (2018), the SS metric results at all sites are within the excellent category (i.e., $S > 0.65$). The norms I_1 and I_2 were on average 0.057 and 0.076 for the whole lake and are similar to values available in the literature, where $I_1 \leq 0.13$ and $I_2 \leq 0.16$ were obtained by Hodges et al. (2000) and Rueda et al. (2003). RMSE values show that differences are greater at the shallowest sites (CR, RB, TV) and the maximum error was 1.39°C , a value that is on the same order of magnitude as the recent 3D hydrodynamic model results in Lake Erie, where RMSE of up to 1.5°C was obtained (Valipour et al. 2019). As noted previously, the primary focus of this project was on the pelagic region of Lake Tahoe, and other methods can be used to improved the littoral zone prediction in the future.

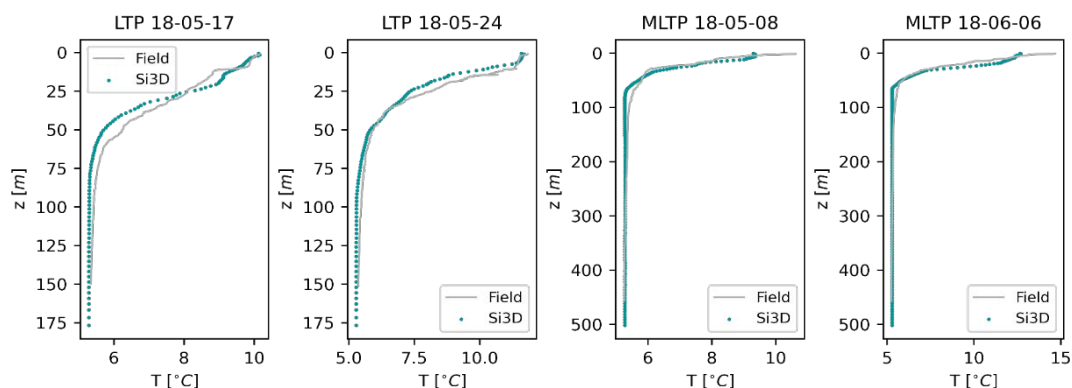


Figure 7-5. Calibration and validation of CTD profiles collected at LTP and MLTP. The title of individual plots indicates the site and date of the temperature profile. PSi3D results (green dots) and the data (gray line).

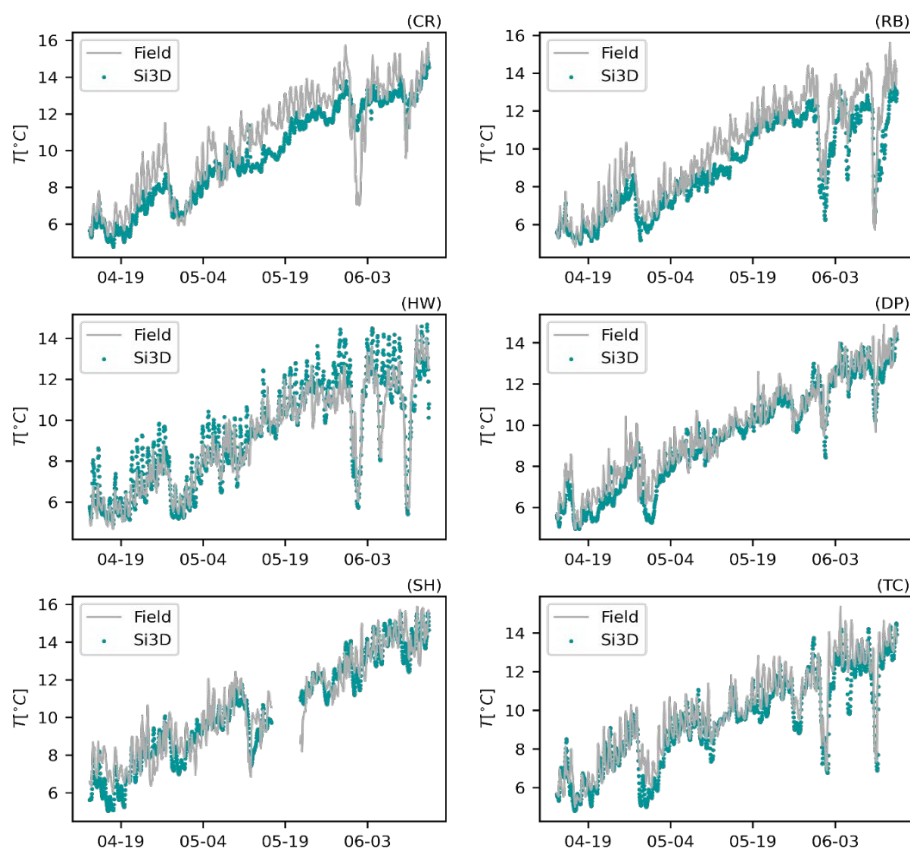


Figure 7-6. Temperature calibration and validation of the numerical results (green dots) and field records (gray line). Tile names indicate the site location from Figure 7-1 of the Nearshore Network (NS). Measurements of temperature at Nearshore sites at ≈ 2 m of depth.

Temperature field observations across the lake (Figure 7-3 to Figure 7-6) show the complexity of the temperature structure in the horizontal and the vertical domains, and their evolution over time. The accuracy of the numerical model to predict the heterogeneity of the temperature field in the 3D domain and the variation through time, support the application of P*Si*3D to represent the lake hydrodynamics at Lake Tahoe. Validation of the numerical model at other locations is shown in Appendix C (Section 11).

Predicted velocities are accurate in both magnitude and direction. In Figure 7-7, we show the comparison of the field observations and numerical results as the velocity evolution in time and depth colored by the velocity magnitude of the horizontal velocity components (u, v). Field observations recorded peak velocities exceeding 0.25 m s^{-1} in the u (positive towards east) and v (positive towards north) directions and are properly predicted by the numerical model. RMSE estimations are less than 10% of the velocity scales observed (

Table 7-2), where horizontal scales are in the order of 25 cm s^{-1} and vertical velocity scale is about 1 cm s^{-1} . Similar level of agreement has been found in previous 3D modeling studies. For instance, Scheu et al. (2018) reported errors from 5 cm s^{-1} up to 18 cm s^{-1} for peak velocities around 30 cm s^{-1} , and Valipour et al. (2019b) reported RMSE of 7.6 cm s^{-1} and 7.2 cm s^{-1} for the u and v components from a 3D hydrodynamic model applied in Lake Geneva. The peak currents were observed at depth during the upwelling and after the relaxation of strong winds. Fast offshore currents during the upwelling and strong counterclockwise alongshore currents after the wind weakens were observed. The coastal jet that could transport particulates, algae, and nutrients along shore and influence near-shore water quality (Rao and Schwab 2007; Valbuena. et al. 2021). PSi3D Validation of the numerical model at other locations is in Appendix C (Section 11).

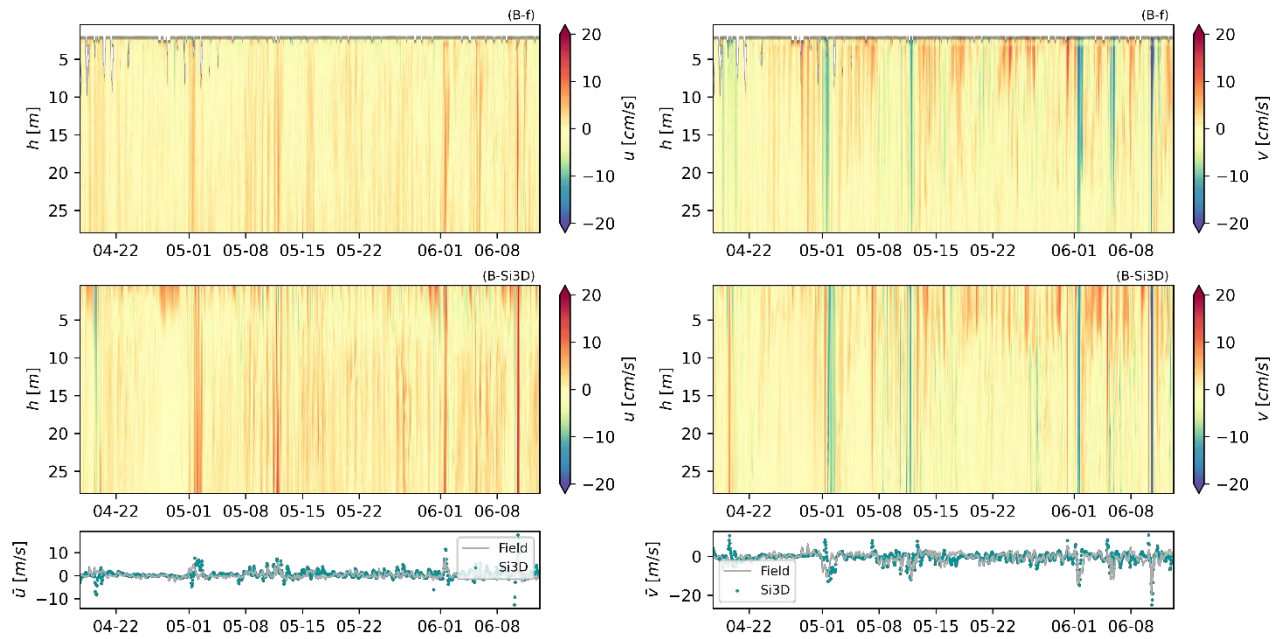


Figure 7-7. Calibration and validation of numerical results of horizontal velocity components u (left plots) and v (right plots). Time series color plot are named by site and followed by -f (field) and -Si3D (PSi3D-L). Bottom time series shows the comparison of the field data (gray line) and numerical results (green dots) for the depth average of \bar{u} (left) and \bar{v} (right).

Table 7-2. Statistical metrics for model performance validation. RSME for the velocity magnitude and error per velocity component. Components u , v , w are for the WE, SN, vertical velocities, respectively.

site	SS	I_1	I_2	RMSE ($^{\circ}\text{C}$)	RMSE u	RMSE v	RMSE w
	Temperature				Velocity (m/s)		
LTP	0.82	0.03	0.04	0.23	-		
MLTP	0.94	0.02	0.04	0.25	-		
TB1	0.86	0.06	0.09	0.88	-		
TB2	0.92	0.05	0.07	0.68	-		
TB3	0.90	0.06	0.08	0.77	-		
TB4	0.87	0.06	0.09	0.86	-		
CR	0.78	0.10	0.12	1.29	-		
DP	0.90	0.06	0.07	0.75	-		
HW	0.87	0.07	0.09	0.87	-		
RB	0.79	0.10	0.12	1.21	-		
SH	0.88	0.07	0.08	0.85	-		
TC	0.86	0.07	0.09	0.89	-		
TV	0.66	0.11	0.13	1.39	-		
LTP	0.82	0.03	0.04	0.23	-		
MLTP	0.94	0.02	0.04	0.25	-		
TB1	0.86	0.06	0.09	0.88	-		
TB2	0.92	0.05	0.07	0.68	-		
TB3	0.90	0.06	0.08	0.77	-		
TB4	0.87	0.06	0.09	0.86	-		
GBTC	0.92	0.04	0.07	0.43	-		
F	0.89	0.05	0.08	0.47	-		
CLE	0.74	0.10	0.13	0.86	-		
CLS	0.81	0.08	0.11	0.78	-		
B	0.87	0.07	0.09	0.67	0.025	0.035	0.002
D	0.88	0.05	0.07	0.47	0.025	0.029	0.006
E	0.92	0.04	0.06	0.39	0.036	0.038	0.015

7.2. Biogeochemical and Ecological Model: PSi3D-AEM

7.2.1. Overview of PSi3D-AEM

We have implemented a coupled Aquatic Ecological Model (AEM) to the parallelized hydrodynamic PSi3D numerical model described in section 7.1. For this project, we will refer to the newly developed coupled 3-D parallelized hydrodynamic Aquatic Ecological Model as PSi3D-AEM. Such an approach was used in the original Lake Clarity Model (Losada 2001; Swift et al. 2006) that was part of the TMDL development. That effort utilized a one-dimensional hydrodynamic model, as that was the only feasible approach at that time. The approach has been applied previously using both a one-dimension framework such as MINLAKE (Riley and Stefan 1988) and DYRESM-WQ (Hamilton and Schladow 1997; Schladow and Hamilton 1997), and a three-dimension framework such as ELCOM-CAEDYM (Hodges et al. 2000; Mooji et al. 2010; Hipsey et al. 2019). Coupled hydrodynamic-ecological models are used as a management tool in a variety of lakes such as Lake Erie (Boegman et al. 2008, Leon et al. 2011, Wang and Boegman 2021), Lake Kinneret, (Bruce et al. 2006), Lake Michigan (Chen et al. 2002), and Lake Champlain (Marti et al. 2019), among others (Bruce et al. 2018). In all these coupled models, ecological processes are updated after each hydrodynamic model time step. In PSi3D-AEM the aquatic ecological model uses the temperature and velocity solved in the hydrodynamic module to simulate the advective and diffusive transport of active scalars or state variables. Active scalars will change due to transport in each time step and due to chemical and biological processes quantified using source-sink equations. This source-sink equations follow the parameterizations described in Hipsey et al. (2019).

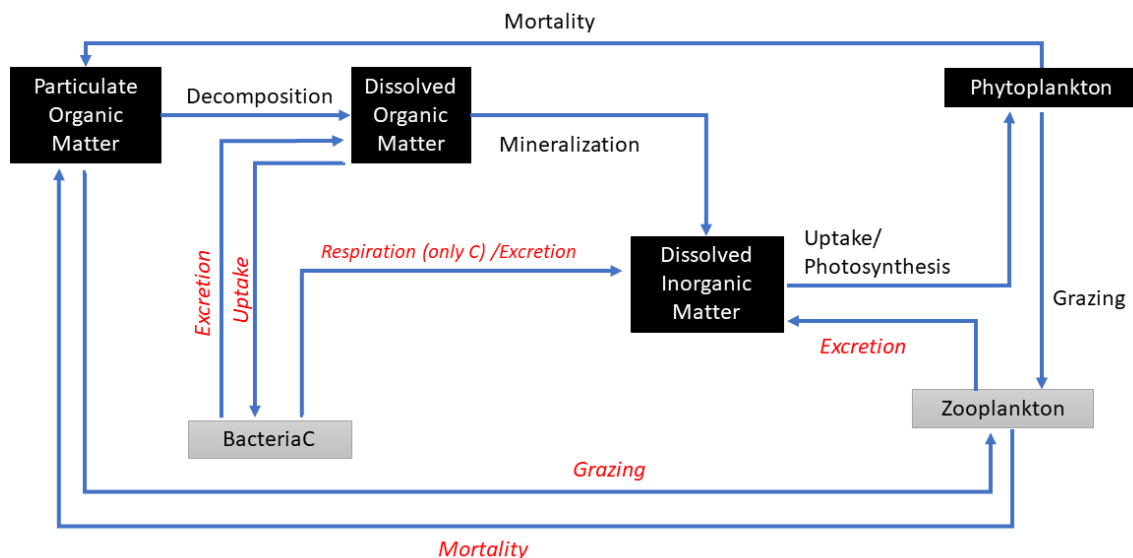


Figure 7-8. Generic diagram of the main state variables and processes modeled in PSi3D-AEM. State variables in black are explicitly modeled (particulate organic matter, dissolved organic matter, dissolved inorganic matter, and phytoplankton), while state variables in gray are not modeled (zooplankton and bacteria). Processes in red have not been parameterized but are included in this figure for completeness.

For this project, the AEM includes cycling of carbon (C), nitrogen (N), and phosphorus (P), along with phytoplankton dynamics including growth, respiration and grazing by zooplankton. Figure 7-8 is a generic diagram of the main state variables and processes modeled in PSi3D-AEM. Each state variable or active scalar has a source-sink equation associated to quantify its rate of change in each time step. State variables

in black are explicitly modeled (particulate organic matter, dissolved organic matter, dissolved inorganic matter, and phytoplankton as four individual functional groups), while state variables in gray are not explicitly modeled (zooplankton and bacteria) but their impact on the other state variable is accounted for. Zooplankton are treated as input data. Processes, shown in red, have not been parameterized but are included in this figure for completeness.

The model accounts for the source and sink terms of each state variable:

- Nitrogen forms: particulate organic nitrogen (PON), dissolved organic nitrogen (DON), ammonium (NH_4), and nitrate plus nitrite (NO_3)
- Phosphorus forms: particulate organic phosphorus (POP), dissolved organic phosphorus (DOP), and soluble reactive phosphorus (SRP)
- Four phytoplankton groups (ALG1, ALG2, ALG3, ALG4), as carbon units. We model particulate organic carbon (POC) and dissolved organic carbon (DOC).

Main features of PSi3D-AEM include:

- Phytoplankton represented as particulate carbon
- Four phytoplankton functional groups arranged by cell size, with particular attention to *Cyclotella* spp.:
 - o Group 1: Size < 2 μm (picoplankton)
 - o Group 2: Size 2-6 μm (e.g., *Cyclotella*)
 - o Group 3: Size 6-30 μm (e.g., *Cryptomonas*)
 - o Group 4: Size > 30 μm (e.g., *Synedra*)
- Nutrient regeneration (C, N, P).
- A Tahoe-specific grazing model driven by the zooplankton counts measured in the lake and literature-based grazing rates for Lake Tahoe and similar aquatic ecosystems.
- The coupled model operates on any sub-daily time step to resolve algal processes. Due to the large computational resources (time and space) required to save 3D outputs, we produced model results every 4 hours.

As described in the hydrodynamic model section, our goal was to run PSi3D-AEM for the three seasons (spring, summer, and fall) in two different years (2011 and 2018). Due to the large computational requirements of our 3D simulations, we were able to complete the calibration of the model using data from spring 2018. In the next sections we will present the following:

- Overview of the phytoplankton and nutrient dynamics, including conceptual models, equations, and model parameters/constants.
- Available data for initial conditions and calibration in spring 2018.
- Modeled phytoplankton and nutrient results in spring 2018.

7.2.2. Phytoplankton and Nutrient Dynamics: Conceptual Models, Equations & Parameters

The equations and parameters described below are adapted from the following sources: Hamilton and Schladow (1997); Losada (2001); Swift et al. (2006); Trommer et al (2019), and Hipsey et al. (2019).

7.2.2.1. Phytoplankton

Phytoplankton biomass is represented as particulate carbon (PhytoC, $\mu\text{g/L}$) and we currently model four phytoplankton functional groups arranged by cell size: (1) size $< 2 \mu\text{m}$ (picoplankton); (2) size $2-6 \mu\text{m}$; (3) size $6-30 \mu\text{m}$; (4) size $> 30 \mu\text{m}$. For each phytoplankton group, the source-sink equation that models the rate of change of phytoplankton carbon concentration ($d[\text{PhytoC}]/dt$) includes three processes: growth (source), mortality, and grazing (sinks).

$$\frac{d[\text{PhytoC}]}{dt} = \text{Growth} - \text{Mortality} - \text{Grazing} \quad (7-6)$$

Phytoplankton Growth: The rate of change of phytoplankton biomass (*Growth*) is proportional to the phytoplankton biomass in the previous time step (*PhytoC*) and the product of a series of constants. The daily maximum potential growth (μ_{max}) rate is multiplied by a temperature function (f_T) and the minimum value of expressions for limitation by light (f_L), nitrogen (f_N), and phosphorus (f_P), as follows,

$$\text{Growth} \left[\frac{\mu\text{g}}{\text{L d}} \right] = \mu_{max} [d^{-1}] \cdot \text{MIN}(f_L, f_N, f_P) \cdot f_T \cdot \text{PhytoC} [\mu\text{g/L}] \quad (7-7)$$

Light limitation on phytoplankton growth is configured to be subject to photoinhibition, following the P-I curve described by Steele's (1982) equation:

$$f_L = \frac{I}{I_{sat}} \cdot e^{\left(1 - \frac{I}{I_{sat}}\right)} \quad (7-8)$$

where I is the photosynthetically active radiation (PAR) reaching a certain depth, I_{sat} is the PAR saturation value ($\mu\text{E/m}^2/\text{s}$). To compute PAR, we are using the incoming shortwave radiation values from the hydrodynamic model (SWin) and converted as $\text{PAR} = 0.47 \text{ SWin}$

Michaelis-Menten equations are used to model nutrient limitation on the growth (f_N for nitrogen, and f_P for phosphorus). In addition, an Arrhenius equation (f_T) is used to account for temperature correction on the growth rate:

$$f_N = \frac{[NO_3 + NH_4]}{[NO_3 + NH_4] + K_{SN}} \quad (7-9)$$

$$f_P = \frac{[PO_4]}{[PO_4] + K_{SP}} \quad (7-10)$$

$$f_T = \vartheta^{(T-20)} \quad (7-11)$$

where K_{SN} and K_{SP} are a half-saturation constant for N and P, respectively, ϑ is a temperature correction constant and T is water temperature.

Phytoplankton Mortality: This term is assumed to be proportional to the daily rate of mortality (k_{mort}), and phytoplankton biomass in the previous time step, corrected by a temperature as follows,

$$\text{Mortality} \left[\frac{\mu\text{g}}{\text{L d}} \right] = k_{mort} [d^{-1}] \cdot f_T \cdot \text{PhytoC} [\mu\text{g/L}] \quad (7-12)$$

Phytoplankton Grazing by Zooplankton: This term is a function of the zooplankton counts for each group (*Rotifers*, *Codotia*, *Nauplii*, *Diaptomus*, *Bosmina*, *Daphnia*, *Epishura*), which are used as input time series

for the model, and group-specific grazing rates found in the literature. Grazing rates for the different zooplankton groups in Lake Tahoe are summarized in Table 7-3.

Table 7-3. Grazing rates ($\mu\text{g C indv}^{-1} \text{ day}^{-1}$) of the different zooplankton groups in Lake Tahoe according to the phytoplankton size that they graze (0-6 μm ; 6-30 μm ; >30 μm). Literature values show different grazing rates depending on the season (spring, summer and fall). Gray shading indicates that the zooplankton group does not graze on the corresponding phytoplankton class.

Rotifers			
Months/size	0-6 μm	6-30 μm	>30 μm
Spring (Apr-May)	0.00039	0.0020	0.0020
Summer (Jun-Aug)	0.00039	0.0020	0.0020
Fall (Sep-Oct)	0.00039	0.0020	0.0020
Copepodits&Nauplii			
Months/size	0-6 μm	6-30 μm	>30 μm
Spring (Apr-May)	0.08-0.29		
Summer (Jun-Aug)	0.08-0.29		
Fall (Sep-Oct)	0.08-0.29		
Diaptomus			
Months/size	0-6 μm	6-30 μm	>30 μm
Spring (Apr-May)		0.06	
Summer (Jun-Aug)		0.30	
Fall (Sep-Oct)		0.32	
Bosmina			
Months/size	0-6 μm	6-30 μm	>30 μm
Spring (Apr-May)	0.0049	0.0049	
Summer (Jun-Aug)	0.0049	0.0049	
Fall (Sep-Oct)	0.0049	0.0049	
Daphnia			
Months/size	0-6 μm	6-30 μm	>30 μm
Spring (Apr-May)	unknown	0.048	
Summer (Jun-Aug)	unknown	0.046	
Fall (Sep-Oct)	unknown	0.046	
Epischura			
Months/size	0-6 μm	6-30 μm	>30 μm
Spring (Apr-May)		0.049	
Summer (Jun-Aug)		0.051	
Fall (Sep-Oct)		0.12	

Assuming a mean annual value per zooplankton group and phytoplankton class, grazing rates used in the model are summarized in Table 7-4.

Table 7-4. Grazing rates ($\mu\text{g C indv}^{-1} \text{ day}^{-1}$) per zooplankton group and phytoplankton class (1 to 4) used in the model. Gray shading indicates that the zooplankton group does not graze on the corresponding phytoplankton class.

Phytoplankton Group (size)	Rotifers	Copepodits&Napuli	Diatomus	Bosmina	Daphnia	Epischura
1 (0-2 μm)	0.0004	0.185		0.005	unknown	
2 (2-6 μm)	0.0004	0.185		0.005	unknown	
3 (6-30 μm)	0.002		0.227	0.005	0.047	0.078
4 (>30 μm)	0.002					

As a result, the phytoplankton grazing term for each algae group was computed as follows:

$$\text{Grazing of a phytoplankton class } \left[\frac{\mu\text{g}}{\text{L d}} \right] = \sum_i \left(\frac{k_{\text{graz}-i} [\text{d}^{-1}]}{f_{\text{pref}}} \cdot f_T \cdot N_{\text{zoop}i} [\mu\text{g/L}] \right) \quad (7-13)$$

where $k_{\text{graz}-i}$ is the zooplankton group-specific grazing rate for each phytoplankton class, f_{pref} is the preference factor of a zooplankton group for each phytoplankton class; we assumed equal preference of a zooplankton group for each phytoplankton class (i.e., f_{pref} ranges between 1 and 4).

We refer the user to We also included the ranges of values found in the literature for those parameters.

Table 7-5 for a full description of all constants and their values used in the model simulations.

7.2.2.2. *Carbon*

Carbon is considered the “primary currency” within AEM and the carbon cycle forms the backbone upon which the other elemental cycles are based. The carbon state variables of AEM carbon cycling are phytoplankton carbon (PhytoC), particulate organic carbon (POC), dissolved organic carbon (DOC), dissolved inorganic carbon (DIC), zooplankton and bacterial carbon (zooC and bacteriaC). The last three state variables have not been modeled in the current version of AEM due to lack of data, but are included in our conceptual diagram for completeness (Figure 7-9).

The main processes involved in carbon fate in the water column are:

- Biological uptake of DIC by phytoplankton (photosynthesis)
- Mortality of phytoplankton into POC and excretion into DOC (lumped together)
- Decomposition of POC into DOC
- Mineralization of DOC into DIC
- Microbial uptake of DOC
- Settling and resuspension of phytoplankton and POC
- Dissolved sediment flux of DOC
- Respiration of living organisms into DIC
- Grazing of phytoplankton, bacteria, zooplankton, and POC by zooplankton

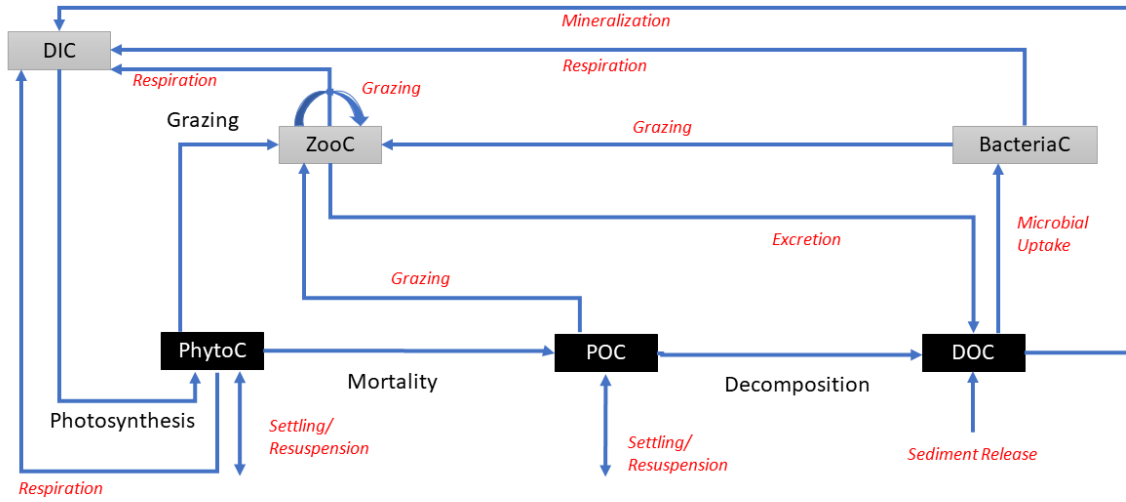


Figure 7-9. Carbon cycling conceptual model, including state variables and processes modeled in PSi3D-AEM. State variables in black are explicitly modeled (particulate organic carbon, dissolved organic carbon, and phytoplankton carbon), while state variables in gray are not modeled (zooplankton, bacteria and dissolved inorganic carbon). Processes in red have not been parameterized but are included in this figure for completeness.

Due to the lack of input data, limited literature values to parameterize some of the above-described ecological processes in Lake Tahoe, or lack of time to refine their implementation, only three carbon state variables have been modeled (PhytoC, POC, DOC), which are marked in black in Figure 7-9. Similarly, processes in red in this figure have not been parameterized. The source-sink equation showing the rate of change PhytoC has been described in detail in the previous section 7.2.2.1. Source-sink equations for POC and DOC are as follows,

$$\frac{d[POC]}{dt} = \underbrace{k_{mort} [d^{-1}] \cdot \vartheta^{(T-20)} \cdot PhytoC [\mu g/L]}_{\text{Phytoplankton Mortality}} - \underbrace{k_{dcc} [d^{-1}] \cdot \vartheta^{(T-20)} \cdot POC \left[\frac{\mu g}{L} \right]}_{\text{Decomposition}} \quad (7-14)$$

$$\frac{d[DOC]}{dt} = \underbrace{k_{dcc} [d^{-1}] \cdot \vartheta^{(T-20)} \cdot POC [\mu g/L]}_{\text{Decomposition}} \quad (7-15)$$

We also included the ranges of values found in the literature for those parameters.

Table 7-5 has a full description of all constants and their values assigned in the model simulations based on calibration. We also included the ranges of values found in the literature for those parameters.

Table 7-5. List of selected parameters used in PSi3D-AEM simulations, with their symbols, units, assigned values based on calibration and values from the literature.

Biological parameter	Symbols	Units	Assigned values	Values from literature
Maximum growth rate of phytoplankton	μ_{max}	d^{-1}	0.4	0.2-4.5 ^{a,b}
PAR saturation value	I_{sat}	$\mu E/m^2/s$	40	40-500 ^{c,d}
half-saturation constant for nitrogen	K_{SN}	$\mu g/L$	30	10-35 ^{e,f}
half-saturation constant for phosphorus	K_{SP}	$\mu g/L$	10	3-11 ^{e,f}
Temperature correction constant	ϑ	-	1.08	1.0- 1.14 ^{a,d}
Ratio of nitrogen to carbon	rnc	-	0.176	16:106 ^l
Ratio of phosphorus to carbon	rpc	-	0.024	1:106 ^l
Algae preference factor for NH ₄	f_{NH_4}	-	0.25	0.2-0.25 ^{f,g}
Mortality rate	kmort	d^{-1}	0.06	0.03-0.2 ^{f,g}
Chemical parameter	Symbols	Units	Assigned values	Values from literature
PON decomposition rate	k_{dcn}	d^{-1}	0.01	0.01-0.03 ^{a,f,h}
DON mineralization rate	k_{mn}	d^{-1}	0.001	0.001-0.005 ^{a,f,i}
Nitrification rate	k_n	d^{-1}	0.01	0.01-0.02 ^{f,d,j}
Denitrification rate	k_{dn}	d^{-1}	0.0	0.05-0.15 ^{f,d,j}
POP decomposition rate	k_{dcp}	d^{-1}	0.01	0.01-0.1 ^{f,k}
DOP mineralization rate	k_{mp}	d^{-1}	0.001	0.001-0.1 ^{f,k}
POC decomposition rate	k_{dcc}	d^{-1}	0.01	0.01-0.2 ^f
Temperature correction constant for decomposition	ϑ	-	1.08	1-1.1 ^{a,i}
Temperature correction constant for mineralization	ϑ	-	1.02	1-1.05 ^{a,i}
Temperature correction constant for nitrification	ϑ	-	1.08	1-1.1 ^{a,d}
Temperature correction constant for denitrification	ϑ	-	1.04	1-1.08 ^{a,d}

^aBowie et al (1985); ^bPollingher and Berman (1982); ^cSchladow & Hamilton (1997); ^dChapra (1997); ^eBruce et al (2006); ^fLosada 2001; ^gChen et al (2002); ^hHipsey et al (2006); ⁱMissaghi and Hondzo (2010); ^jRomero et al (2004); ^kLeon et al (2011); ^lRedfield (1958)

7.2.2.3. Nitrogen

The nitrogen forms modeled in AEM are particulate organic nitrogen (PON), dissolved organic nitrogen (DON), ammonium (NH₄), and nitrate plus nitrite (NO₃+NO₂). The conceptual diagram of the processes is shown in Figure 7-10. The main processes involved in nitrogen fate in the water column are:

- Biological uptake of NO₃ and NH₄ by phytoplankton
- Biological mortality of phytoplankton into PON and DON, respectively
- Biological excretion of NH₄ by zooplankton
- Mineralization of DON to NH₄
- Nitrification of NH₄ to NO₃
- Denitrification of NO₃ to N₂
- Settling and resuspension of PON

- Dissolved sediment flux and groundwater release of NO_3 and NH_4
- Atmospheric deposition of DON and NH_4

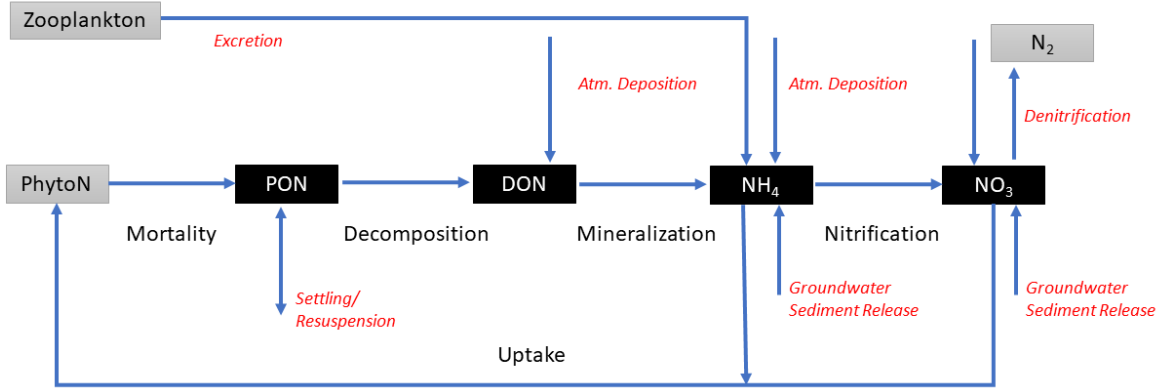


Figure 7-10. Nitrogen cycling conceptual model, including state variables and processes modeled in PSI3D-AEM. State variables in black are explicitly modeled (particulate organic nitrogen, dissolved organic nitrogen, ammonium and nitrate), while state variables in gray are not modeled (phytoplanktonN and N_2). In addition, processes in red have not been parameterized but are included in this figure for completeness.

Due to the lack of input data, limited literature values to parameterized some of the above-described ecological processes in Lake Tahoe, or lack of time to refine their implementation, processes in red in Figure 7-10 have not been parameterized. The source-sink equation equations for PON, DON, NH_4 , and NO_3 are as follows,

$$\frac{d[\text{PON}]}{dt} = \underbrace{rnc \cdot k_{mort} [d^{-1}] \cdot \vartheta^{(T-20)} \cdot \text{PhytoC} [\mu g/L]}_{\text{Phytoplankton Mortality}} - \underbrace{k_{dcn} [d^{-1}] \cdot \vartheta^{(T-20)} \cdot \text{PON} \left[\frac{\mu g}{L} \right]}_{\text{Decomposition}} \quad (7-16)$$

$$\frac{d[\text{DON}]}{dt} = \underbrace{k_{dcn} [d^{-1}] \cdot \vartheta^{(T-20)} \cdot \text{PON} [\mu g/L]}_{\text{Decomposition}} - \underbrace{k_{mn} [d^{-1}] \cdot \vartheta^{(T-20)} \cdot \text{DON} \left[\frac{\mu g}{L} \right]}_{\text{Mineralization}} \quad (7-17)$$

$$\begin{aligned} \frac{d[\text{NH}_4]}{dt} = & \underbrace{k_{mn} [d^{-1}] \cdot \vartheta^{(T-20)} \cdot \text{DON} [\mu g/L]}_{\text{Mineralization}} - \underbrace{k_n [d^{-1}] \cdot \vartheta^{(T-20)} \cdot \text{NH}_4 \left[\frac{\mu g}{L} \right]}_{\text{Nitrification}} - \\ & \underbrace{rnc \cdot f_{\text{NH}_4} \cdot \mu_{max} [d^{-1}] \cdot \text{MIN}(f_L, f_N, f_P) \cdot f_T \cdot \text{PhytoC} [\mu g/L]}_{\text{Phytoplankton Growth}} \end{aligned} \quad (7-18)$$

$$\begin{aligned} \frac{d[\text{NO}_3]}{dt} = & \underbrace{k_n [d^{-1}] \cdot \vartheta^{(T-20)} \cdot \text{NH}_4 \left[\frac{\mu g}{L} \right]}_{\text{Nitrification}} - \underbrace{k_{dn} [d^{-1}] \cdot \vartheta^{(T-20)} \cdot \text{NO}_3 \left[\frac{\mu g}{L} \right]}_{\text{Denitrification}} - \\ & \underbrace{rnc \cdot (1 - f_{\text{NH}_4}) \cdot \mu_{max} [d^{-1}] \cdot \text{MIN}(f_L, f_N, f_P) \cdot f_T \cdot \text{PhytoC} [\mu g/L]}_{\text{Phytoplankton Growth}} \end{aligned} \quad (7-19)$$

We refer the user to We also included the ranges of values found in the literature for those parameters.

Table 7-5 for a full description of all constants and their values used in the model simulations.

7.2.2.4. Phosphorus

The phosphorus forms modeled in AEM are particulate organic phosphorus (POP), dissolved organic phosphorus (DOP), and soluble reactive phosphorus (SRP). The conceptual diagram of the processes is shown in Figure 7-11. The main processes involved in phosphorus fate in the water column are:

- Biological uptake of SRP by phytoplankton
- Biological mortality of phytoplankton into POP and DOP, respectively
- Biological excretion of SRP by zooplankton
- Mineralization of DOP to SRP
- Settling and resuspension of POP
- Dissolved sediment flux and groundwater release of SRP
- Atmospheric deposition of DOP and SRP

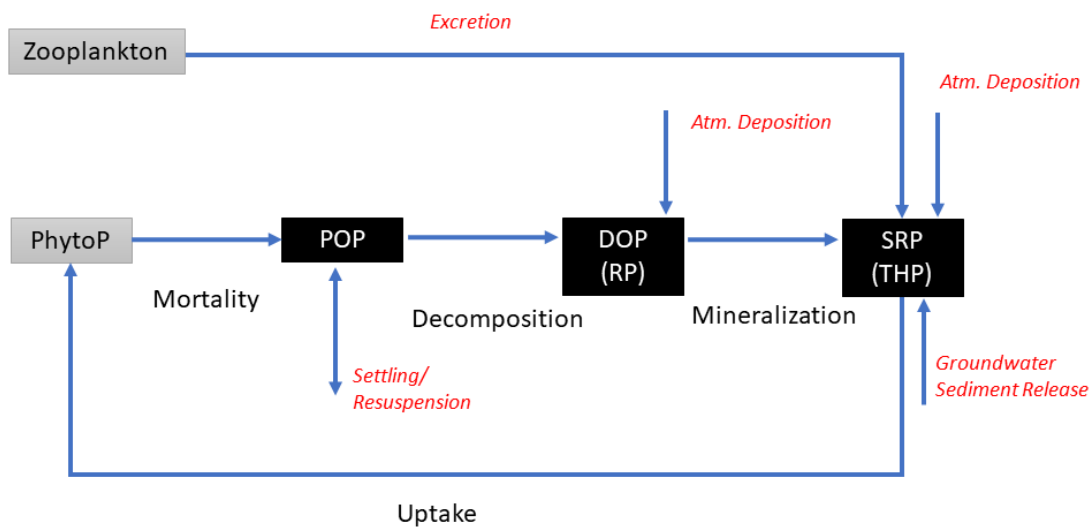


Figure 7-11. Phosphorus cycling conceptual model, including state variables and processes modeled in PSI3D-AEM. State variables in black are explicitly modeled (particulate organic phosphorus, dissolved organic phosphorus, and soluble reactive phosphorus), while state variables in gray are not modeled (phytoplanktonP). In addition, processes in red have not been parameterized but are included in this figure for completeness.

Due to the lack of input data, limited literature values to parameterize some of the above-described ecological processes in Lake Tahoe, or lack of time to refine their implementation, processes in red in Figure 7-11 have not been parameterized. The source-sink equation equations for POP, DOP, and SRP are as follows,

$$\frac{d[POP]}{dt} = \underbrace{rpc \cdot k_{mort} [d^{-1}] \cdot \vartheta^{(T-20)} \cdot PhytoC [\mu g/L]}_{\text{Phytoplankton Mortality}} - \underbrace{k_{dcp} [d^{-1}] \cdot \vartheta^{(T-20)} \cdot POP [\frac{\mu g}{L}]}_{\text{Decomposition}} \quad (7-20)$$

$$\frac{d[DOP]}{dt} = \underbrace{k_{dcp} [d^{-1}] \cdot \vartheta^{(T-20)} \cdot POP [\mu g/L]}_{\text{Decomposition}} - \underbrace{k_{mp} [d^{-1}] \cdot \vartheta^{(T-20)} \cdot DOP [\mu g/L]}_{\text{Mineralization}} \quad (7-21)$$

$$\frac{d[SRP]}{dt} = \underbrace{k_{mp} [d^{-1}] \vartheta^{(T-20)} DOP \left[\frac{\mu g}{L} \right]}_{Mineralization} - \underbrace{rpc \cdot \mu_{max} [d^{-1}] \cdot MIN(f_L, f_N, f_P) \cdot f_T \cdot PhytoC [\mu g/L]}_{Phytoplankton Growth} \quad (7-22)$$

We refer the user to We also included the ranges of values found in the literature for those parameters.

Table 7-5 for a full description of all constants and their values used in the model simulations.

7.2.3. Field measurements: Data for Initial Conditions and Calibration

7.2.3.1. Phytoplankton, Zooplankton and Carbon

The numerical model uses phytoplankton biomass expressed as units of carbon, PhytoC ($\mu\text{g/L}$). The biomass of phytoplankton carbon was determined from recorded abundances (cell counts) of phytoplankton and calculated biovolumes following the approach described in Section 4.3. The monthly total phytoplankton carbon profiles collected at LTP in 2011 and 2018 are shown in Figure 7-12 and Figure 7-13. Phytoplankton carbon values ranged between 5 and 20 $\mu\text{g/L}$ during most of the year, with peak concentrations of $\sim 80 \mu\text{g/L}$ by the end of summer/early fall.

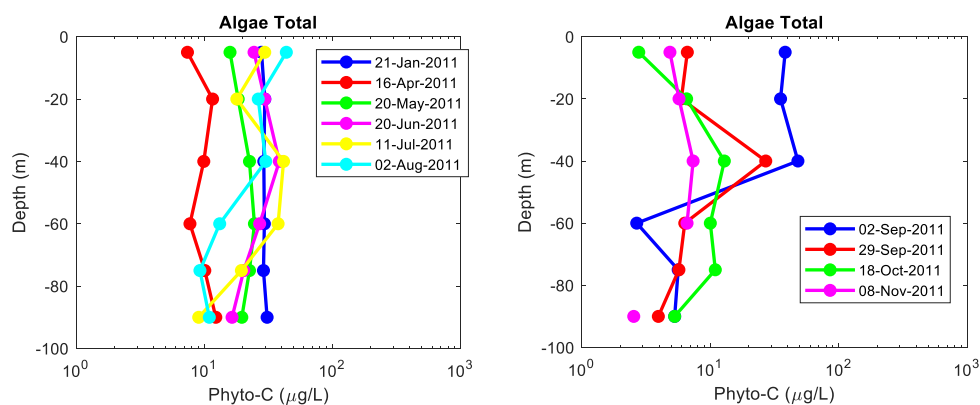


Figure 7-12. Monthly total phytoplankton carbon profiles collected at LTP in 2011

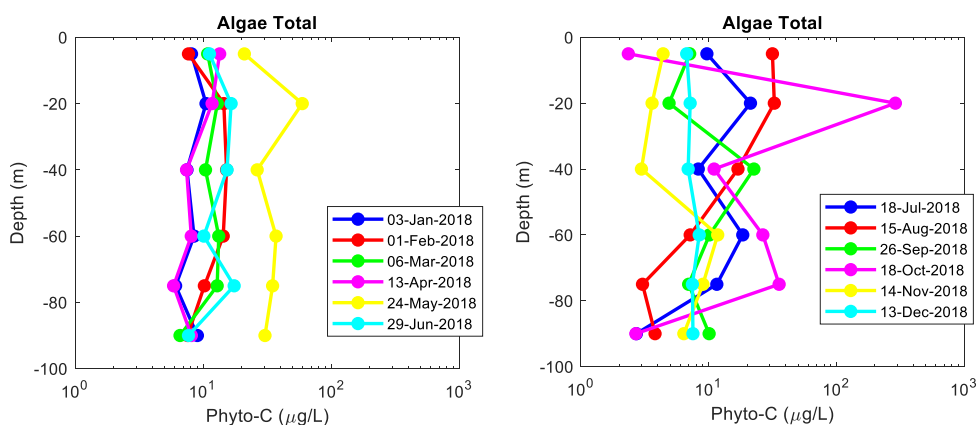


Figure 7-13. Monthly total phytoplankton carbon profiles collected at LTP in 2018

For the *calibration* of the coupled hydrodynamic-ecological PSi3D-AEM model, we used phytoplankton carbon data during spring (April, May, and June) 2018 for the different phytoplankton groups (Figure 7-14). Initial conditions for the ecological model are the blue profiles (April 2018) in Figure 7-14. Only phytoplankton from functional groups 2 and 3 was found during that time of the year. Values of total phytoplankton carbon increased from $\sim 10 \mu\text{g/L}$ to $\sim 20 \mu\text{g/L}$ between April and June 2018. Phytoplankton carbon of Group 2 (2-6 μm) represents only 1% of the total carbon and also doubled during these two months.

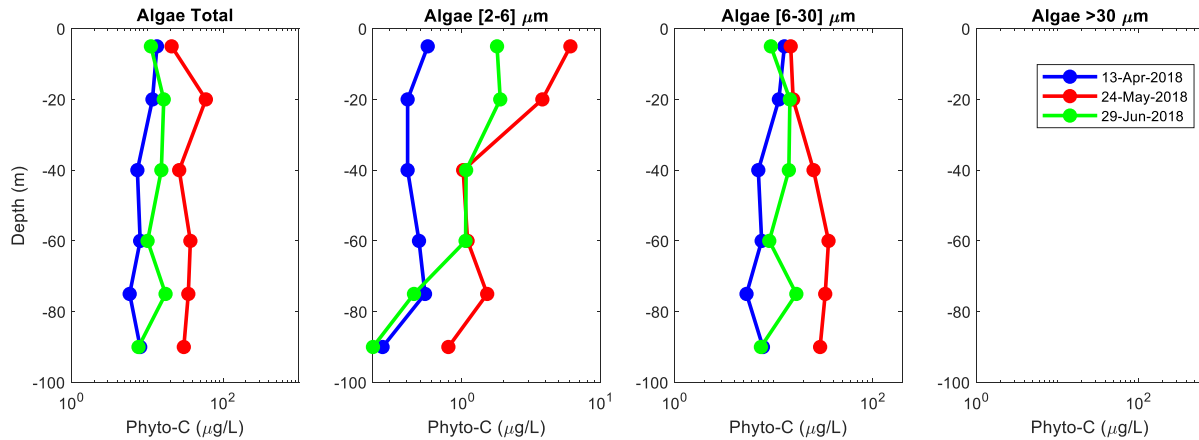


Figure 7-14. Phytoplankton carbon profiles for the different phytoplankton groups collected at LTP in spring 2018. Blue profiles are the initial conditions for the numerical model.

Values of primary production by phytoplankton (PPr) obtained from monthly measurements with 4 hour incubation periods in spring 2018 are presented in Figure 7-15. PPr values were of order $5 \text{ mg/m}^3/4\text{-h}$ and were highest at 20 m in April 2018. Values increased slightly in June 2018 with a peak in PPr at $\sim 50 \text{ m}$. These profiles allow us to calibrate the growth term of the source-sink equation for phytoplankton in our numerical model. All measured values of PPr in 2011 and 2018 are presented in Appendix D (Section 13).

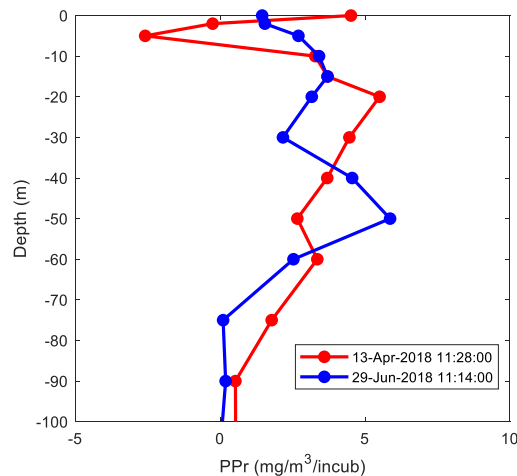


Figure 7-15. Primary production by phytoplankton (PPr) values obtained from incubation experiments at LTP in spring 2018.

Values of zooplankton density obtained from monthly sampling in the top 150 m at LTP in spring 2018 are presented in Figure 7-16. Note that *Daphnia* were not present during the study period. Also, we have assumed that zooplankton is evenly distributed over the top 150 m, though we do not have data to support this assumption. All measured values of zooplankton density in 2011 and 2018 are presented in Appendix D (Section 13).

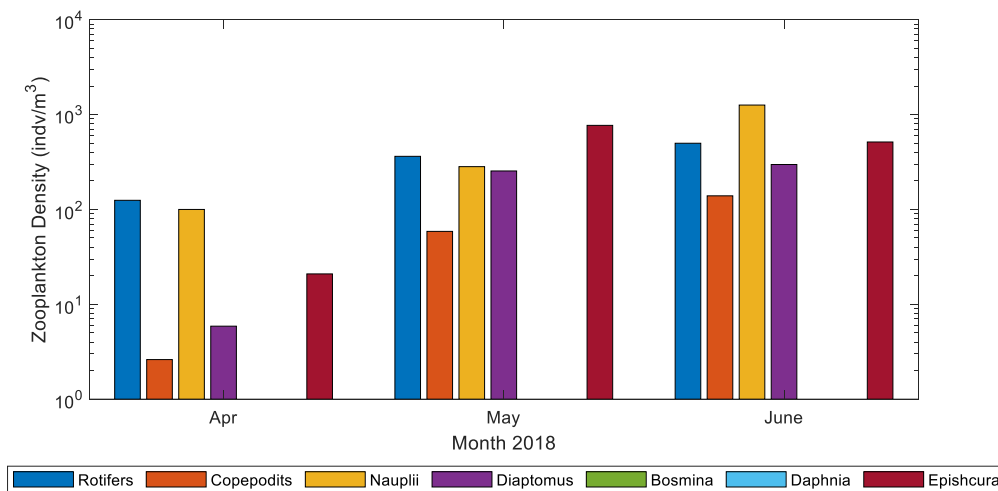


Figure 7-16. Zooplankton density values from monthly sampling at LTP in spring 2018.

In addition to phytoplankton carbon content, primary productivity, and zooplankton densities, the numerical model needs values of dissolved and particulate organic carbon (DOC and POC, respectively) for its initialization. Historical data for these constituents are DOC ~500 µg/L and POC ~100 µg/L. The pool of dissolved inorganic carbon in Lake Tahoe is considered sufficiently large to not be limiting algal growth.

7.2.3.2. Nitrogen

The nitrogen forms modeled in AEM are particulate organic nitrogen (PON), dissolved organic nitrogen (DON), ammonium (NH₄), and nitrate plus nitrite (NO₃). Available measured fractions are Total Kjeldahl nitrogen (TKN = Organic nitrogen + NH₄), ammonium (NH₄), and nitrate plus nitrite (NO₃). Averaged values of these analytes measured in spring 2018 are:

- TKN ~ 42 µg/L
- NH₄ ~ 5 µg/L
- NO₃ ~ 10 µg/L

Thus, the total organic nitrogen can be estimated as, ON = TKN – NH₄ ~ 37 µg/L. We used annually mean averaged fractions to compute the particulate and dissolved organic nitrogen (PON and DON) from the total organic nitrogen (Marjanovic 1989), as PON = 0.166 ON and DON = 0.834 ON. Thus, the initial conditions used for the numerical model in spring 2018 are:

- PON ~ 7 µg/L
- DON ~ 30 µg/L
- NH₄ ~ 5 µg/L
- NO₃ ~ 10 µg/L

All measured values of nitrogen forms in 2018 are presented in Appendix D (Section 13).

7.2.3.3. Phosphorus

The phosphorus forms modeled in AEM are particulate organic phosphorus (POP), dissolved organic phosphorus (DOP), and soluble reactive phosphorus (SRP). Available measured fractions are total

phosphorus (TP), dissolved phosphorus (DP), and total hydrolysable phosphorus (THP). Averaged values of these analytes measured in Spring 2018 are:

- TP ~ 40 µg/L
- DP ~ 30 µg/L
- THP ~ 5 µg/L

Thus, the particulate phosphorus can be estimated as $PP = TP - DP$. We assumed that the particulate inorganic phosphorus pool is very small, thus, $POP \sim PP$. Measured THP is assumed to be representative of the immediately biologically available phosphorus or SRP. Finally, dissolved organic phosphorus is computed as, $DOP = DP - THP$. Thus, the initial conditions used for the numerical model in spring 2018 are:

- POP ~ 10 µg/L
- DOP ~ 25 µg/L
- SRP ~ 5 µg/L

All measured values of *phosphorus* forms in 2018 are presented in Appendix D (Section 13).

7.2.4. Model results: Phytoplankton and Nutrients

Phytoplankton Carbon

Model phytoplankton carbon concentrations in spring 2018 are similar to values measured in the field (Figure 7-14 and Figure 7-17). Phytoplankton carbon concentrations ranged between [0.5-3] µg/L for group 2 (size 2-6 µm) (Figure 7-17a,d) and between [10-80] µg/L for group 3 (size 6-30 µm) (Figure 7-17b,e). Phytoplankton growth was slow during the second half of April when lake temperatures were low and the seasonal stratification was not developed. Phytoplankton carbon concentrations slowly increased during the first half of May. We modeled the highest values between mid-May to mid-June when lake stratification fully developed. The phytoplankton growth progressively increased in the top 20 m at MLTP (Figure 7-17d,e) while upwelling events of cool waters on June 1 and June 9 diluted the phytoplankton population at LTP for a few days before the phytoplankton population increased again (Figure 7-17a,b). We observed a larger growth of both phytoplankton groups after upwelling events at LTP.

Nitrogen and Phosphorus Forms

Model nitrogen values did show the nutrient recycling associated with the phytoplankton dynamics implemented for PSi3D-AEM (Figure 7-18). Biogeochemical processes such as decomposition, mineralization, and nitrification drove the conversion of particulate organic nitrogen (PON) into dissolved organic nitrogen (DON), and then ammonium and nitrate (NH₄ and NO₃). As a result, we observed lower values of PON and DON than NH₄ and NO₃ in deep waters (~100 m). Values of nitrogen in the top 20 m changed as the phytoplankton community evolved. Increased mortality and excretion led to larger values of PON and DON in the top 20 m when the phytoplankton carbon increased in mid-May, while NH₄ and NO₃ decreased near the surface due to the growing demand for nutrients by phytoplankton. These changes occurred continuously at MLTP (Figure 7-18e-h), while the upwelling events occurring in June brought nutrient-rich water to the surface, but low in organic matter (Figure 7-18a-d).

Model phosphorus values had similar trends as nitrogen forms due to food web interactions, but changes were not as large due to the low C:P ratio (Figure 7-19). Decomposition and mineralization drove the

conversion of organic forms into soluble reactive phosphorus which increased at the lake surface. Changes occurred continuously at MLTP (Figure 7-19d-f), while upwelling events in June brought low SRP water to the surface (Figure 7-19a-c).

Phytoplankton Growth Limiting Factors

Model outputs of the phytoplankton growth limiting factors such as light (f_L), nitrogen (f_N), phosphorus (f_P), and temperature (f_T) were explored to better understand phytoplankton dynamics (Figure 7-20, Equations 7-8 to 7-11). Light limited the phytoplankton growth daily between 6:00 AM and 6:00 PM, with maximum growth between 20 and 40 m and inhibited growth in the top 10 m and below 50 m. Model results showed that dissolved inorganic nitrogen limited the phytoplankton growth more ($f_N \sim 0.5$) than dissolved inorganic phosphorus ($f_P \sim 0.7$). Nitrogen limitation was more intense in the top 20 m, where phytoplankton growth was larger ($f_N \sim 0.3$). Upwelling events in June altered limiting nutrient factors: they increased f_N but decreased f_P . Temperature correction factor was always above 0.85, with values closer to one when lake temperature increased close to 12°C.

Spatial Variability of Nutrients and their Effect on Phytoplankton Carbon

We studied the spatial variability of nutrients and their effect on phytoplankton carbon when conditions drove larger horizontal gradients that occurred during the upwelling events in June (Figure 7-21). During late May, phytoplankton carbon concentrations were not above 64 $\mu\text{g/L}$ across the lake, and dissolved inorganic nitrogen and phosphorus were of order $\sim 25 \mu\text{g/L}$ and $\sim 28 \mu\text{g/L}$, respectively. Dissolved inorganic nitrogen forms (NH_4 and NO_3) increased 50% near-surface on the west shore during the upwelling event on June 9, while water with low-SRP concentration at that location and time. In a few hours, water rich in NH_4 and NO_3 at the lake surface on the west shore of the lake were transported counterclockwise due to the coast jet. After 3-4 days after the upwelling event and the coast jet started the transport of nutrients hugging the shoreline, the phytoplankton carbon concentrations in the pelagic zone of the lake increased by $\sim 30\%$ (from 64 to 82 $\mu\text{g/L}$).

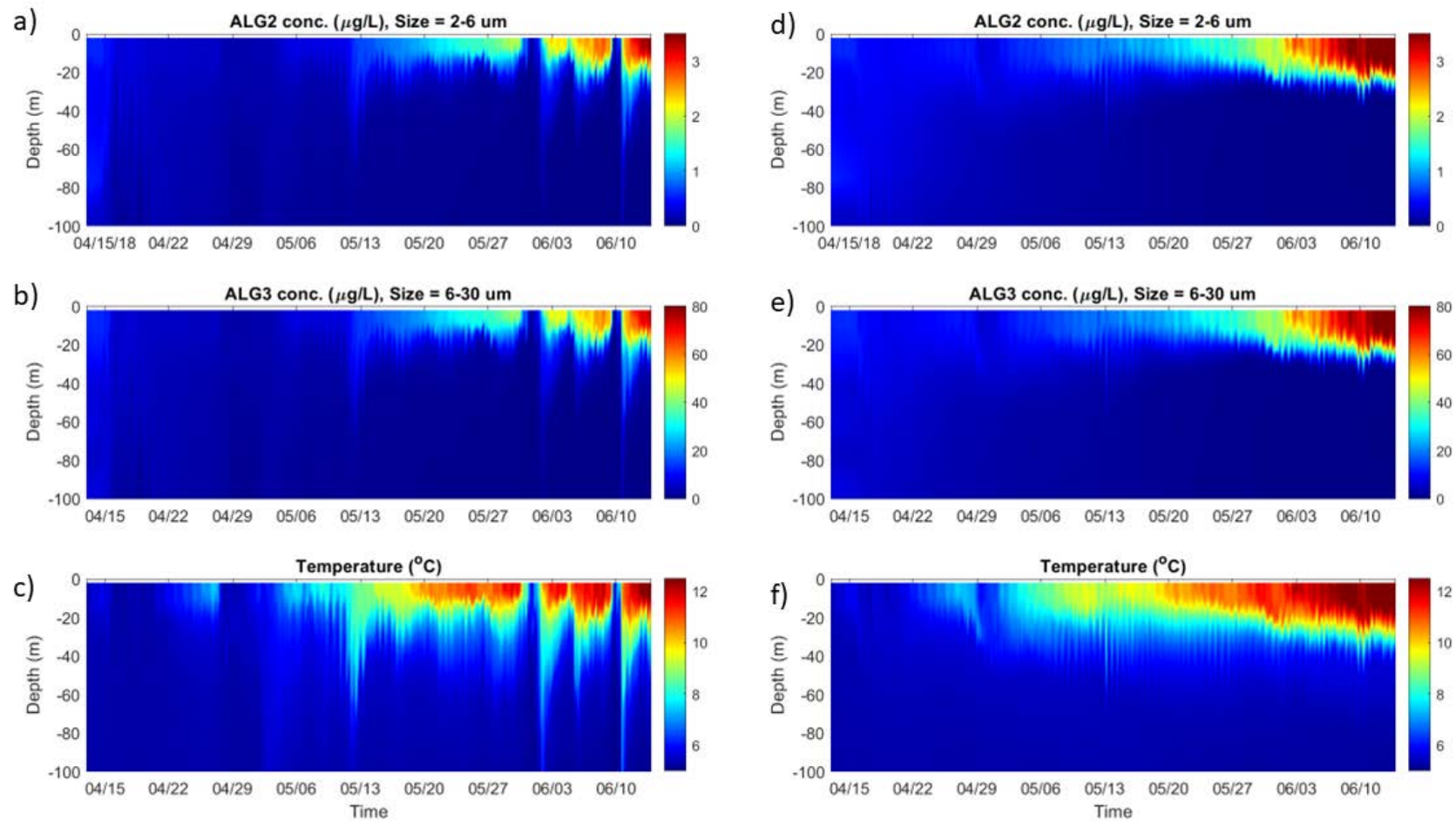


Figure 7-17. Model time series of phytoplankton carbon of group 2 (a,d) and group 3 (b,e) in spring 2018 in the top 100 m at LTP (a-c) and MLTP (d-e) assuming that only growth, mortality, and grazing affect the phytoplankton dynamics. Lake temperatures during the same period at LTP (c) and MLTP (f)

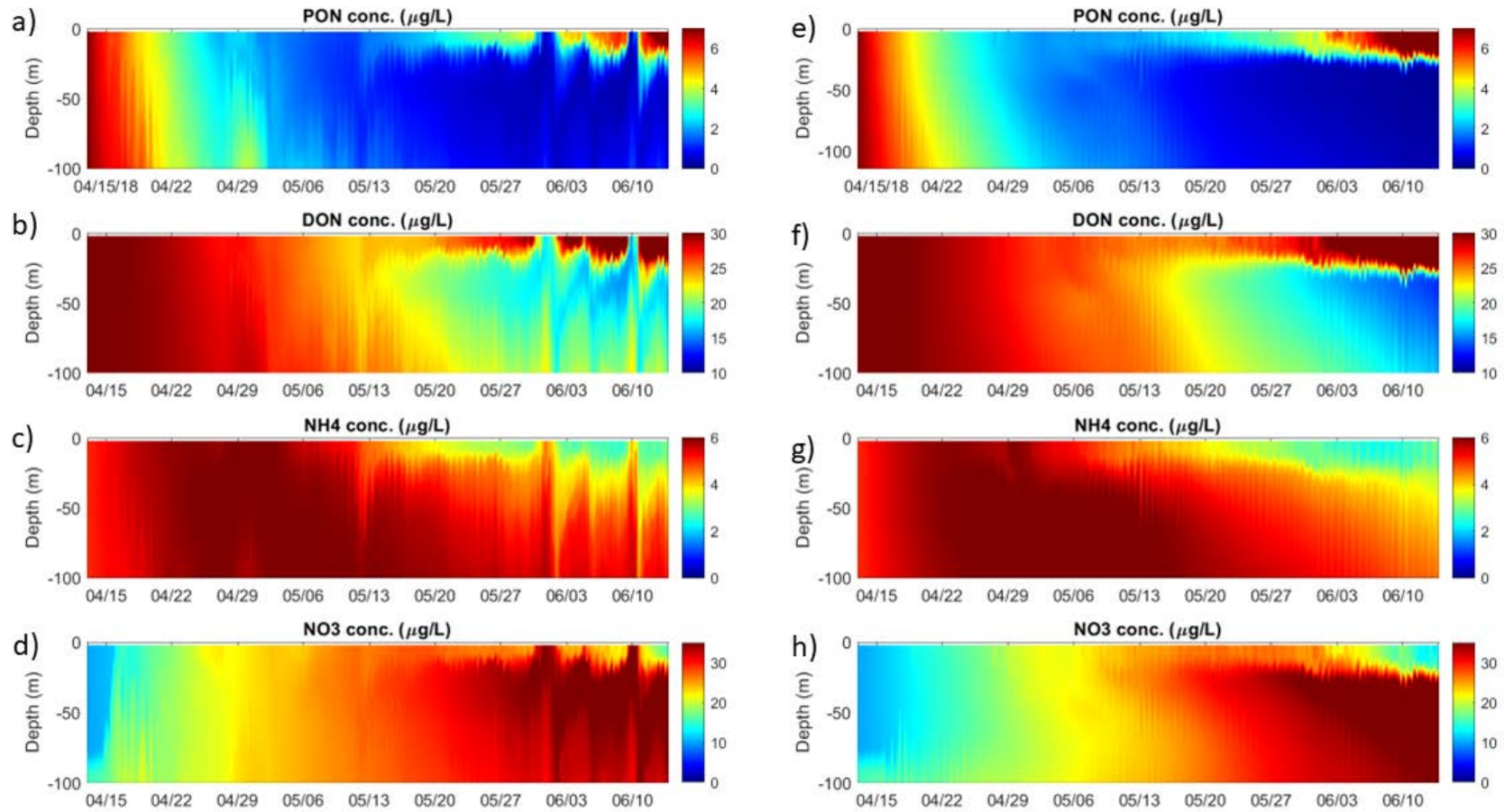


Figure 7-18. Model time series of nitrogen forms: PON (a,e), DON (b,f), NH_4 (c,g), NO_3 (d,h) in spring 2018 in the top 100 m at LTP (a-d) and MLTP (e-h) assuming that growth, mortality and grazing affect the phytoplankton dynamics.

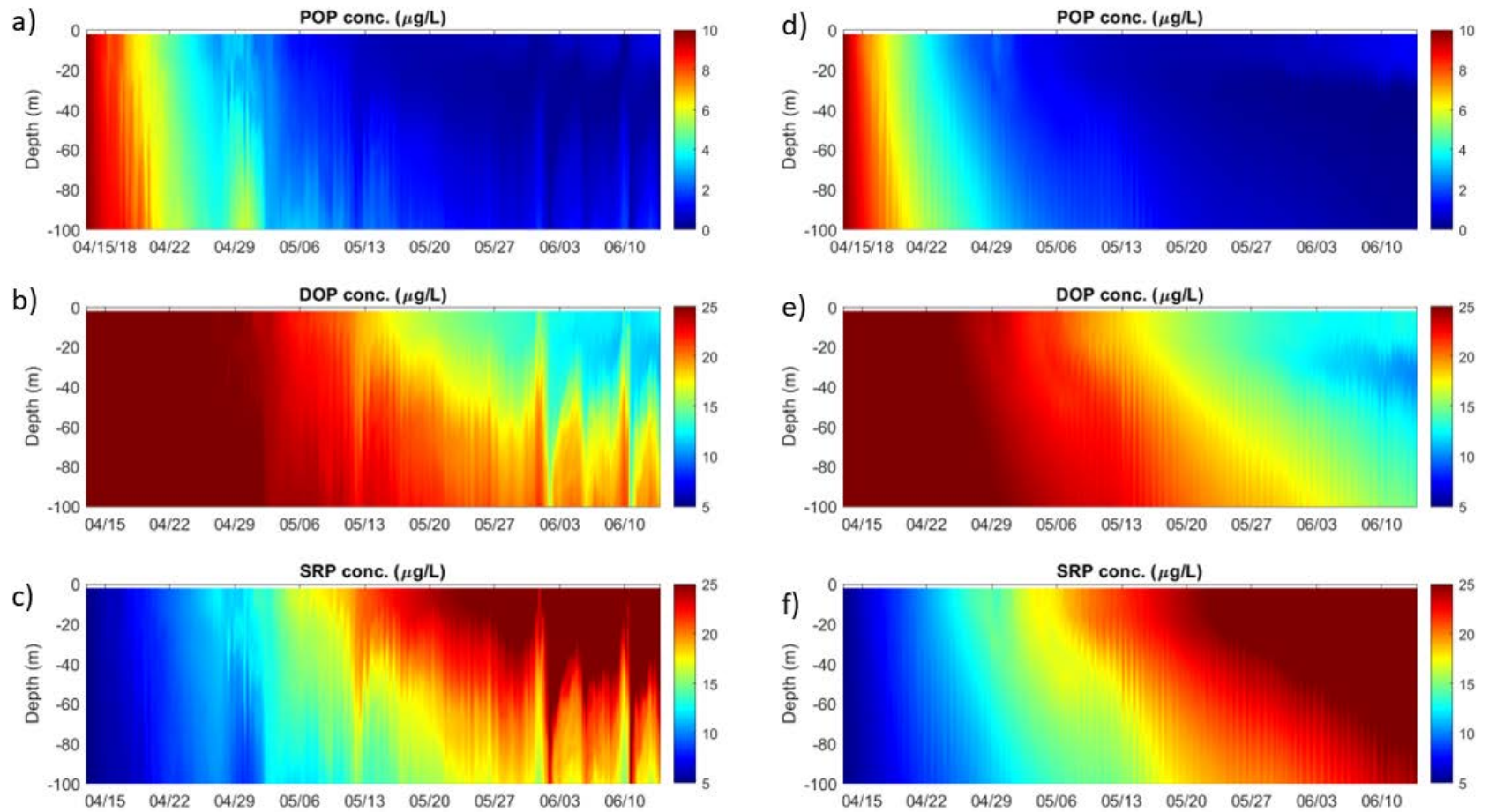


Figure 7-19. Model time series of phosphorus forms: POP (a,d) DOP (b,e), SRP (c,f), in spring 2018 in the top 100 m at LTP (a-e) and MLTP (d-f) assuming that growth, mortality and grazing affect the phytoplankton dynamics.

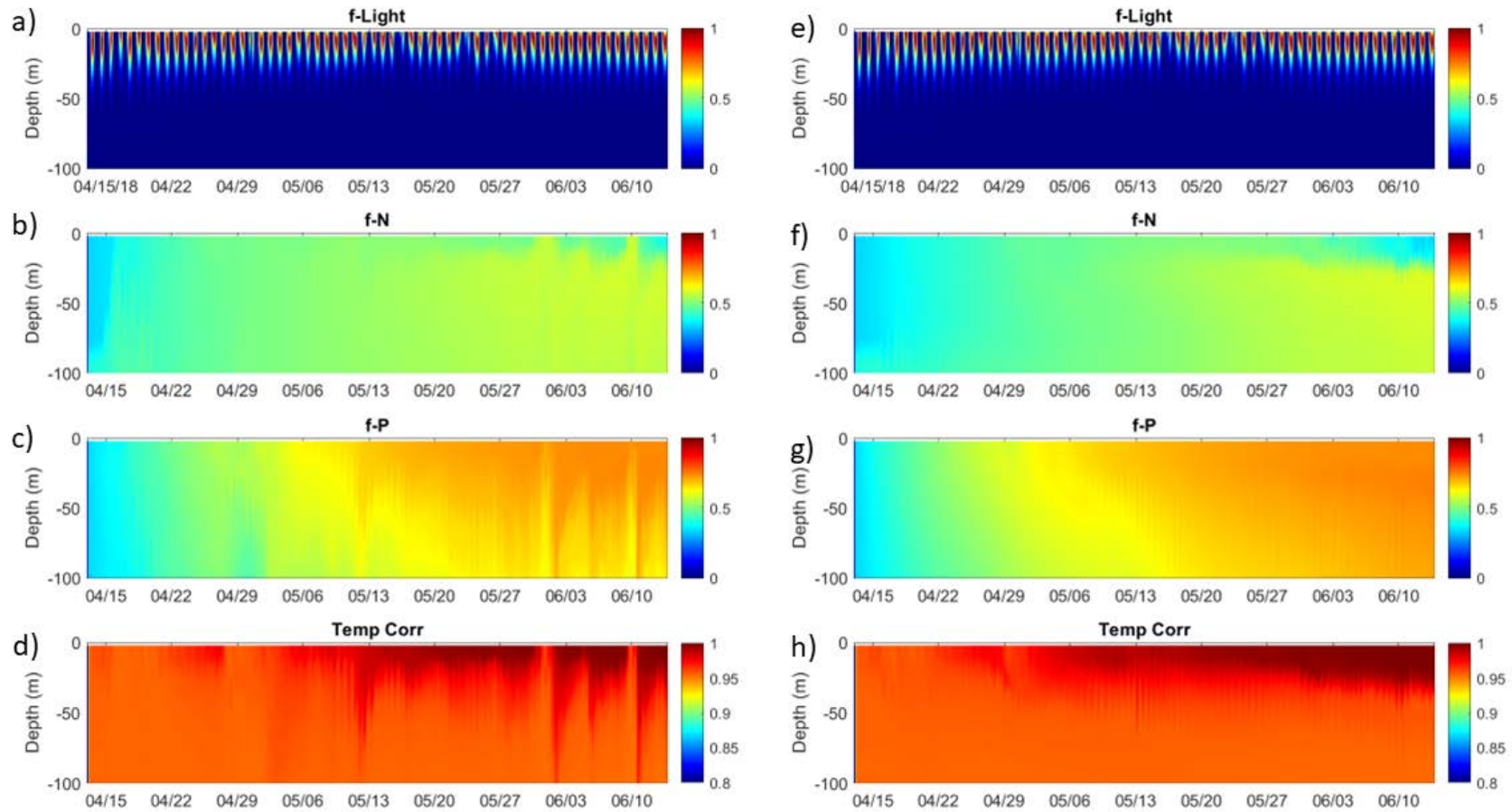


Figure 7-20. Model time series of phytoplankton growth limiting factors: light (a,e), nitrogen (b,f), phosphorus (c,g), temperature (d,h) in spring 2018 in the top 100 m at LTP (a-d) and MLTP (e-h) assuming that growth, mortality and grazing affect the phytoplankton dynamics.

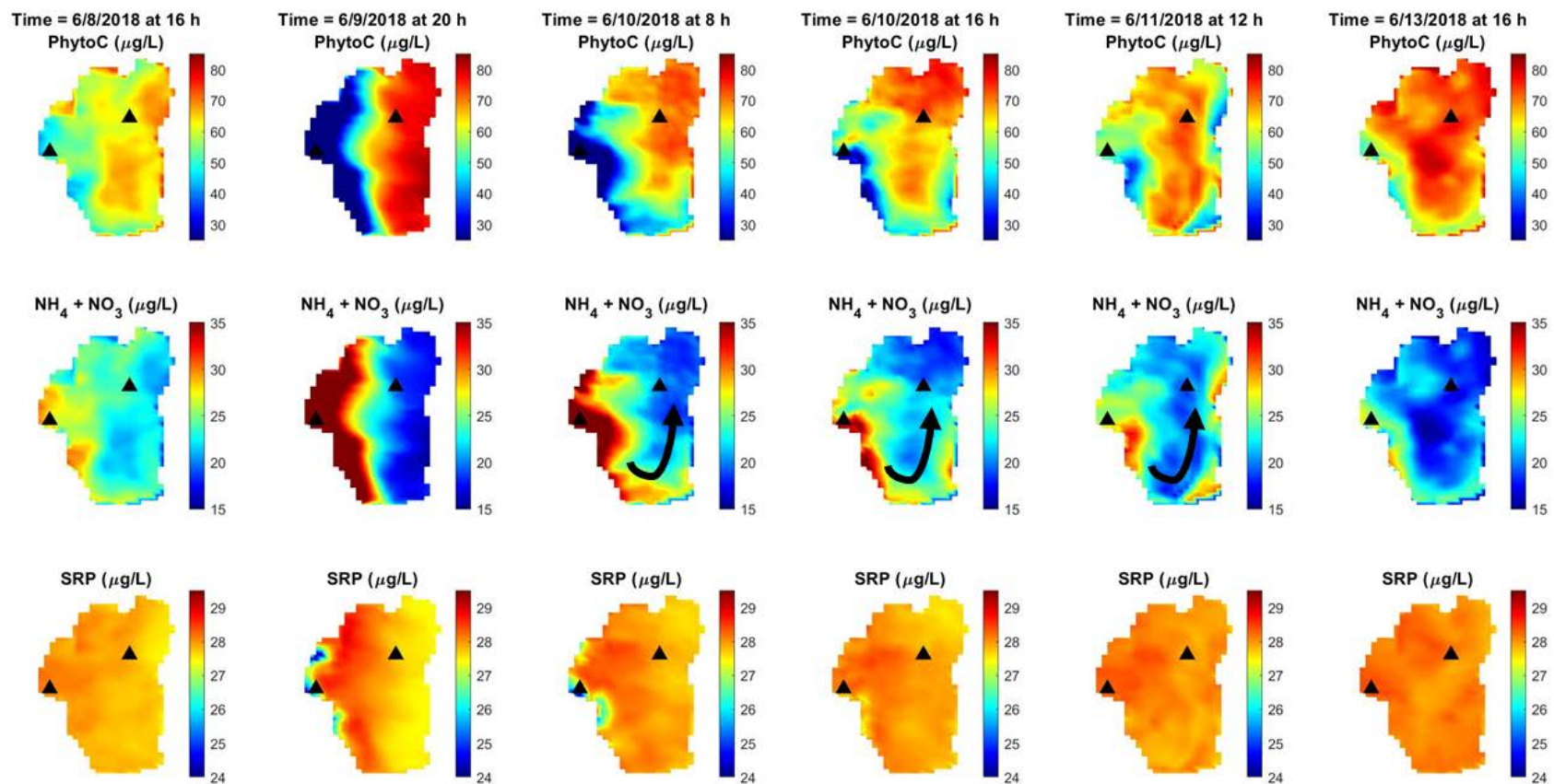


Figure 7-21. Time series of horizontal planes showing average values of different variables in the top 20 m before and after the upwelling event on June 9th. Top panel shows phytoplankton carbon (PhytoC), middle panel shows dissolved inorganic nitrogen ($\text{NH}_4 + \text{NO}_3$) and bottom panel shows soluble reactive phosphorus (SRP). The black arrows in the middle panels indicate the direction of the coastal jet formed due to the upwelling event. The triangles indicate the location of the sampling stations (LTP and MLTP).

Phytoplankton: Growth, Mortality, Grazing and Primary Productivity

To further understand the modeled changes in the phytoplankton concentrations, we explored three scenarios to quantify the relative contribution of the different processes affecting the phytoplankton dynamics (growth, mortality, and grazing). Hence, we have run three different scenarios (or simulations):

- Scenario 1: The source-sink equation that models the rate of change of phytoplankton carbon concentration includes only growth (source). Model outputs from this scenario allowed us to quantify the primary productivity for phytoplankton as a rate of change in phytoplankton carbon concentrations every 4 h (incubation experiment).
- Scenario 2: The source-sink equation that models the rate of change of phytoplankton carbon concentration includes only growth (source) and mortality (sink). By comparing Scenarios 1 and 2, we were able to quantify the relative contribution of mortality to the rate of change in phytoplankton carbon.
- Scenario 3: The source-sink equation that models the rate of change of phytoplankton carbon concentration includes growth (source), mortality, and grazing (sink). Results from this run have been presented in Figure 7-17 to Figure 7-20 (described above). By comparing Scenarios 2 and 3, we were able to quantify the relative contribution of grazing to the rate of change in phytoplankton carbon.

Time series of temporal and spatial changes of phytoplankton carbon, nitrogen forms, phosphorus forms, and limiting factors for scenarios 1 and 2 are shown in Appendix E (Section 14). However, we have used spatially averaged time series of phytoplankton carbon to quantify the relative contribution of each biological process to the rate of change in the phytoplankton community (Figure 7-22). Results show that mortality reduces by more than half (62%) the phytoplankton carbon concentrations while grazing only reduces them by 5%.

Model outputs from Scenario 1 allowed us to quantify the primary productivity for phytoplankton as a rate of change in phytoplankton carbon concentrations every 4 h (incubation experiment) (Figure 7-15). Results show that modeled primary productivity values were of order $5 \text{ mgC/m}^3/4\text{h}$, which matches the order of magnitude of the values measured in the field (Figure 7-23). We also noted that primary productivity doubled right after the upwelling events (June 1 and June 9), probably due to the input of nutrients described in the previous section. In addition, the peak of primary productivity deepened between 10-20 m after each upwelling event. As a result, daily maximum values of primary productive moved from 10 m below the surface at the beginning of the simulations down to 40 m by mid-June.

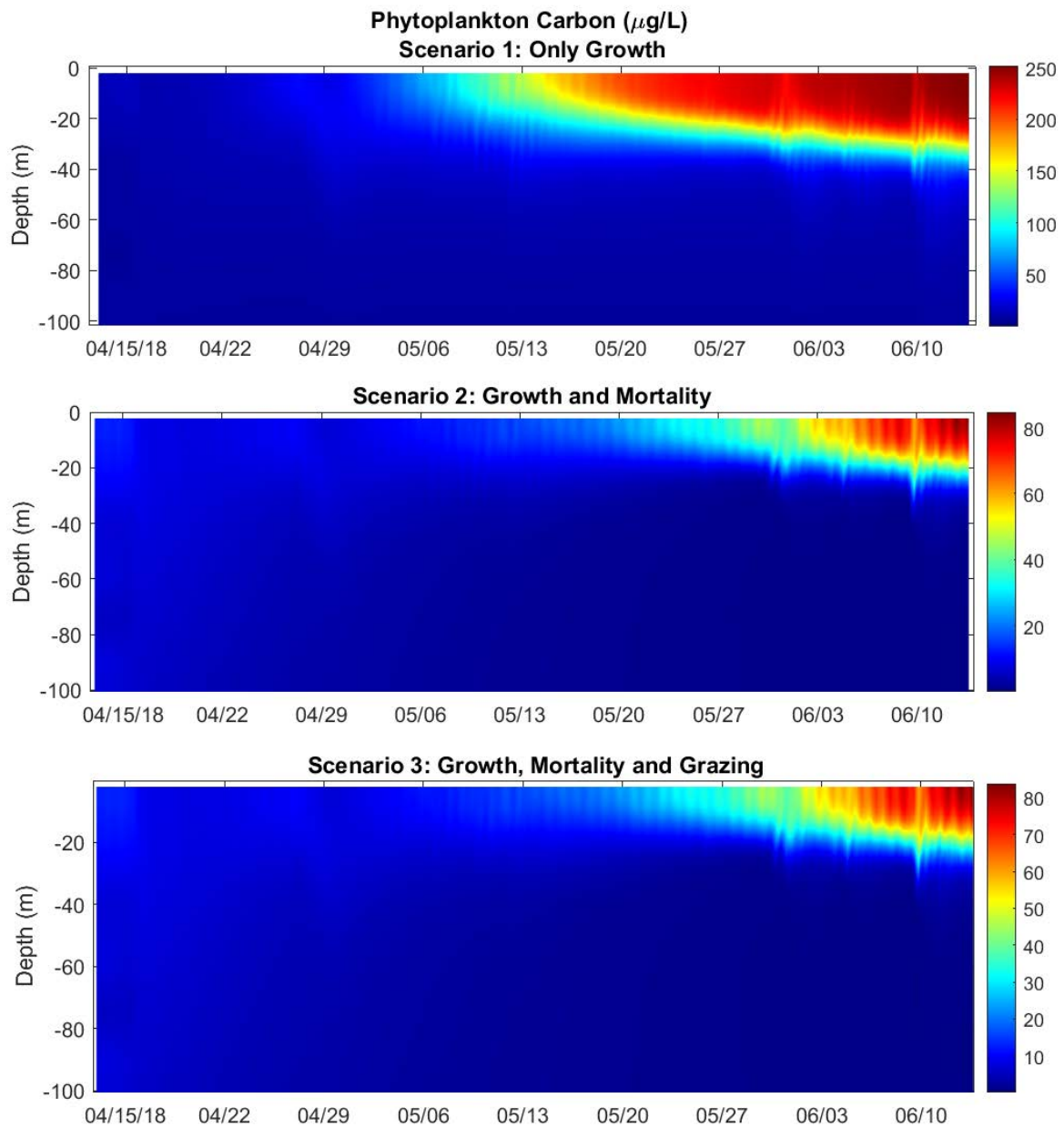


Figure 7-22. Model time series of phytoplankton carbon spatially averaged across the lake in spring 2018 under three different scenarios: (top) scenario 1: only growth; (middle) scenario 2: growth and mortality, (bottom) scenario 3: growth, mortality, and grazing affect the phytoplankton dynamics

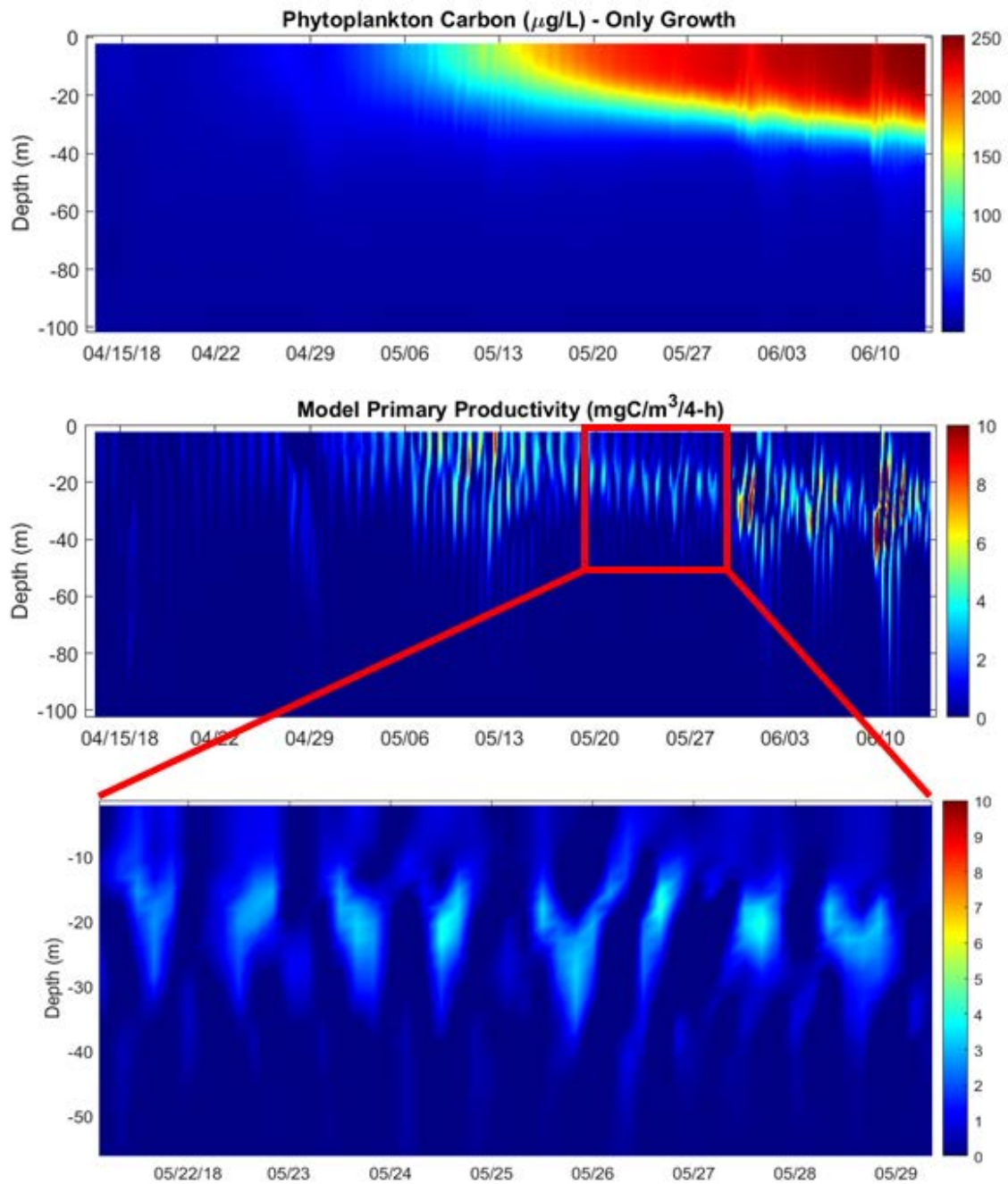


Figure 7-23. (Top) Model time series of phytoplankton carbon spatially averaged across the lake in spring 2018, assuming that only growth affects the phytoplankton dynamics; (Middle) Model time series of primary productivity of phytoplankton using the above phytoC values above; (bottom) Detailed of middle panel marked with the red box

7.2.5. Model results: Developing Scenarios

In the previous section, we have shown the model results of active tracers (phytoplankton carbon and nutrients) due to both hydrodynamic and ecological processes (transport, mixing, decomposition, growth, and others). One process that we have not integrated in the coupled hydrodynamic-ecological model frameworks is the nutrient load from external sources, specifically stream inflows or atmospheric deposition. The proper inclusion of this process requires changes both in the input framework (e.g., how to read stream nutrients), the model parametrizations (e.g., are the model equations correctly reproducing the inflow dynamics) and the testing of nested grid algorithms to provide the necessary resolution to represent inflow dynamics. However, we are able to utilize passive tracers (i.e. only affected by hydrodynamic processes) to provide a qualitative sense of the pathway of the inflow water.

For this scenario, we have used the discharge and stream temperature of Blackwood Creek in spring 2018 as the boundary conditions. We prescribed these conditions on a grid cell at the boundary (200 m wide and 0.5 m deep) close to the Blackwood mount (Figure 7-24). We modeled a continuous injection of a passive tracer of 100 $\mu\text{g/L}$ commencing on 4/13/2018.

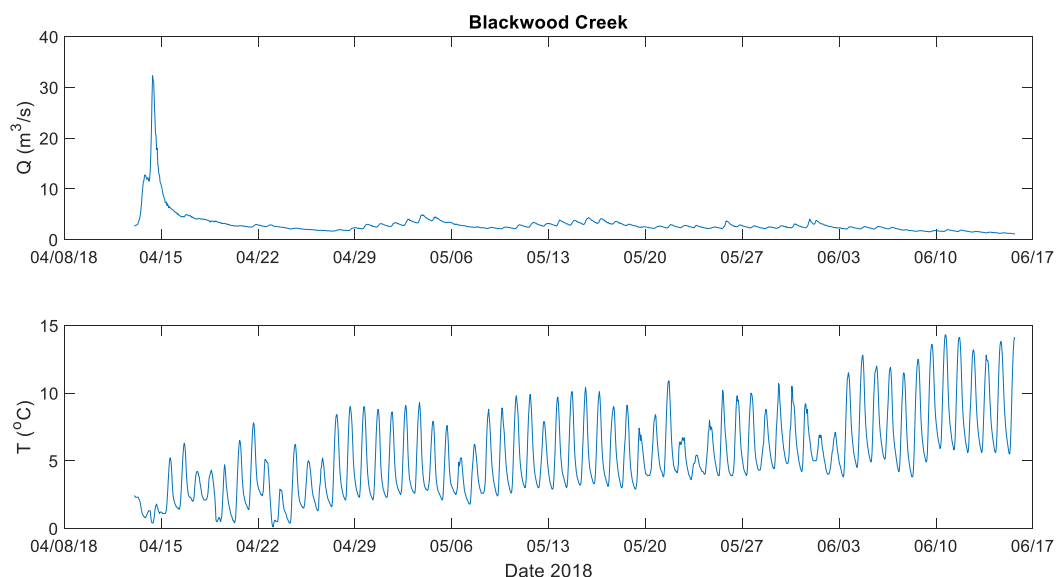


Figure 7-24. Blackwood Creek discharge and stream temperature in spring 2018.

Model results of the passive tracer distribution in the top 30 m show multiple changes in the inflow fate during spring 2018 (Figure 7-25). During late April, the inflow tended to flow south hugging the shoreline. By early May, the flow pattern changed and the water inflow was observed along the north shore. By the end of May, both flow paths occurred simultaneously, so the west shore was significantly affected by inflow water. During early June, the upwelling events contributed to diluting the inflow passive tracer and transporting the dye to the pelagic zone. Even in the earliest stages of the simulation, tracer can be seen to have been transported well away from the region of the stream mouth, and impacting large areas of the lake.

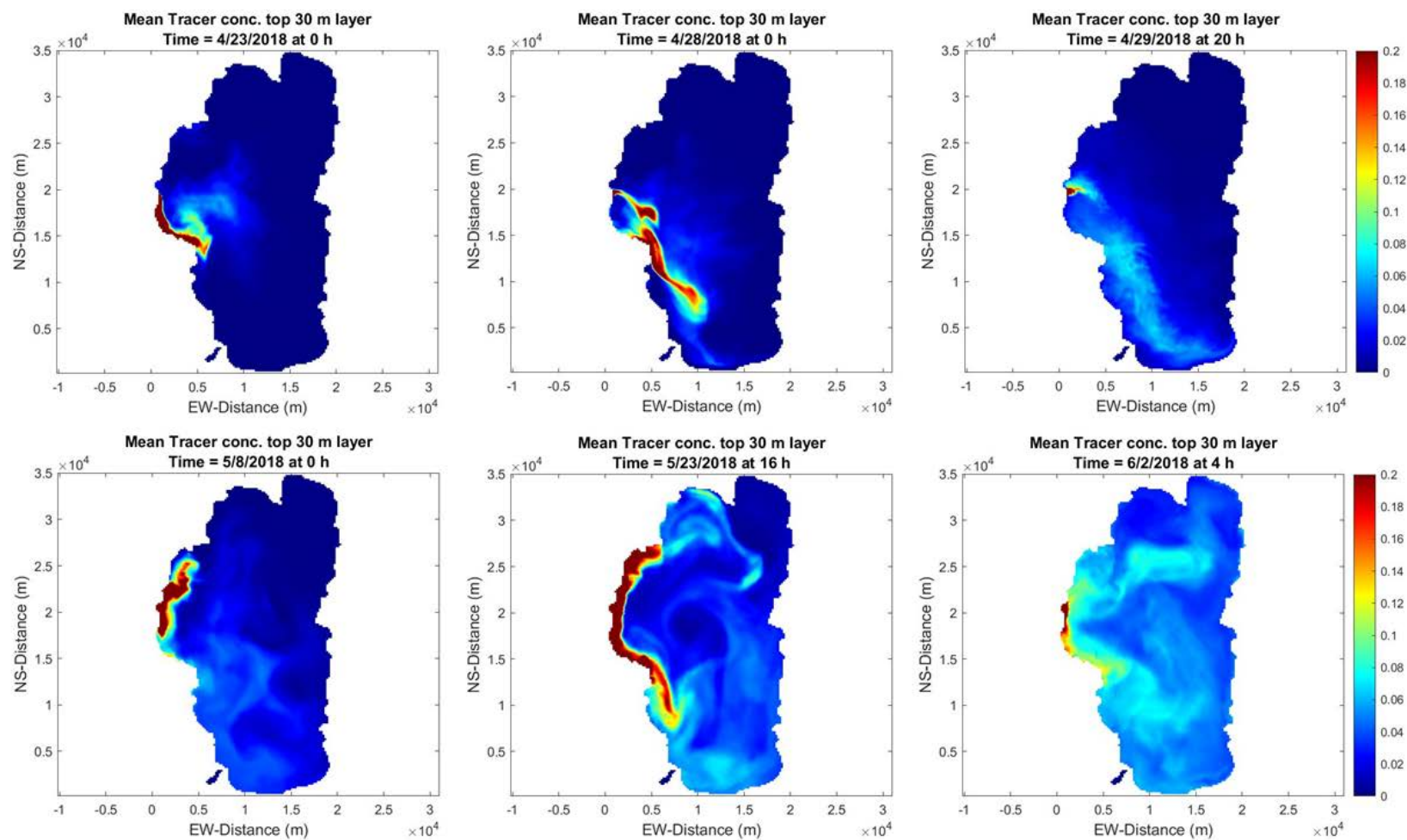


Figure 7-25. Time series of horizontal planes showing average values of a passive tracer injected in Blackwood in the top 30 m in spring 2018.

8. Conclusions

We have calibrated and validated a parallelized three-dimensional (3D) hydrodynamic model (PSi3D) for Lake Tahoe in 2011 and 2018. We have linked this 3D hydrodynamic framework to many ecological processes including phytoplankton dynamics and basic nutrient cycling (carbon, nitrogen, and phosphorus). The ecological model has been calibrated for Lake Tahoe for spring 2018. This coupled hydrodynamic-aquatic ecological model (PSi3D-AEM) is a tool for exploratory testing of future scenarios and their impact on clarity and other water quality variables. In addition, the model is used to evaluate some tasks in need of greater consideration and investment. For example, we have identified deficiencies in the monitoring of zooplankton in space (vertical and horizontal) and time (submonthly to diel), limited measurements of micrograzers or lack of understanding of the microbial loop. Running scenarios with the newly developed PSi3D-AEM will provide insight into the significance of improving our understanding of these and others ecosystem aspects linked to water clarity.

9. Recommendations

We have identified scientific knowledge gaps that limit or constrain the modeling of clarity in Lake Tahoe. The knowledge gaps and accompanying recommendations (that are listed in no specific order) are of two types: data-related and model-related. For some of our data-related recommendations we have limited or nonexistent data for Lake Tahoe (e.g., picoplankton abundance and dynamics; microzooplankton ecology or bacterial loop; the process of deep mixing; stream entrainment processes). Further refinement of our newly developed aquatic ecological model is required to properly simulate clarity in Lake Tahoe. For example, we lumped different processes and omitted others because we did not have data available to develop or test the model.

9.1. Data-related

1) *Automated profiling systems to obtain high-frequency limnological data*

Continuous measurements of limnological parameters have become readily available in the 21st century. We currently measure physical properties such as temperature at a high temporal resolution, but we conduct routine ecological sampling only once a month. Thus, there is a mismatch between physical and ecological sampling frequencies. Moreover, ecological and biogeochemical processes can change rapidly, at daily or hourly time scales. Automated profiling systems can provide a platform for observing phenomena that vary rapidly in depth and time. Such profiling systems can simultaneously measure at a high temporal resolution physical and biological parameters, such as temperature, conductivity, dissolved oxygen, chlorophyll, and CDOM with proven sensors.

Recommendation: Acquire and test the performance of an automated profiling system to increase the temporal resolution of ecological data in Lake Tahoe.

2) *Refining understanding of macro- and micro zooplankton*

Despite the published studies on zooplankton in the 1970s and 1980s, there remains an incomplete understanding of zooplankton abundance, distribution, and species composition, including micrograzers that feed on small particles and bacteria, in space (vertical and horizontal), and time (diel to subseasonal). Zooplankton grazing rates are likely influenced by the variable but low carbon available within the water column and by season. Zooplankton in other low productive ecosystems contribute bioavailable nitrogen through excretion, carbon which supports microbial activity, and may influence the aggregation of particles. Future work should develop a contemporary understanding of the zooplankton community in Lake Tahoe, including micrograzers, and their grazing, egestion, and excretion of particles and algae, nutrient cycling, and population regulation. This can be accomplished by a robust field monitoring program that incorporates appropriate scales of space and time, semi-natural field experiments, and modeling.

Recommendation: We recommend focused studies on the ecology of the zooplankton community, diel vertical and horizontal distributions, the development of complementary bioenergetic models, and experiments to quantify zooplankton grazing, nutrient excretion, carbon egestion, and feedbacks to phytoplankton and microbial activity. Novel (eDNA, genome sequencing, visual imaging) and traditional techniques (counts) that account for relative dominance and species traits should be coupled with seminatural experiments to understand carbon transformation and flows in the lower food. The

restoration of funding for zooplankton monitoring plus the addition of micrograzers (ciliates and rotifers) should be included in long-term monitoring.

3) Measurements of bacteria and other aspects of nutrient cycles

The conceptual models described in Section 7.2.2 have not been fully implemented in PSi3D-AEM due to a lack of data on some of the state variables such as bacteria or the rates of specific processes related to the microbial loop (note processes in red in Figure 7-8 to Figure 7-11).

Recommendation: Both field collections to quantify the amount and types of microbes (by season, depth, and horizontal distribution), and laboratory experiments to understand nutrient cycling and the microbial loop and zooplankton grazing interactions are needed. Contemporary techniques including metagenomics, eDNA, and experimental studies, should be employed in the nearshore and offshore waters of Lake Tahoe. If combined with appropriate measurements and models of hydrologic and hydrodynamic fluxes, mass balance calculations may provide a complementary approach to evaluating nutrient cycling.

4) Measurements of picoplankton

Long-term or ongoing measurements of picoplankton counts and their contribution to primary productivity and phytoplankton biomass are not available. Previous studies indicate that picoplankton can contribute 30-60% of the primary productivity of phytoplankton in Lake Tahoe, they are in a critical size range that impacts clarity, and their exudates may contribute to particle aggregation.

Recommendation: Employ appropriate techniques, such as epifluorescence microscopy and flow cytometry, for the detection and enumeration of picoplankton and determine their contribution to primary productivity.

5) Fundamental understanding of primary productivity

We lack understanding of variations in primary productivity and phytoplankton carbon concentrations. Multi-variable analyses of primary productivity, chlorophyll-a, phytoplankton carbon content, lake stratification, and amount of light would provide valuable insights.

Recommendation: Analyze existing data to gain an improved understanding of relations between primary productivity and phytoplankton carbon concentrations through the water column, and the factors driving their dynamics seasonally and interannually. Most data are available, but the analyses required are underfunded.

6) Sampling at multiple locations

Lakes are complex, three-dimensional systems with vertical and horizontal variations in physical, chemical, and biological processes and conditions occurring across a range of temporal scales. Suspended sediment and phytoplankton, that alter clarity, are transported and dispersed by physical processes, and the growth of phytoplankton is influenced by mixing, availability of nutrients, and light climate. As a result, the complexity of these and other dynamics are not represented by the current monitoring program, although they would be in part enhanced by an automated profiling system (Recommendation 1). For example, our modeling results illustrate the dispersal of stream inflows (Figure 7-25) and the influence of upwelling (Figure 7-21).

Recommendation: Conduct intensive and strategic monitoring and focused studies guided by hydrodynamic and ecological modeling.

9.2. Model-related

1) *Optical submodel*

The current optical submodel provides a mechanistic link between concentrations of dissolved and particulate matter and water clarity. The optical model calculates the scattering and absorption characteristics of the water and its constituents (particulate organic, particulate inorganic, and dissolved matter) based on particle size distributions, composition, and concentration, and then calculates the Secchi depth from the inherent optical properties. Inorganic particles are separated within 7 size ranges; organic particles (phytoplankton) are parameterized as chlorophyll-a concentration, and colored dissolved organic matter (CDOM) and pure water appear as constants. The particle aggregation model (a key component of clarity) uses a fractal approach (Jassby 2006). This approach is computationally intensive, and simplifying assumptions are made to enable it to operate in the 1-D model framework.

Recommendation: Implement an updated optical submodel in the newly developed PSi3D-AEM, with an emphasis on better characterizing aggregation processes.

2) *Scenario testing*

The newly developed PSi3D-AEM is a tool for the exploration of future scenarios and their impact on clarity and can guide revised sampling, measurements, and experiments.

Recommendation: Run hypothetical scenarios to evaluate the potential magnitude and role of the varied ecological and physical conditions on Lake Tahoe and its clarity.

3) *Deep mixing, dissolved oxygen dynamics, and sediment nutrient release*

Deep mixing and the associated oxygen transfer are believed to be controlled by differential convection from the shallow shelves at the margins of the lake. The 3-D hydrodynamic model developed in this project provides a tool to help understand and quantify this transfer. No algorithms currently exist to represent this important process.

Recommendation: Develop, test and implement a deep mixing model for Lake Tahoe, with associated dissolved oxygen transfer and sediment nutrient fluxes.

4) *Fate of streams, groundwater, and urban stormwater inflow*

Modeling the movement, dispersion, and fate of stream, groundwater, and urban stormwater inflows after they enter Lake Tahoe under a range of lake stratification, lake level, snowpack, and inflow conditions was not part of the current scope of work. Adding this aspect to the model would help agencies to prioritize their future investments in stormwater monitoring, modeling, and project implementation. The connectivity of the pelagic and littoral zones cannot be understood without better algorithms for these processes

Recommendation: Add to PSi3D-AEM implementation in Lake Tahoe, the movement, dispersion, and fate of stream, groundwater, and urban stormwater inflows under a range of lake stratification, lake level, snowpack, and inflow conditions.

5) Zooplankton population dynamics

Zooplankton grazing and nutrient cycling influence phytoplankton carbon dynamics and species composition, microbial activity, and the fate of inorganic and organic particles. To model zooplankton population abundances and movements requires a better understanding of zooplankton composition including sizes and life-history stages and estimations for grazing, excretion, and egestion. Models such as PSi3D-AEM are not designed to do this type of modeling and investments in bioenergetic and population models for zooplankton would be required

Recommendation: Develop specific zooplankton bioenergetics and/or population models for zooplankton that incorporate changes in abundance, food supply, and temperature for estimations of nutrient excretion and grazing. Model inputs will require field collections in space (horizontal and vertical) and time, food supply, and temperature. Experiments with each taxon may be required.

10. Appendix A: Literature review of physiological parameters of phytoplankton

Table 10-1. Literature review of physiological parameters of phytoplankton. References are provided in a separate table.

Parameter	Unit	Value	Assigned Functional Group	Studied organism	Source
Cell nutrient quotas (N) (minimum)	$\mu\text{moles cells}^{-1}$	1×10^{-7}	cyanobacteria	cyanobacteria: <i>Anabaena sp</i>	Lehman 1975
Cell nutrient quotas (N) (minimum)	$\mu\text{moles cells}^{-1}$	1.8×10^{-8}	flagellate	flagellate: <i>Dinobryon sp</i>	Lehman 1975
Cell nutrient quotas (N) (minimum)	$\mu\text{moles cells}^{-1}$	3.9×10^{-7}	flagellate	flagellate: <i>Gymnodinium sp</i>	Lehman 1975
Cell nutrient quotas (N) (minimum)	$\mu\text{moles cells}^{-1}$	6×10^{-7}	large diatom	diatom: <i>Asterionella formosa</i>	Grim 1939 cited by Lehman 1975
Cell nutrient quotas (P) (minimum)	$\mu\text{moles cells}^{-1}$	1.5×10^{-9}	large diatom	diatom: <i>Asterionella formosa</i>	Mackereth 1953 cited by Lehman 1975
Cell nutrient quotas (P) (minimum)	$\mu\text{moles cells}^{-1}$	0.9×10^{-9}	small diatom	marine diatom: <i>Cyclotella nana</i>	Fuhs 1969 cited by Lehman 1975
Cell nutrient quotas (Si) (minimum)	$\mu\text{moles cells}^{-1}$	2×10^{-6}	large diatom	diatom: <i>Asterionella formosa</i>	Hughes and Lund 1962
Cell nutrient quotas (Si) (minimum)	$\mu\text{moles cells}^{-1}$	4×10^{-6}	large diatom	diatom: <i>Fragilaria crotonensis</i>	Lehman 1975
Cell nutrient quotas (Si) (minimum)	$\mu\text{moles cells}^{-1}$	3×10^{-7}	large diatom	diatom: <i>Nitzschia alba</i>	Lewin and Chen 1968
Cell nutrient quotas (Si) (minimum)	$\mu\text{moles cells}^{-1}$	2×10^{-8}	small diatom	diatom: <i>Thalassiosira pseudonana</i>	Paasche 1973a
Density of particulate nutrients	kg m^{-3}	1.08			Ambrose 1988
Density of particulate organic matter		1.07	green-algae	green-algae: <i>Scenedesmus dominated</i>	Jorgensen 1978
Density of particulate organic matter	kg m^{-3}	1.08			Ambrose 1988
Density of particulate organic matter		1.08			Ambrose 1988
Excretion rate (C excreted)	$\text{pg C cell}^{-1} \text{d}^{-1}$	4.0	flagellate	flagellate: <i>Cryptomonas erosa</i>	Morgan and Kalff 1979
Excretion rate (C excreted)	$\text{pg C cell}^{-1} \text{d}^{-1}$	3.5	flagellate	flagellate: <i>Cryptomonas erosa</i>	Morgan and Kalff 1979
Excretion rate (C excreted)	$\text{pg C cell}^{-1} \text{d}^{-1}$	7.8	flagellate	flagellate: <i>Cryptomonas erosa</i>	Morgan and Kalff 1979
Excretion rates of algae (maximum)	d^{-1}				
Growth rate of algae	d^{-1}	1.35	large diatom	marine diatom	Eppeley 1971
Growth rate of algae	d^{-1}	1.16	large diatom	marine diatom	Eppeley 1971
Growth rate of algae	d^{-1}	1.36 – 1.52	large diatom	diatom: <i>Nitzschia closterium</i>	Eppeley 1971
Growth rate of algae (maximum)	d^{-1}	0.48	flagellate	flagellate: <i>Gymnodinium splendens</i>	Thomas 1974
Growth rate of algae (maximum)	d^{-1}	0.16	green-algae	green-algae: <i>Selenastrum gracile</i>	Middlebrooks 1971
Growth rate of algae (maximum)	d^{-1}	0.43	green-algae	green-algae: <i>Selenastrum gracile</i>	Middlebrooks 1971
Growth rate of algae (maximum)	d^{-1}	2.3 and 2.53	green-algae	green-algae: <i>Scenedesmus dominated</i>	Jorgensen 1978
Growth rate of algae (maximum)	d^{-1}	0.67	large diatom	diatom: <i>Nitzschia closterium</i>	Di Toro 1971
Growth rate of algae (maximum)	d^{-1}	1.55	large diatom	diatom: <i>Nitzschia closterium</i>	Di Toro 1971
Growth rate of algae (maximum)	d^{-1}	1.19	large diatom	diatom: <i>Nitzschia closterium</i>	Di Toro 1971
Growth rate of algae (maximum)	d^{-1}	2.5	(estuarine algae)	phytoplankton	O'Connor 1975
Growth rate of algae (maximum)	d^{-1}	1.3	(freshwater algae)	freshwater algae	O'Connor 1975
Growth rate of algae (maximum)	d^{-1}	2.1	(freshwater algae)	freshwater algae	O'Connor 1975
Growth rate of algae (maximum)	d^{-1}	0.58	(freshwater algae)	freshwater algae	Thomann 1975
Growth rate of algae (maximum)	d^{-1}	1.6 – 2.1			Canale 1976 cited by Hamilton and Schladow 1997

Growth rate of algae (maximum)	d ⁻¹	1.3 – 2.5			O'Connor 1976 cited by Hamilton and Schladow 1997
Growth rate of algae (maximum)	d ⁻¹	1.8 – 3.9			O'Connor 1973
Growth rate of algae (maximum)	d ⁻¹	2			Ambrose 1988
Half saturation constant for N uptake	mg m ⁻³	200	green-algae	green-algae: <i>Scenedesmus</i> dominated	Jorgensen 1978
Half saturation constant for N uptake	mg m ⁻³	25			Ambrose 1988
Half saturation constant for NH ₄ growth	μmoles/L	0.4	small diatom	marine diatom: <i>Cyclotella nana</i>	Eppeley 1969
Half saturation constant for NH ₄ uptake	μM	1.1	flagellate	flagellate: <i>Gymnodinium splendens</i>	Lehman 1975
Half saturation constant for NH ₄ uptake	μM	0.4	small diatom	marine diatom: <i>Cyclotella nana</i>	Lehman 1975
Half saturation constant for NO ₃ growth	μmoles/L	70	cyanobacteria	cyanobacteria: <i>Anabaena cylindrica</i>	Hattori 1962
Half saturation constant for NO ₃ growth	μmoles/L	0.4 – 1.9	small diatom	marine diatom: <i>Cyclotella nana</i>	Carpenter, 1971
Half saturation constant for NO ₃ uptake	μM	3.8	flagellate	flagellate: <i>Gymnodinium splendens</i>	-
Half saturation constant for NO ₃ uptake	μM	0.4 – 1.9	small diatom	marine diatom: <i>Cyclotella nana</i>	Carpenter and Guillard 1971
Half saturation constant for NO ₃ uptake	μM	0.5	small diatom	marine diatom: <i>Cyclotella nana</i>	Eppeley et al 1969
Half saturation constant for P growth	μg/L	10	(freshwater algae)	freshwater algae	O'Connor 1975
Half saturation constant for P growth	μg/L	2	(freshwater algae)	freshwater algae	O'Connor 1975
Half saturation constant for P uptake	μmoles/L	0.42	flagellate	flagellate: <i>Dinobryon sociale</i> var. <i>americanum</i>	Lehman 1976
Half saturation constant for P uptake	mg/L	0.002	(freshwater algae)	freshwater algae	Thomann 1975
Half saturation constant for P uptake	μM	0.24	(freshwater algae)	freshwater algae	Halmann 1974
Half saturation constant for P uptake	μmoles/L	0.58	small diatom	marine diatom: <i>Cyclotella nana</i>	Fuhs 1972 cited by Jorgensen 1979
Half saturation constant for P-limited growth	μM	0.02	large diatom	diatom: <i>Asterionella formosa</i>	Tilman and Kilham 1976
Half saturation constant for P-limited growth	μM	0.25	large diatom	diatom: <i>Cyclotella meneghiniana</i>	Tilman and Kilham 1976
Half saturation constant for PO ₄ uptake	μM	0.8	flagellate	flagellate: <i>Dinobryon cylindricum</i>	Lehman 1975
Half saturation constant for PO ₄ uptake	μM	0.5	flagellate	flagellate: <i>Dinobryon sociale</i> var. <i>americanum</i>	Lehman 1975
Half saturation constant for PO ₄ uptake	μM	1.1	green-algae	green-algae: <i>Pediastrum duplex</i>	Lehman unpublished
Half saturation constant for PO ₄ uptake	μM	0.6	green-algae	green-algae: <i>Scenedesmus</i> sp.	Rhee 1973
Half saturation constant for PO ₄ uptake	μM cells ⁻¹ h ⁻¹	8 x 10 ⁻⁸	large diatom	diatom: <i>Asterionella formosa</i>	Mackereth 1953 cited by Jorgensen 1979
Half saturation constant for Si uptake	μM	3.5	large diatom	diatom: <i>Nitzschia actinastreoides</i>	Muller 1972
Half saturation constant for Si uptake	μM cells ⁻¹ h ⁻¹	2.5 – 5.7 x 10 ⁻⁸	large diatom	diatom: <i>Nitzschia alba</i>	Lewin and Chen 1968
Half saturation constant for Si-limited (SiO ₂ -Si) growth	μM	3.94	large diatom	diatom: <i>Asterionella formosa</i>	Tilman and Kilham 1976
Half saturation constant for Si-limited (SiO ₂ -Si) growth	μM	1.44	large diatom	diatom: <i>Cyclotella meneghiniana</i>	Tilman and Kilham 1976
Half saturation constant for Si-limited growth	μM	8.3	small diatom	marine diatom: <i>Cyclotella</i> sp.	Taguchi et al. 1987
Half-saturation constant for P uptake	mg L ⁻¹	0.006	cyanobacteria	freshwater cyanobacteria: <i>Microcystis aeruginosa</i>	Holm and Armstrong 1981
Half-saturation constant for P uptake	mg L ⁻¹	0.01	large diatom	diatom: <i>Asterionella formosa</i>	Holm and Armstrong 1981
Internal N concentration (maximum)	mg N(mg chl a) ⁻¹	20	green-algae	green-algae: <i>Scenedesmus</i> dominated	Jorgensen 1978
Internal N concentration (minimum)	mg N(mg chl a) ⁻¹	1.5	green-algae	green-algae: <i>Scenedesmus</i> dominated	Jorgensen 1978
Internal P concentration (minimum)	mg P(mg chl a) ⁻¹	1.3	green-algae	green-algae: <i>Scenedesmus</i> dominated	Jorgensen 1978
Internal P concentration (minimum)	mg P(mg chl a) ⁻¹	0.1	green-algae	green-algae: <i>Scenedesmus</i> dominated	Jorgensen 1978

Irradiance parameter non-photoinhibited growth	$\mu\text{E m}^{-2} \text{s}^{-1}$	120	cyanobacteria	freshwater cyanobacteria: <i>Microcystis aeruginosa</i>	Burger 2008
Irradiance parameter non-photoinhibited growth	$\mu\text{E m}^{-2} \text{s}^{-1}$	200	green-algae		Robson and Hamilton (2004)
Irradiance parameter non-photoinhibited growth	$\mu\text{E m}^{-2} \text{s}^{-1}$	500	cyanobacteria	freshwater cyanobacteria: <i>Microcystis aeruginosa</i>	Robson and Hamilton (2004)
Irradiance parameter non-photoinhibited growth	$\mu\text{E m}^{-2} \text{s}^{-1}$	380	(marine algae)		Robson and Hamilton (2004)
Irradiance parameter non-photoinhibited growth	$\mu\text{E m}^{-2} \text{s}^{-1}$	180	flagellate	dinoflagellates	
Mortality	h^{-1}	0.004	(freshwater algae)	freshwater algae	Richey 1977 cited by Jorgensen 1979
Photoinhibited saturation irradiance	$\mu\text{E m}^{-2} \text{s}^{-1}$	200	cyanobacteria	freshwater cyanobacteria: <i>Microcystis aeruginosa</i>	Wallace and Hamilton 1999
Rate coefficient for mineralisation of organic N	d^{-1}	0.05 – 0.3	green-algae	green-algae: <i>Scenedesmus</i> dominated	Jorgensen 1978
Rate coefficient for mineralization of organic N	d^{-1}	0.25 and 0.4	green-algae	green-algae: <i>Scenedesmus</i> dominated	Jorgensen 1978
Rate coefficient for mineralization of organic N	d^{-1}	0.22			Ambrose 1988
Rate coefficient for nitrification	d^{-1}	0.02	green-algae	green-algae: <i>Scenedesmus</i> dominated	Jorgensen 1978
Rate coefficient for respiration	d^{-1}	0.088 and 0.13	green-algae	green-algae: <i>Scenedesmus</i> dominated	Jorgensen 1978,
Rate coefficient for respiration	d^{-1}	0.09	green-algae	green-algae: <i>Scenedesmus</i> dominated	Jorgensen 1978
Rate coefficient for respiration	d^{-1}	0.015			Gargas 1976 cited by Hamilton and Schladow 1997
Rate coefficient for respiration	d^{-1}	0.05 – 0.10			Andersen 1974
Rate coefficient for respiration	d^{-1}	0.02			Ambrose 1988
Rate coefficient for respiration	d^{-1}	0.02 – 0.16			Larsen 1976 cited by Hamilton and Schladow 1997
Saturating light intensity	$\mu\text{Em}^{-2}\text{s}^{-1}$	105 – 697			Lehman 1975
Settling velocity	m d^{-1}	0.001	(detritus)	detritus	Thomann 1975
Settling velocity	m d^{-1}	0 – 30	(marine algae)	phytoplankton	Smayda 1970
Settling velocity	m d^{-1}	4.32	cyanobacteria	cyanobacteria	Romero 2004 cited by Burger 2008
Settling velocity	m d^{-1}	0.31 +- 0.32	flagellate	flagellate: <i>Cryptomonas erosa</i>	Burns and Rosa 1980
Settling velocity	m d^{-1}	0.2 – 0.4	flagellate	flagellate: <i>Dinobryon sertularia</i>	Grim 1952 cited by Margalef 1961
Settling velocity	m d^{-1}	0.07 +- 0.21	flagellate	flagellate: <i>Rhodomonas minuta</i>	Burns and Rosa 1980
Settling velocity	m d^{-1}	0.32 +- 0.32	flagellate	flagellate: <i>Cryptomonas marsonii</i>	Burns and Rosa 1980
Settling velocity	m d^{-1}	0.18 +- 0.11	green-algae	green-algae: <i>Closterium parvulum</i>	Burns and Rosa 1980
Settling velocity	m d^{-1}	0.15 +- 0.13	green-algae	green-algae: <i>Selenastrum minutum</i>	Burns and Rosa 1980
Settling velocity	m d^{-1}	0.40 +- 0.28	large diatom	diatom: <i>Asterionella formosa</i>	
Settling velocity	m d^{-1}	0.09	large diatom	diatom: <i>Asterionella formosa</i>	Smayda 1974; Titman and Kilham 1976
Settling velocity	m d^{-1}	0.63	large diatom	diatom: <i>Asterionella formosa</i>	Smayda 1974; Titman and Kilham 1976
Settling velocity	m d^{-1}	0.22 – 0.61	large diatom	diatom: <i>Asterionella formosa</i>	Smayda 1974
Settling velocity	m d^{-1}	0.32	large diatom	diatom: <i>Asterionella formosa</i>	Smayda 1974
Settling velocity	m d^{-1}	0.7	large diatom	diatom: <i>Asterionella formosa</i>	Fritz 1935 cited by Margalef 1961
Settling velocity	m d^{-1}	1.0	large diatom	diatom: <i>Asterionella formosa</i>	Fritz 1935 cited by Margalef 1961

Settling velocity	m d ⁻¹	2.9	large diatom	diatom: <i>Asterionella formosa</i>	Fritz 1935 cited by Margalef 1961
Settling velocity	m d ⁻¹	1.4	large diatom	diatom: <i>Cyclotella bodanica</i> (renamed as <i>Lindavia bodanica</i>)	Fritz 1935 cited by Margalef 1961
Settling velocity	m d ⁻¹	1.9	large diatom	diatom: <i>Cyclotella bodanica</i> (renamed as <i>Lindavia bodanica</i>)	Fritz 1935 cited by Margalef 1961
Settling velocity	m d ⁻¹	5.3	large diatom	diatom: <i>Cyclotella bodanica</i> (renamed as <i>Lindavia bodanica</i>)	Fritz 1935 cited by Margalef 1961
Settling velocity	m d ⁻¹	0.27 +- 0.13	large diatom	diatom: <i>Fragilaria crotonensis</i>	-
Settling velocity	m d ⁻¹	0.43 +- 0.22	large diatom	diatom: <i>Fragilaria crotonensis</i>	Reynolds 1976
Settling velocity	m d ⁻¹	0.5	large diatom	diatom: <i>Fragilaria crotonensis</i>	Fritz 1935 cited by Margalef 1961
Settling velocity	m d ⁻¹	1.0	large diatom	diatom: <i>Fragilaria crotonensis</i>	Fritz 1935 cited by Margalef 1961
Settling velocity	m d ⁻¹	3.8	large diatom	diatom: <i>Fragilaria crotonensis</i>	Fritz 1935 cited by Margalef 1961
Settling velocity	m d ⁻¹	0.6 – 1.5	large diatom	diatom: <i>Fragilaria crotonensis</i>	Grim 1952 cited by Margalef 1961
Settling velocity	m d ⁻¹	2.5 – 7 (– 10)	large diatom	diatom: <i>Fragilaria crotonensis</i>	Grim 1952 cited by Margalef 1961
Settling velocity	m d ⁻¹	0.5 – 4.5	large diatom	diatom: <i>Synedra acus delicadissima</i>	Grim 1939 cited by Margalef 1961
Settling velocity	m d ⁻¹	0.39	large diatom	diatom: <i>Tabellaria flocculosa</i>	Smayda 1974
Settling velocity	m d ⁻¹	1.29	large diatom	diatom: <i>Tabellaria flocculosa</i>	Smayda 1974
Settling velocity	m d ⁻¹	0.08 +- 0.10	large diatom	diatom: <i>Cyclotella meneghiniana</i>	Titman 1976
Settling velocity	m d ⁻¹	0.24 +- 0.31	large diatom	diatom: <i>Cyclotella meneghiniana</i>	Titman 1976
Settling velocity	m d ⁻¹	0.1 – 0.27	(freshwater algae)	freshwater algae	Snodgrass 1975
Settling velocity	m d ⁻¹	0.1	(freshwater algae)	freshwater algae	Thomann 1975
Settling velocity	m d ⁻¹	0.1 – 0.4	(freshwater algae)	freshwater algae	Imboden 1974
Settling velocity	m d ⁻¹	0.5 – 0.8	small diatom	diatom: <i>Cyclotella compta</i>	Grim 1952 cited by Margalef 1961
Settling velocity	m d ⁻¹	0.3 – 1.5	small diatom	diatom: <i>Cyclotella melosiroides</i>	Grim 1952 cited by Margalef 1961
Settling velocity	m d ⁻¹	2.5 – 3.5	small diatom	diatom: <i>Cyclotella sp.</i>	Grim 1939 cited by Margalef 1961
Si content (mean) per unit biovolume	(pmol cell ⁻¹)	533	large diatom	diatom: <i>Cyclotella bodanica</i> (currently: <i>Lindavia bodanica</i>)	Einsele and Grim 1938 cited by Conley and Kilham 1989
Si content (mean)	(pmol cell ⁻¹)	31.7	small diatom	diatom: <i>Cyclotella compta</i>	Einsele and Grim 1938 cited by Conley and Kilham 1989
Si content (mean)	(pmol cell ⁻¹)	39.8	small diatom	diatom: <i>Cyclotella compta</i>	Conley et al. unpubl. cited by Conley and Kilham 1989
Specific extinction coefficient for chlorophyll-a	m ² (mg ⁻¹ chl) ⁻¹	0.016	(marine algae)		Smith and Baker 1978 cited by Hamilton and Schladow 1997
Temperature for algal growth (maximum)	°C	35 – 40	cyanobacteria	cyanobacteria: <i>Microcystis aeruginosa</i>	Krüger and Eloff 1978
Temperature for algal growth (maximum)	°C	35	cyanobacteria	freshwater cyanobacteria: <i>Microcystis aeruginosa</i>	Gorham 1964 cited by Van der Westhuizen and Eloff 1985
Temperature for algal growth (optimum)	°C	20 – 27	flagellate	flagellate: <i>Gymnodinium splendens</i>	Thomas and Dodson, 1974
Temperature for algal growth (standard)	°C	28.8 – 30.5	cyanobacteria	cyanobacteria: <i>Microcystis aeruginosa</i>	Krüger and Eloff 1978
Temperature multiplier for algae		1.068	(freshwater algae)		Di Toro 1980
Temperature multiplier for algae		1.068			Ambrose 1988
Temperature multiplier for nitrification		1.08			Ambrose 1988

Temperature multiplier for sediments		1.03	green-algae	green-algae: <i>Scenedesmus</i> dominated	Jorgensen 1978
Uptake rate (N, maximum)	mg N (mg chl a) ⁻¹ d ⁻¹	1.5 and 3	green-algae	green-algae: <i>Scenedesmus</i> dominated	Jorgensen 1978
Uptake rate (nitrate, maximum)	mg m ⁻³	20	green-algae	green-algae: <i>Scenedesmus</i> dominated	Jorgensen 1978
Uptake rate (nitrate, maximum)	μM cells ⁻¹ h ⁻¹	0.3 – 1.6 x10 ⁻⁸	small diatom	marine diatom: <i>Cyclotella nana</i>	Lehman 1975
uptake rate (silicate, maximum)	d ⁻¹	2.3	large diatom	marine diatom: <i>Hantzschia</i> sp.	Taguchi et al. 1987
uptake rate (silicate, maximum)	d ⁻¹	9.3	small diatom	marine diatom: <i>Cyclotella</i> sp.	Taguchi et al. 1987

References

Author	Year	Title	Publisher
Margalef, R.	1961	Velocidad de sedimentación de organismos pasivos de fitoplancton (Sinking speed of pasive phytoplanktonic organisms)	Invest. Pesq. 18: 3-8 (Investigación Pesquera 18: 3-8)
Mullin, M. M., Sloan, P. R. & Eppley, R. W.	1966	Relationship between carbon content, cell volume and area in phytoplankton.	Limnol. Oceanogr. 11:307–11.
Strathmann, R. R.	1967	Estimating the organic content of phytoplankton from cell volume or plasma volume.	Limnol. Oceanogr. 12:411–8.
Carpenter, E.J. and R.R.L. Guillard	1971	Intraspecific differences in nitrate half-saturation constants for three species of marine phytoplankton.	Ecology 52 : 183-185.
Eppley, R.W., A. F. Carlucci, O. Holm-Hansen, D. Kiefer, J. J. McCarthy, Elizabeth Venrick, P. M. Williams	1971	Phytoplankton growth and composition in shipboard cultures supplied with nitrate, ammonium or urea as the nitrogen source	Limnol Oceanogr 16(5): 741-757
Andersen, J. M.	1974	Nitrogen and phosphorus budgets and the role of sediments in six shallow Danish lakes.	Arch. Hydro- biol., 74: 528-550.
Bannister, T.T.,	1974	Production equations in terms of chlorophyll concentration, quantum yield and upper limit to production.	Limnol. Oceanogr., 19: 1-12
Halmann, M. and M. Stiller	1974	Turnover and uptake of dissolved phosphate in freshwater	Limnol Oceanogr 19(5): 774-783
Imboden, D.M.	1974	Phosphorus model of lake eutrophication	Limnol Oceanogr 19(2):297-304
Smayda, T.J.	1974	Some experiments on the sinking characteristics of two freshwater diatoms	Limnol Oceanogr. 10:628-635
Thomas, W.H. and A.N. Dodson	1974	Effect of interactions between temperature and nitrate supply on the cell-division rates of two marine phytoflagellates	Mar. Biol. 24: 213-217
Lehman, T.D., Botkin, D.B. and Likens, G.E.	1975	The assumptions and rationales of a computer model of phytoplankton population dynamics.	Limnol. Oceanogr., 20: 343-364
Lehman, T.D.,	1976	Ecological and nutritional studies on Dinobryon Ehrenb.: Seasonal periodicity and the phosphate toxicity problem	Limnol Oceanogr 21(5): 646
Reynolds, C.S.	1976	Sinking movements of phytoplankton indicated by a simple trapping method. I.A Fragilaria population.	Br. Phycol. J. 11: 279-291
Titman, D. and P. Kilham	1976	Sinking in freshwater phytoplankton: Some ecological implications of cell nutrient status and physical mixing processes	Limnol Oceanogr 21(3): 409-417
Jorgensen, S.E., Mejer, H.F. and Friis, M.	1978	Examination of a lake model.	Ecol. Modelling, 4: 253-279.
Smith, R.C. and Baker, K.S.	1978	The bio-optical state of ocean waters and remote sensing	Limnol. Oceanogr., 23: 247-259
Jørgensen, S.E.	1979	Handbook of Environmental Data and Ecological Parameters	ed. Oxford : Pergamon, 1162pp.

Smith, V.H.	1979	Nutrient dependence of primary productivity in lakes.	Limnol. Oceanogr., 24: 1051-1064
Burns, N. M., and Rosa, F.	1980	In situ measurements of the settling velocity of organic carbon particles and 10 species of phytoplankton.	Limnol. Oceanogr.25:855-864.
Holm, N.P., Armstrong, D.E.	1981	Role of nutrient limitation and competition in controlling the populations of <i>Asterionella formosa</i> and <i>Microcystis aeruginosa</i> in semicontinuous culture.	Limnol. Oceanogr. 26, 622–634
Infante, A. and A. H. Litt	1985	Differences between two species of <i>Daphnia</i> in the use of 10 species of algae in Lake Washington.	Limnol. Oceanogr. 30: 1053–1059.
Rocha, O. and Duncan, A.	1985	The relationship between cell carbon and cell volume in freshwater algal species used in zooplankton studies.	J. Plankton Res. 7:279–94
Ambrose, Jr., R.B., Wool, T.A., Connolly J.P. and Schanz, R.W.,	1988	WASP4, a hydrodynamic and water quality model - model theory, user's manual, and programmer's guide	U.S. EPA Report EPA/600/3-87/039, 297 pp.
Verity, P. G., Robertson, C. Y., Tronzo, C. R., Andrews, M. G., Nelson, J. R. & Sieracki, M. E.	1992	Relationships between cell volume and the carbon and nitrogen content of marine photosynthetic nanoplankton.	Limnol. Oceanogr. 37:1434–46.
Montagnes, D. J. S., Berges, J. A., Harrison, P. J. & Taylor, F. J.R.	1994	Estimating carbon, nitrogen, protein, and chlorophyll a from volume in marine phytoplankton	Limnol. Oceanogr. 39:1044–60.
Hamilton, D. P. and S. G. Schladow	1997	Prediction of water quality in lakes and reservoirs. Part I – Model description	Ecological Modelling 96 (1997) 91-110
Schladow, S. G. and D. P. Hamilton	1997	Prediction of water quality in lakes and reservoirs. Part II - Model calibration, sensitivity analysis and application	Ecological Modelling Volume 96, Issues 1–3, 1 March 1997, Pages 111-123
Robson, B. J. and D. P. Hamilton	2004	Three-dimensional modelling of a <i>Microcystis</i> bloom event in the Swan River estuary, Western Australia	Ecol. Model. 174 (1–2), 203–222.
Bruce, L.C., David Hamilton, Jörg Imberger, Gideon Gal, Moshe Gophen, Tamar Zohary, K. David Hambright	2006	A numerical simulation of the role of zooplankton in C, N and P cycling in Lake Kinneret, Israel	Ecological Modelling Volume 193, Issues 3–4, 15 March 2006, Pages 412-436
Bruce, L. C., Robert Jellison, Jörg Imberger and John M Melack	2008	Effect of benthic boundary layer transport on the productivity of Mono Lake, California	Saline Systems volume 4, Article number: 11 (2008)
Burger, David F., David P. Hamilton and Conrad A. Pilditch	2008	Modelling the relative importance of internal and external nutrient loads on water column nutrient concentrations and phytoplankton biomass in a shallow polymictic lake	Ecological Modelling Volume 211, Issues 3–4, 10 March 2008, Pages 411-423
Trolle, D., H. Skovgaard and Erik Jeppesen	2008	The Water Framework Directive: Setting the phosphorus loading target for a deep lake in Denmark using the 1D lake ecosystem model DYRESM–CAEDYM	Ecological Modelling Volume 219, Issues 1–2, 24 November 2008, Pages 138-152
Trolle, D., Torben B. Jørgensen and Erik Jeppesen	2008	Predicting the effects of reduced external nitrogen loading on the nitrogen dynamics and ecological state of deep Lake Ravn, Denmark, using the DYRESM–CAEDYM model	Limnologia 38 (2008) 220–232
Gal G., Hipsey M.R., Parparov A., Wagner U., Makler V. & Zohary T.	2009	Implementation of ecological modeling as an effective management and investigation tool: Lake Kinneret as a case study.	Ecological Modelling, 220, 1697–1718.
Zohary, T.	2004	Changes to the phytoplankton assemblage of Lake Kinneret after decades of a predictable, repetitive pattern	Freshwater Biology (2004) 49, 1355–1371
Schlabing, D., M.A. Frassl, M.M. Eder a, K. Rinke and A. Bardossy	2014	Use of a weather generator for simulating climate change effects on ecosystems: A case study on Lake Constance	Environmental Modelling & Software Volume 61, November 2014, Pages 326-338
Hanson, P.C., David P. Hamilton, Emily H. Stanley, Nicholas Preston, Owen C. Langman, Emily L. Kara	2011	Fate of Allochthonous Dissolved Organic Carbon in Lakes: A Quantitative Approach	PLoS ONE 6(7): e21884. https://doi.org/10.1371/journal.pone.0021884
Hipsey, Matthew R., Ryan Alexander & Chris J. Dallimore	2007	Simulation Model to Evaluate Coeur d’Alene Lake’s Response to Watershed Remediation. Volume 2: Water quality modeling using ELCOM-CAEDYM	

11. Appendix B: One-dimensional Model Results

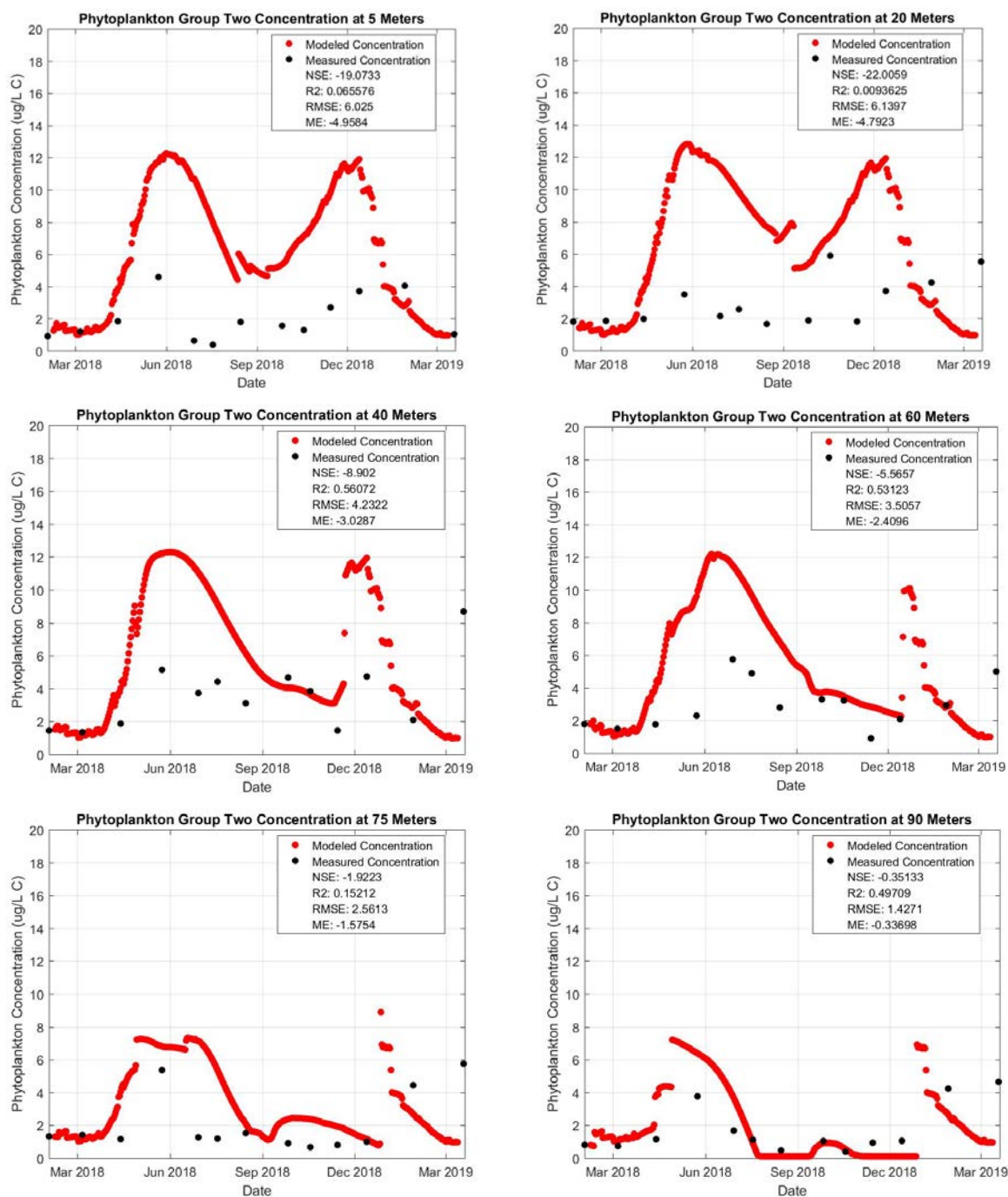


Figure 11-1. Comparison of sampled and model simulated phytoplankton concentration for phytoplankton group two at constant depths from the surface of Lake Tahoe.

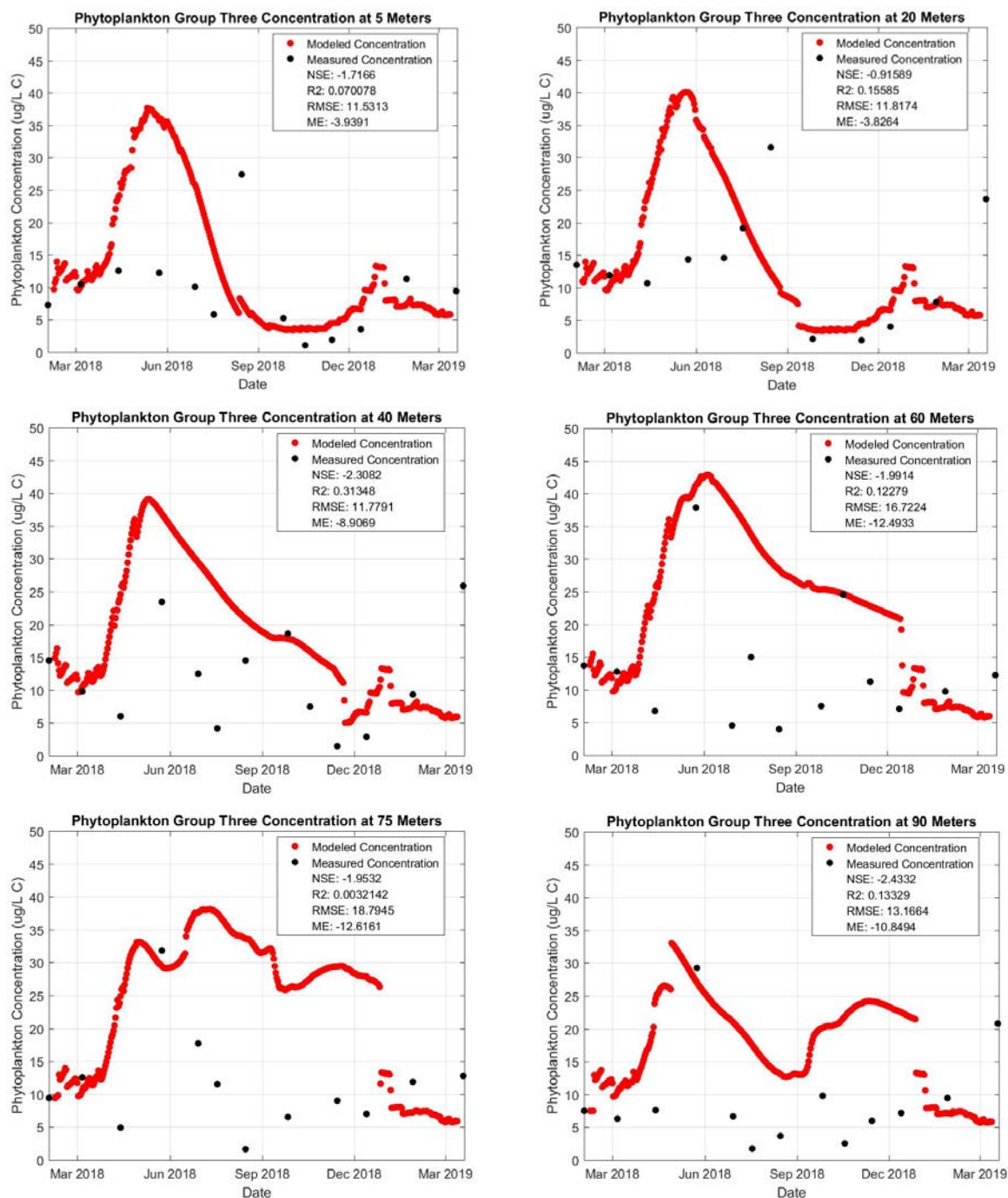


Figure 11-2. Comparison of sampled and model simulated phytoplankton concentration for phytoplankton group three at constant depths from the surface of Lake Tahoe.

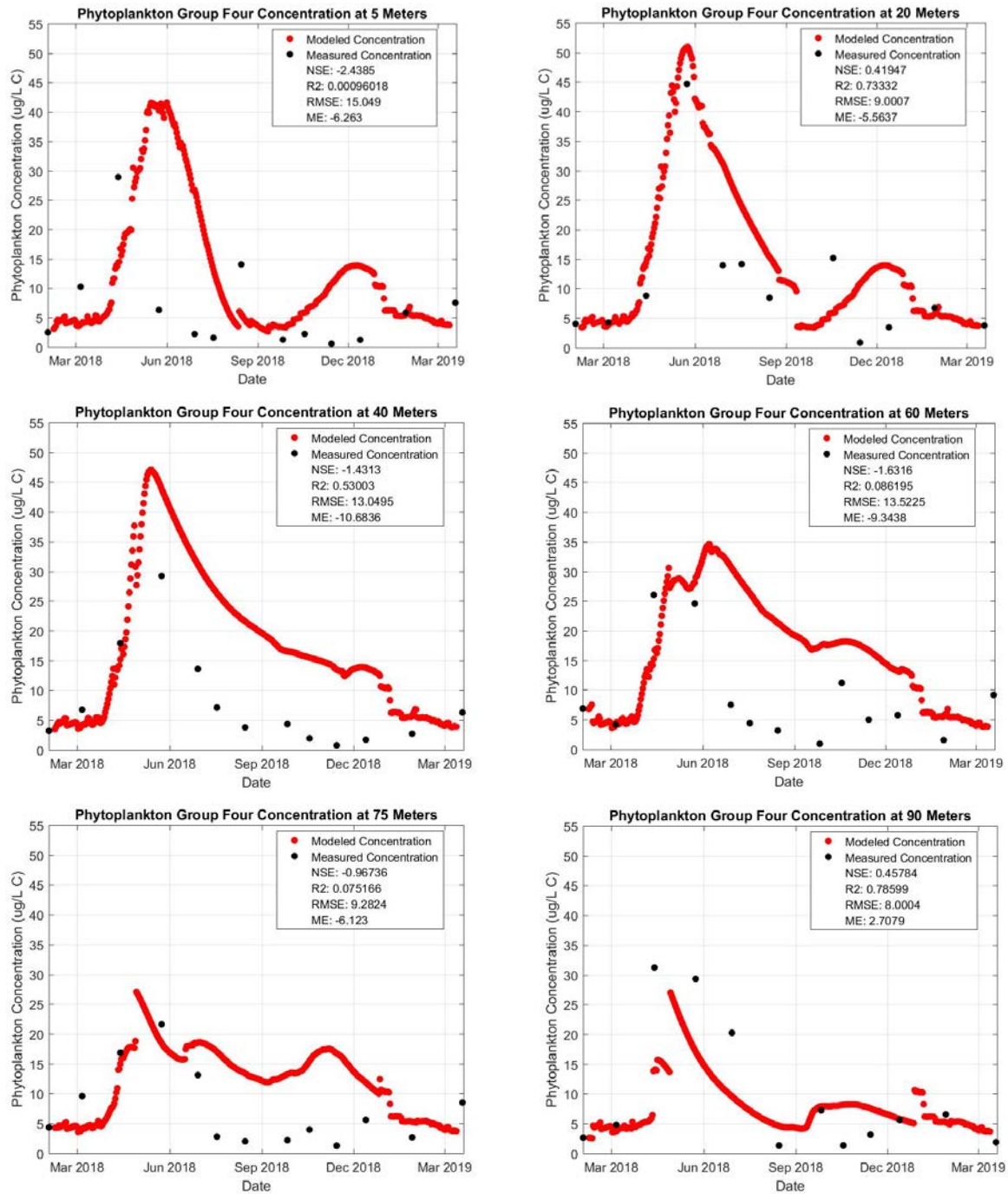


Figure 11-3. Comparison of sampled and model simulated phytoplankton concentration for phytoplankton group four at constant depths from the surface of Lake Tahoe.

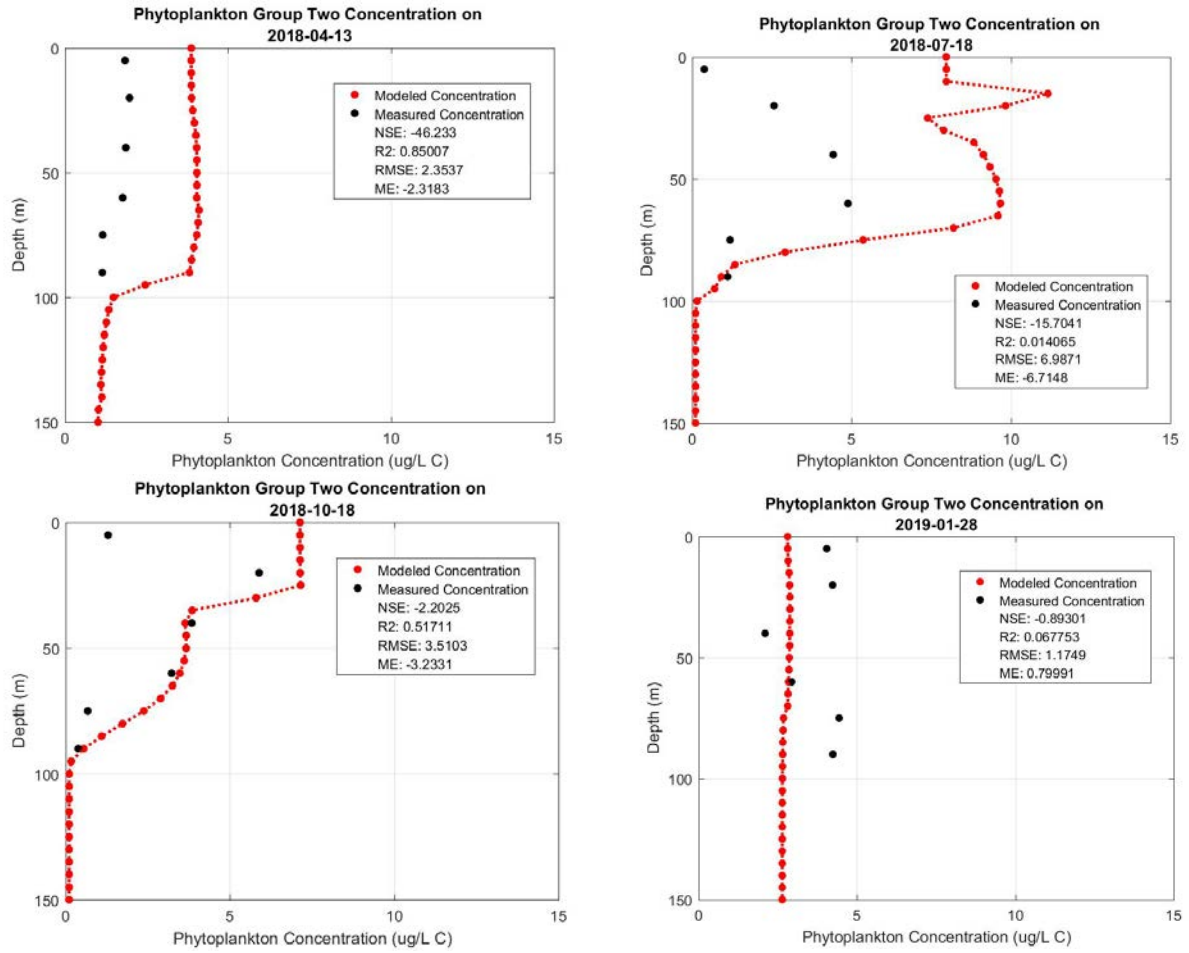


Figure 11-4. Quarterly vertical profiles of sampled and model simulated phytoplankton concentration for phytoplankton group two.

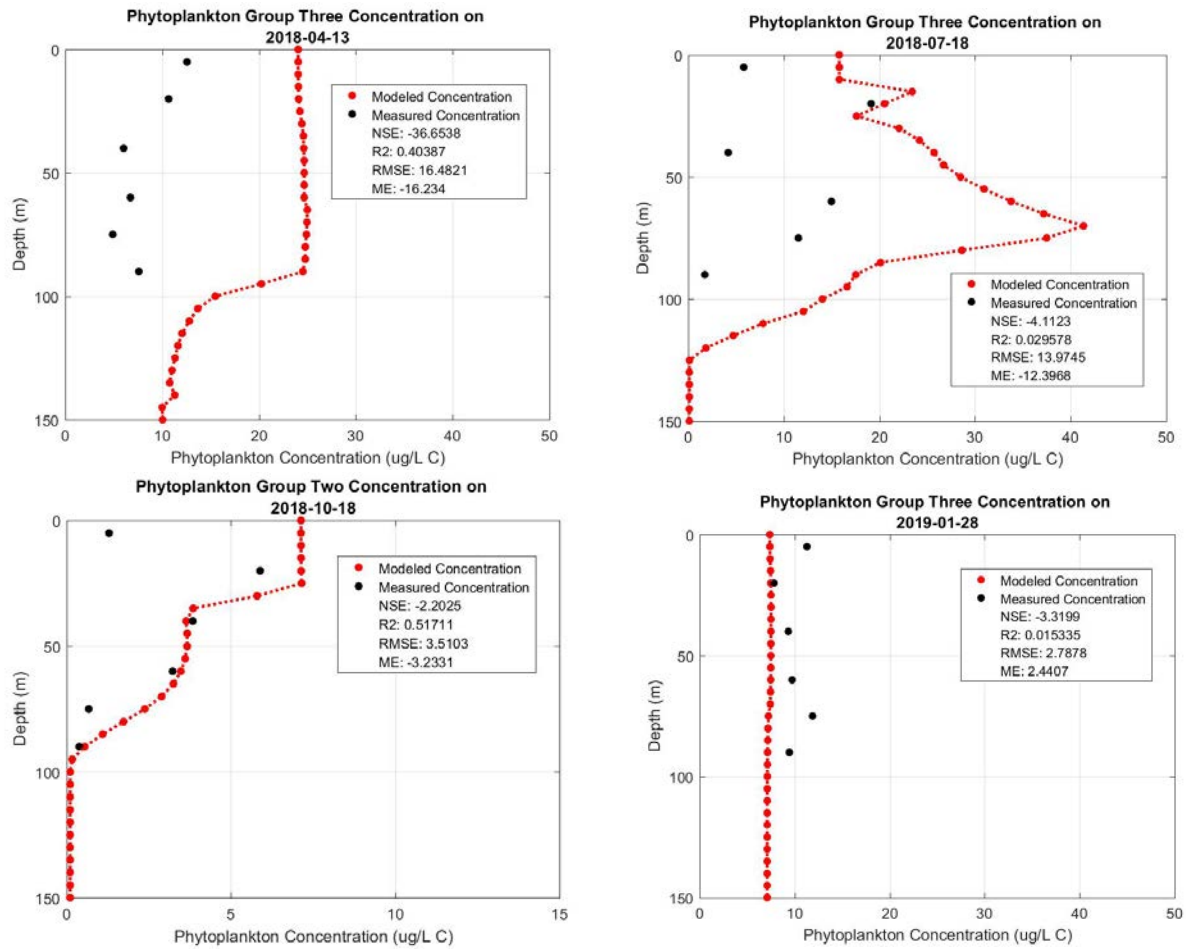


Figure 11-5. Quarterly vertical profiles of sampled and model simulated phytoplankton concentration for phytoplankton group four.

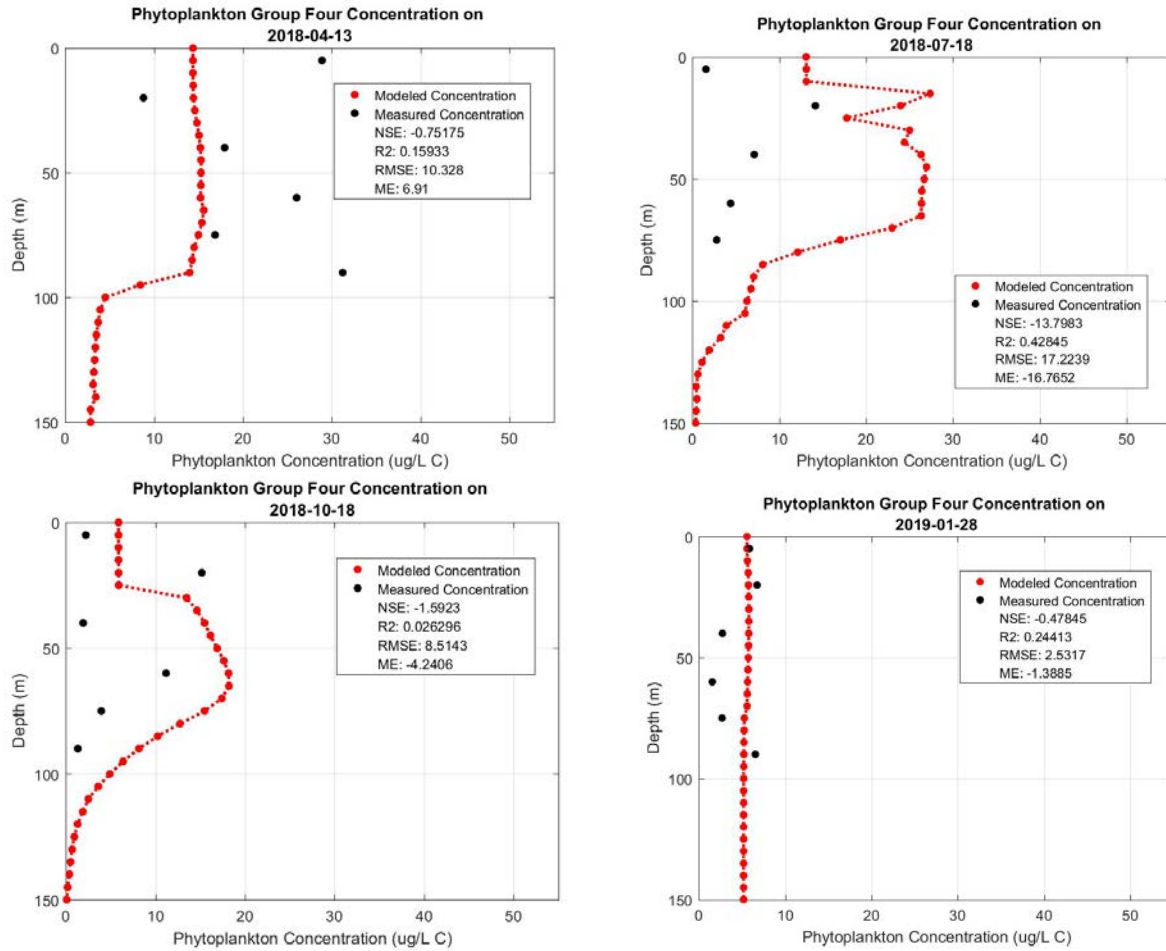


Figure 11-6. Quarterly vertical profiles of sampled and model simulated phytoplankton concentration for phytoplankton group four.

Table 11-1. List of phytoplankton model variables whose sensitivity was assessed, with their magnitude of change applied and resulting change in modeled phytoplankton concentration for the phytoplankton group which variable was modified. Gray areas indicate > 10% of change

<i>Variable Changed</i>	<i>Magnitude of Change</i>	<i>Change in Plankton Group Two</i>	<i>Change in Plankton Group Three</i>	<i>Change in Plankton Group Four</i>
Optimal Temperature	-1 Degree	4%	-4%	-2%
	+1 Degree	-11%	-3%	-8%
Temperature Boundary Distance	-1 Degree	3%	4%	9%
	+1 Degree	-3%	-4%	-8%
Zooplankton Grazing	-10%	-75%	0%	1%
	+10%	-75%	0%	1%
Maximum Growth Rate	-10%	-64%	-17%	-31%
	+10%	40%	15%	41%
Maximum Mortality Rate	-10%	6%	13%	53%
	+10%	-7%	-11%	-35%
Light Saturation	-10%	-11%	-4%	-7%
	+10%	7%	4%	7%
Phosphorus to Carbon Mass Ratio	-10%	0%	2%	-1%
	+10%	0%	-2%	1%
Nitrogen to Carbon Mass Ratio	-10%	2%	2%	3%
	+10%	-2%	-2%	-3%
Settling Velocity for Phytoplankton	-10%	0%	0%	0%
	+10%	0%	0%	0%
Nitrogen Half Saturation Constant	-10%	11%	4%	14%
	+10%	-12%	-4%	-11%
Phosphorus Half Saturation Constant	-10%	14%	7%	4%
	+10%	-16%	-7%	-4%
Ammonia Half Saturation Constant	-10%	0%	0%	0%
	+10%	0%	0%	0%

Table 11-2. List of phytoplankton model for phytoplankton group two whose sensitivity was assessed, with their magnitude of change applied and resulting change in model performance for all calibrated phytoplankton groups that occurred as a result.

Phytoplankton Group Two				
Variable Changed	Magnitude of Change	Change in Plankton Group Two	Change in Plankton Group Three	Change in Plankton Group Four
Optimal Temperature	-1 Degree	4%	0%	-1%
	+1 Degree	-11%	1%	1%
Temperature Boundary Distance	-1 Degree	3%	0%	0%
	+1 Degree	-3%	0%	0%
Zooplankton Grazing	-10%	-75%	4%	86%
	+10%	-75%	4%	86%
Maximum Growth Rate	-10%	-64%	6%	10%
	+10%	40%	-8%	-12%
Maximum Mortality Rate	-10%	6%	-1%	-1%
	+10%	-7%	1%	1%
Light Saturation	-10%	-11%	1%	2%
	+10%	7%	-1%	-2%
Phosphorus to Carbon Mass Ratio	-10%	0%	0%	0%
	+10%	0%	0%	0%
Nitrogen to Carbon Mass Ratio	-10%	2%	0%	1%
	+10%	-2%	0%	-1%
Settling Velocity for Phytoplankton	-10%	0%	0%	0%
	+10%	0%	0%	0%
Nitrogen Half Saturation Constant	-10%	11%	-2%	-3%
	+10%	-12%	2%	2%
Phosphorus Half Saturation Constant	-10%	14%	-1%	-2%
	+10%	-16%	1%	2%
Ammonia Half Saturation Constant	-10%	0%	0%	0%
	+10%	0%	0%	0%

Table 11-3. List of phytoplankton model for phytoplankton group three whose sensitivity was assessed, with their magnitude of change applied and resulting change in model performance for all calibrated phytoplankton groups that occurred as a result.

Phytoplankton Group Three				
Variable Changed	Magnitude of Change	Change in Plankton Group Two	Change in Plankton Group Three	Change in Plankton Group Four
Optimal Temperature	-1 Degree	4%	-4%	3%
	1 Degree	3%	-3%	1%
Temperature Boundary Distance	-1 Degree	-4%	4%	-1%
	1 Degree	4%	-4%	1%
Zooplankton Grazing	-10%	-6%	0%	1%
	10%	-6%	0%	1%
Maximum Growth Rate	-10%	28%	-17%	15%
	10%	-42%	15%	-14%
Maximum Mortality Rate	-10%	-11%	13%	-3%
	10%	9%	-11%	3%
Light Saturation	-10%	6%	-4%	1%
	10%	-6%	4%	-1%
Phosphorus to Carbon Mass Ratio	-10%	0%	2%	-1%
	10%	0%	-2%	1%
Nitrogen to Carbon Mass Ratio	-10%	6%	2%	7%
	10%	-7%	-2%	-6%
Settling Velocity for Phytoplankton	-10%	0%	0%	0%
	10%	0%	0%	0%
Nitrogen Half Saturation Constant	-10%	-7%	4%	-3%
	10%	6%	-4%	2%
Phosphorus Half Saturation Constant	-10%	-15%	7%	-7%
	10%	12%	-7%	7%
Ammonia Half Saturation Constant	-10%	0%	0%	0%
	10%	0%	0%	0%

Table 11-4. List of phytoplankton model for phytoplankton group four whose sensitivity was assessed, with their magnitude of change applied and resulting change in model performance for all calibrated phytoplankton groups that occurred as a result.

Phytoplankton Group Four				
Variable Changed	Magnitude of Change	Change in Plankton Group Two	Change in Plankton Group Three	Change in Plankton Group Four
Optimal Temperature	-1 Degree	4%	1%	-2%
	1 Degree	-1%	-1%	-8%
Temperature Boundary Distance	-1 Degree	-2%	0%	9%
	1 Degree	2%	0%	-8%
Zooplankton Grazing	-10%	-6%	0%	1%
	10%	-6%	0%	1%
Maximum Growth Rate	-10%	15%	4%	-31%
	10%	-25%	-6%	41%
Maximum Mortality Rate	-10%	-12%	-3%	53%
	10%	8%	2%	-35%
Light Saturation	-10%	2%	0%	-7%
	10%	-2%	0%	7%
Phosphorus to Carbon Mass Ratio	-10%	0%	1%	-1%
	10%	0%	-1%	1%
Nitrogen to Carbon Mass Ratio	-10%	4%	0%	3%
	10%	-4%	0%	-3%
Settling Velocity for Phytoplankton	-10%	0%	0%	0%
	10%	0%	0%	0%
Nitrogen Half Saturation Constant	-10%	-4%	-1%	14%
	10%	3%	1%	-11%
Phosphorus Half Saturation Constant	-10%	-4%	-1%	4%
	10%	3%	1%	-4%
Ammonia Half Saturation Constant	-10%	0%	0%	0%
	10%	0%	0%	0%

12. Appendix C: Three-dimensional Hydrodynamic Model Validation Scenarios

12.1. Validation of Summer 2018

The model for the summer season was set to predict the lake hydrodynamics between June 19th and August 02nd (43 days). The calibrated parameters from Spring 2018 are used for this period and the remaining validations in this report (e.g., C_{db} , C_{dw} , C). During the simulation period we observed better performance on the prediction of the temperature structure when applying multiplying factors of 0.9 for the wind speed, and 1.1 for the incoming shortwave and incoming longwave radiation parameters. The modified forcing conditions applied to the numerical model are shown in Figure 12-1, and provide an improvement of approximately 20% in comparison to simply considering the conditions applied to the Spring 2018 season (i.e., 0.9 for wind speed and 1.1 for incoming shortwave).

We focused on the PSi3D performance to represent the warming of the epilimnion and strengthening of the stratification during the increasing summer temperatures and longer days. The proper prediction of lake hydrodynamics during Summer is relevant to the ecology as the surface warming and increase of the temperature gradient in the water column impedes vertical fluxes of nutrients and chlorophyll, and limits the Mysis diurnal vertical migration due to their temperature tolerance ($\approx 18^\circ\text{C}$). In Figure 12-2 to Figure 12-4, we present the comparison of the field observations and numerical results, where good agreement in the overall dynamics is observed.

Increasing temperature gradient in the temperature vertical profiles from the numerical results closely follow the field observations (See Figure 12-3). Nonetheless a slight overprediction of 1.5°C in the top 20 meters at the end of the study period was observed. Surface temperature records show that overprediction of the surface temperature occurs in the last 10 days of the simulated period (Figure 12-4).

The performance metrics indicate that the numerical results fall within the excellent and very good categories for the SS, and RMSE estimates are below 1°C for most of the sites (Table 12-1). The maximum error occurs at shallow sites HW, TC, and RB with $RMSE > 1$, values of the same order of magnitude to similar 3D hydrodynamics models (Rueda et al., 2003). The numerical error (RMSE) obtained is in overall less than 10% of the temperature fluctuation (10°C), and thus we conclude that the numerical model properly predicts the surface warming and increase of the temperature gradient in the water column.

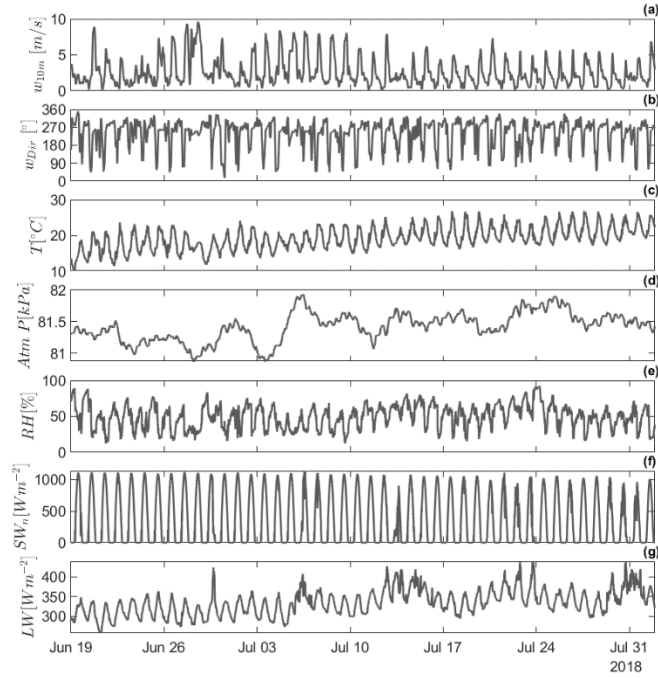


Figure 12-1. Numerical model surface boundary condition parameters from observed meteorological conditions for Summer 2018. Time series of wind speed modified by 0.9 (a), incoming shortwave multiplied by 1.1, and incoming longwave radiation multiplied by 1.1 (g). Time series plot of (a) wind speed, (b) wind direction, (c) air temperature, (d) atmospheric pressure, (e) relative humidity, (f) net shortwave radiation, and (g) incoming longwave.

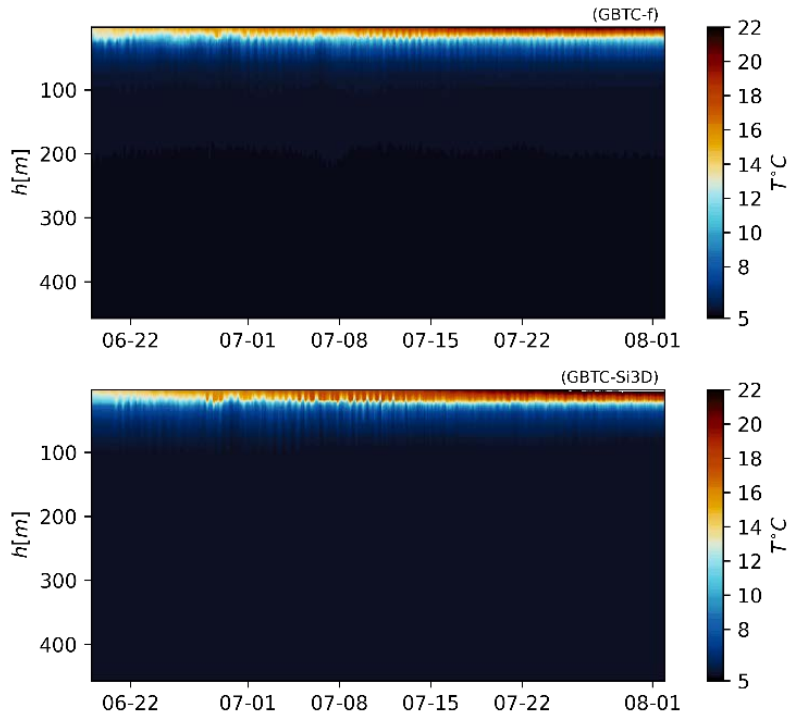


Figure 12-2. Validation of the numerical results regarding temperature; tile names indicate the site location from Figure 7-1. Time series color plot are named by site followed by -f and -Si3D for field and PSi3D results, respectively. The surface color plot shows the evolution of the temperature structure in time and depth.

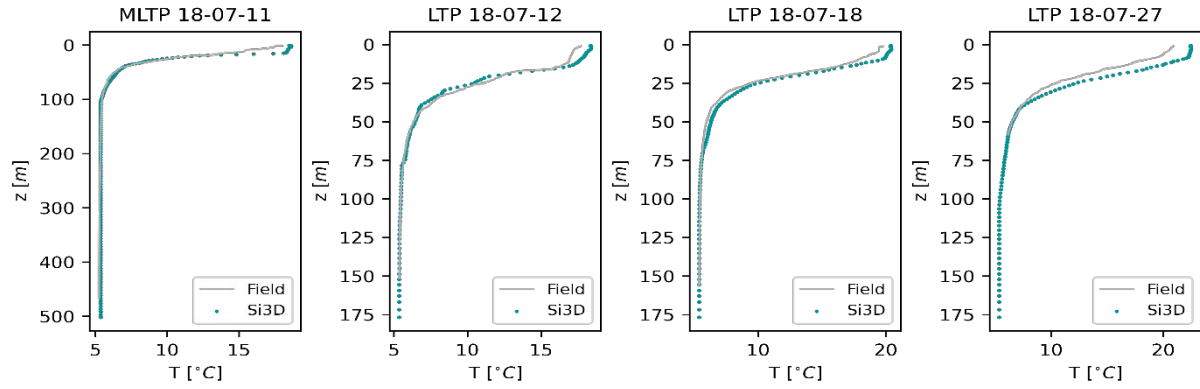


Figure 12-3. Validation of CTD profiles collected at LTP and MLTP. The title of individual plots indicates the site and date of the temperature profile. Snapshots show the vertical temperature structure of the PSi3D results (green dots) and the data collected on site (gray line).

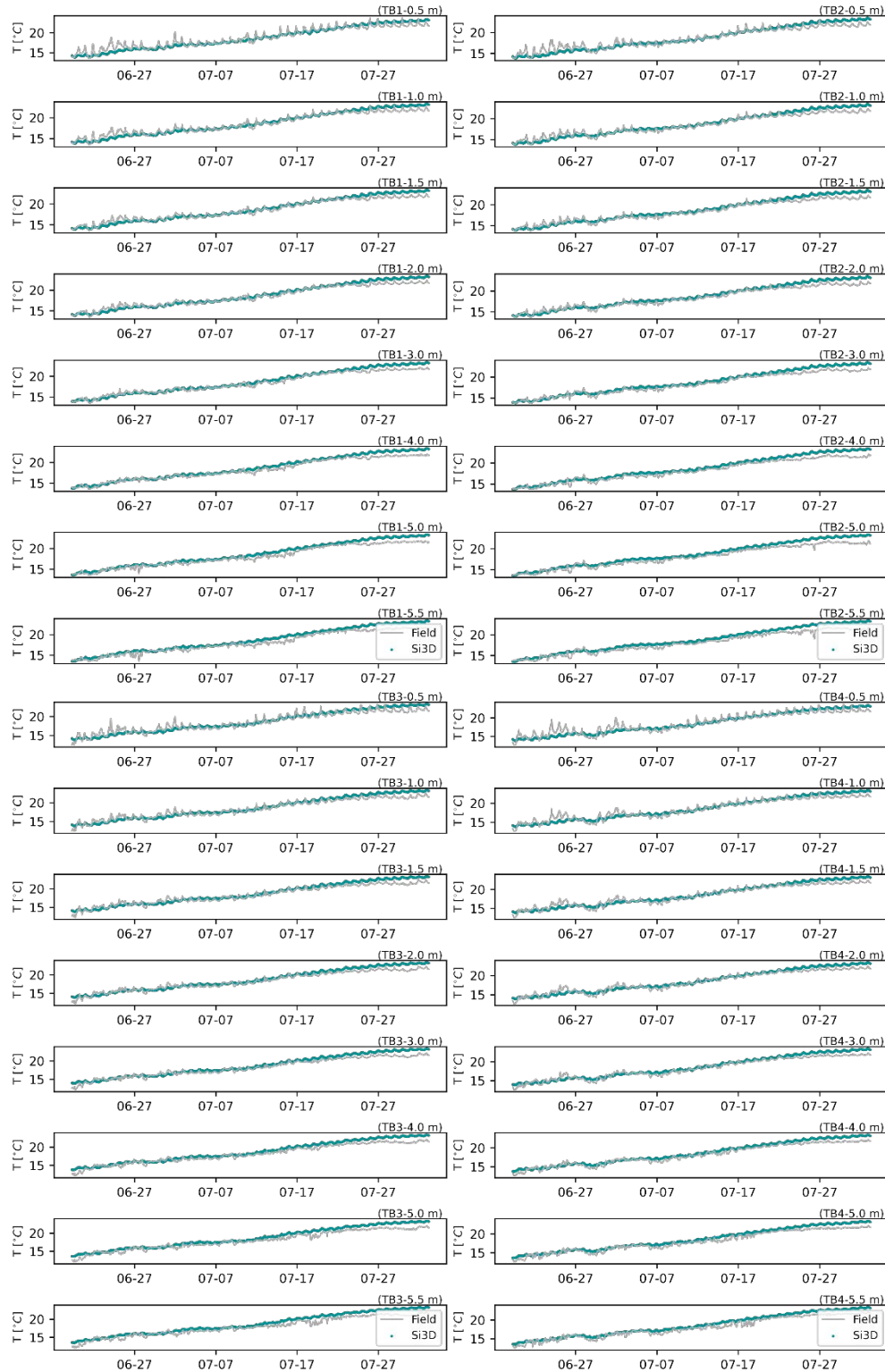


Figure 12-4. Temperature validation of the numerical results (green dots) and field records (gray line). Tile names indicate the site location from Figure 7-1 with the site followed by the depth of the measurement.

Table 12-1. Statistical metric estimations for model performance validation Summer 2018.

Site	SS	I_1	I_2	RMSE (°C)
Temperature				
CR	0.83	0.05	0.05	0.95
DP	0.89	0.04	0.05	0.84
GBTC	0.96	0.05	0.09	0.73
HW	0.57	0.09	0.10	1.72
LTP	0.95	0.05	0.08	0.78
MLTP	0.95	0.03	0.08	0.49
RB	0.55	0.07	0.07	1.36
SH	0.87	0.04	0.05	0.87
TB1	0.92	0.03	0.04	0.72
TB2	0.89	0.04	0.04	0.79
TB3	0.88	0.04	0.05	0.86
TB4	0.91	0.04	0.04	0.78
TC	0.84	0.05	0.06	1.04
TV	0.87	0.04	0.05	0.91

12.2. Validation of Fall 2018

During the Fall season we focused at validating the model performance to predict the annual weakening of the stratification and deepening of the thermocline. The erosion of the stratification during Fall alters the water clarity as thermocline deepens and reaches the depth of maximum chlorophyll concentration; making it available for convective processes to bring it up to the euphotic zone. Furthermore, in late Fall, as the thermocline and nitracline depths align, diapycnal mixing during severe winds may be a source of nutrient loading to the photic zone. To corroborate the performance of the model at representing the hydrodynamics, we ran the lake model from September 19th to December 16th. After a sensitivity analysis, we observed that the model performance improved when multiplying the wind speed by 0.9, and the incoming longwave radiation by a factor of 1.1. The surface boundary conditions applied to the model are shown in Figure 12-5.

Temperature evolution in time and depth on the east shore (GBTC) is shown in Figure 12-6, where correct timing of the water column cooling can be observed. Good agreement on the water column temperature changes of $\approx 5^\circ\text{C}$ to $\approx 18^\circ\text{C}$ during mid-September and $\approx 5^\circ\text{C}$ to $\approx 10^\circ\text{C}$ at the end of the study period provide confidence on the model's performance during the Fall season. Furthermore, internal wave motions, identified as the oscillations of the temperature contours, decreased as the stratification weakened at the end of October and during November and are accurately represented by the numerical model (Figure 12-6). The good agreement on the internal wave dynamics allows us to conclude the good estimation of the velocity field in the lake by the numerical model.

Moreover, vertical profiles at LTP (Figure 12-7) indicate that predicted deepening of the thermocline and sharpening of the vertical temperature structure follows closely the field observations, including the sharp temperature gradient in late Fall (i.e., December). The statistical performance metrics on the LTP and

MLTP show excellent agreement ($SS \approx 1$) and $RMSE < 0.6^\circ C$, supporting the very good agreement observed in the figures. Finally, overall surface temperature cooling is properly represented by the numerical model (Figure 12-8). However, diurnal temperature fluctuations are smaller than recorded in the field, similar to model results observed in previous sections, and due to the limitations on the discretization of the vertical domain.

The performance metrics indicate that the numerical results fall are within the excellent category at all sites and on average $\overline{SS} \approx 0.96$ and $\overline{RMSE} \approx 0.5^\circ C$ for the whole lake. The numerical error (RMSE) is $\approx 6\%$ of the temperature range during the simulation, supporting the outstanding agreement of the model results and the field observations ().

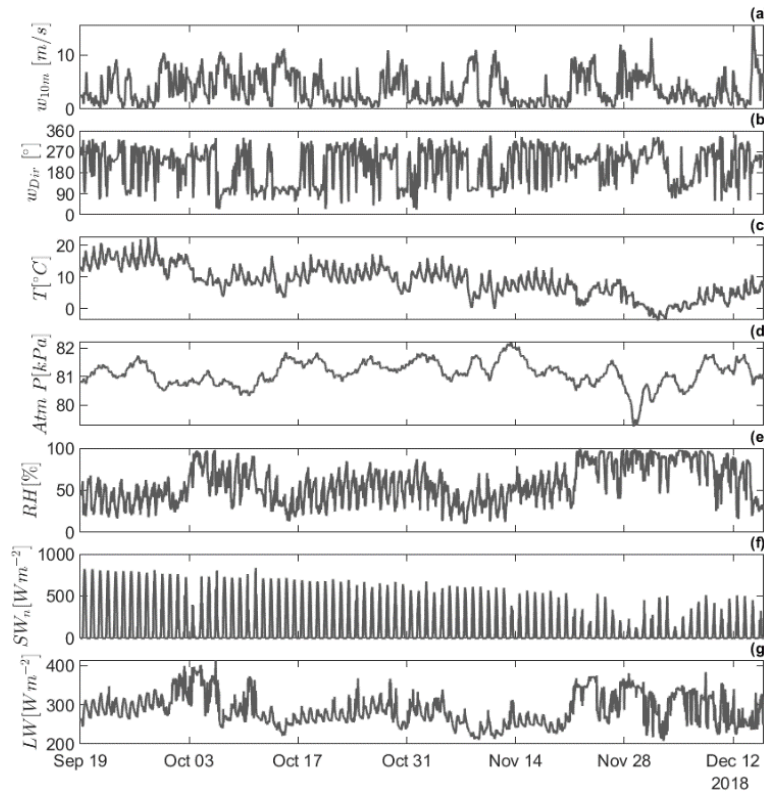


Figure 12-5. Numerical model surface boundary condition parameters from observed meteorological conditions for Fall 2018. Wind speed modified by a factor of 0.9 (a) and incoming longwave radiation multiplied by 1.1 (g). Time series plot of (a) wind speed, (b) wind direction, (c) air temperature, (d) atmospheric pressure, (e) relative humidity, (f) net shortwave radiation, and (g) incoming longwave.

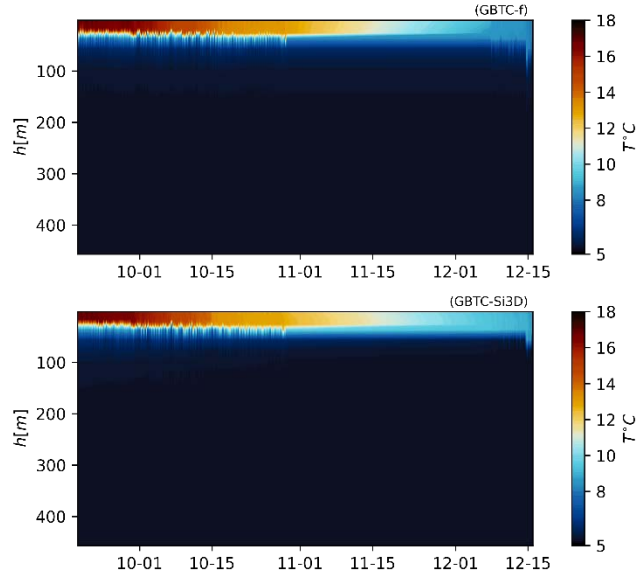


Figure 12-6. Validation of the numerical results regarding temperature; tile names indicate the site location from Figure 7-1. Time series color plot are named by site followed by -f and -Si3D for field and PSi3D results, respectively. The surface color plot shows the evolution of the temperature structure in time and depth.

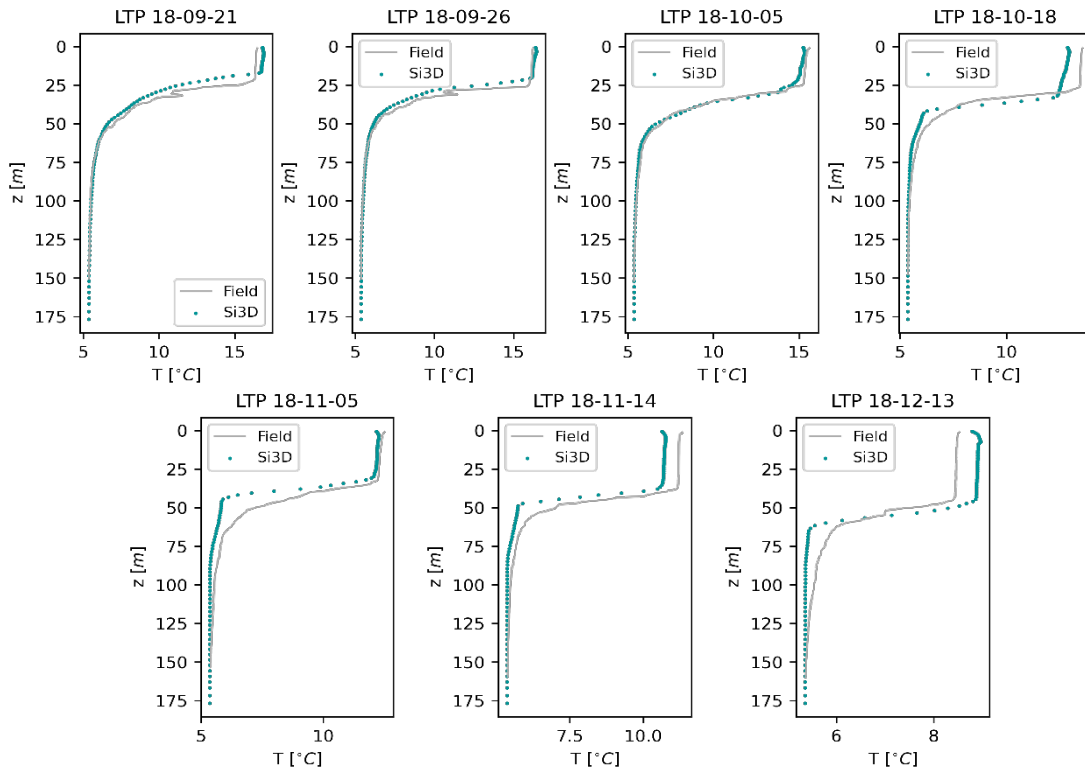


Figure 12-7. Validation of CTD profiles collected at LTP. The title of individual plots indicates the site and date of the temperature profile. Snapshots show the vertical temperature structure of the PSi3D results (green dots) and the data collected on site (gray line).

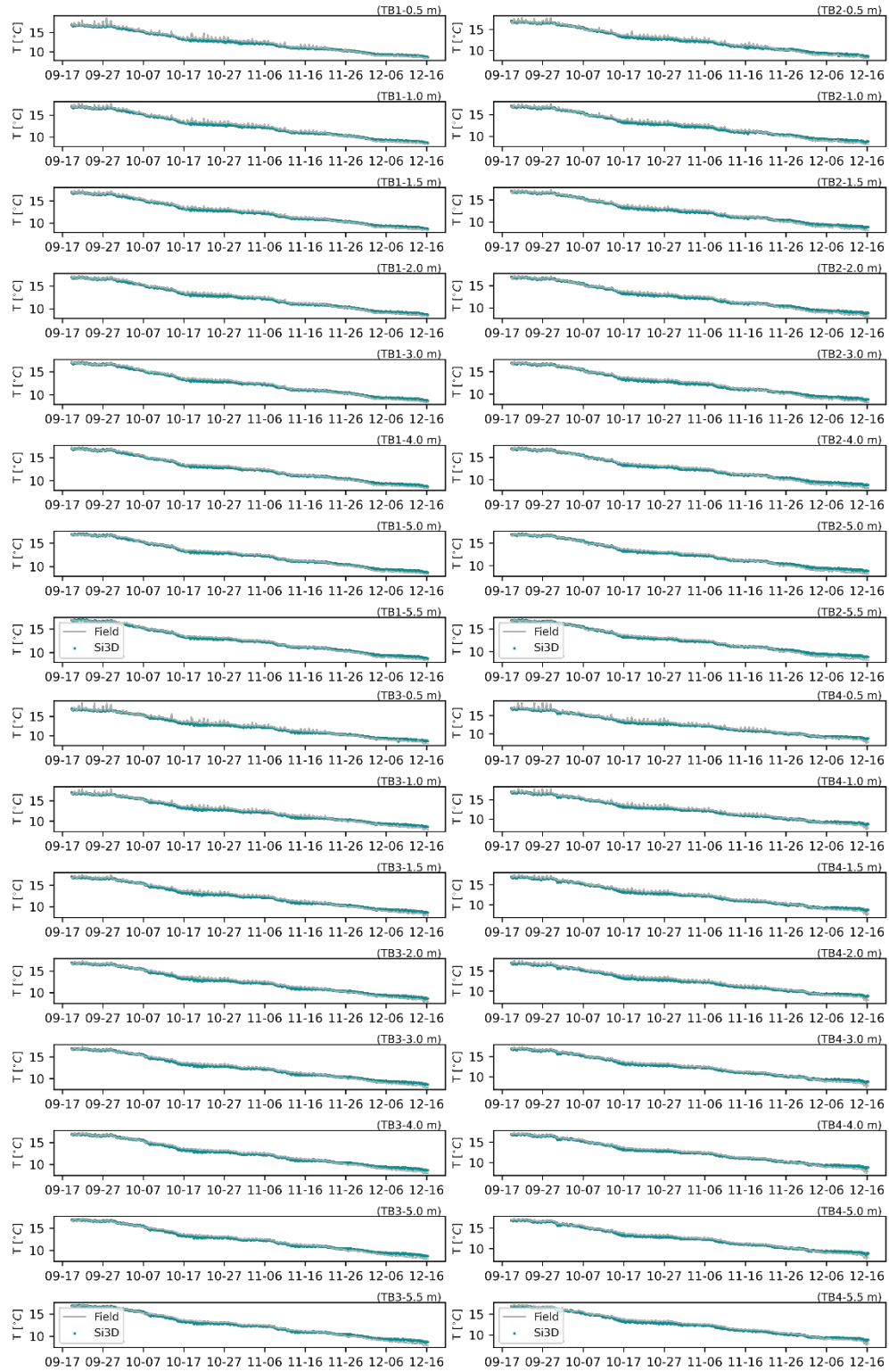


Figure 12-8. Temperature validation of the numerical results (green dots) and field records (gray line). Tile names indicate the site location from Figure 7-1 with the site followed by the depth of the measurement.

Table 12-2. Statistical metric estimations for model performance validation Fall 2018.

Site	SS	I_1	I_2	RMSE (°C)
DP	0.959	0.033	0.044	0.562
RB	0.953	0.040	0.049	0.611
SH	0.959	0.037	0.045	0.571
TC	0.917	0.059	0.076	0.921
TV	0.968	0.031	0.039	0.495
LTP	0.959	0.041	0.068	0.552
MLTP	0.955	0.017	0.048	0.302
TB1	0.989	0.018	0.021	0.273
TB2	0.985	0.021	0.025	0.320
TB3	0.985	0.021	0.025	0.326
TB4	0.984	0.022	0.026	0.331
GBTC	0.982	0.029	0.057	0.345
MK	0.948	0.044	0.052	0.653
GB	0.932	0.052	0.062	0.759

12.3. Validation of Spring 2011

The information presented in sections 7.1.6, 12.1, and 12.2 supports the capacity of the PSi3D model to properly represent the overall annual lake hydrodynamics. Nonetheless, we include the validation for the 2011 year to corroborate the lake physics and thus supporting the findings in the Ecology section of the numerical model. In this section, we present the comparison of the field and numerical data for the Spring season.

The Spring 2011 period considered the prediction of the temperature and velocity fields for April 12 to June 22, 2011 (70 days). Like the 2018 Spring season, we focused on the numerical model performance to predict the onset of the stratification and initial annual surface warming (Section 7.1.6).

During the study period, the USCG meteorological station (Figure 7-1) was down, and thus, records for the parameters used from this site, as explained in section 7.1.4, are not available to generate the forcing conditions for the numerical model. To overcome the lack of shortwave records, we used available Photosynthetically Active Radiation (PAR) data. The PAR data was then used to estimate incoming shortwave radiation following Britton & Dodd, (1976), where the shortwave irradiance is defined as the downward irradiance for PAR (400 – 700 ηm) modified by an empirical constant (Equation (12-1). Britton & Dodd, (1976) found this constant to be on average 0.47.

$$SWin_{Mod} = C_{SW}PAR, \quad (12-1)$$

Comparison of the available shortwave measurements and modeled shortwave records from PAR data using $C_{SW} = 0.47$ results on a mean absolute error equal to $65 \frac{W}{m^2}$ and incoming shortwave records significantly lower than available records. Therefore, we minimized the absolute error to obtain a site-specific mean C_{SW} for Lake Tahoe during Spring. The optimization of the empirical constant results in a

$C_{SW} = 0.511$ for which the mean absolute error is $55 \frac{W}{m^2}$ and modeled incoming shortwave in overall represents the available measurements from USCG (Figure 12-9).

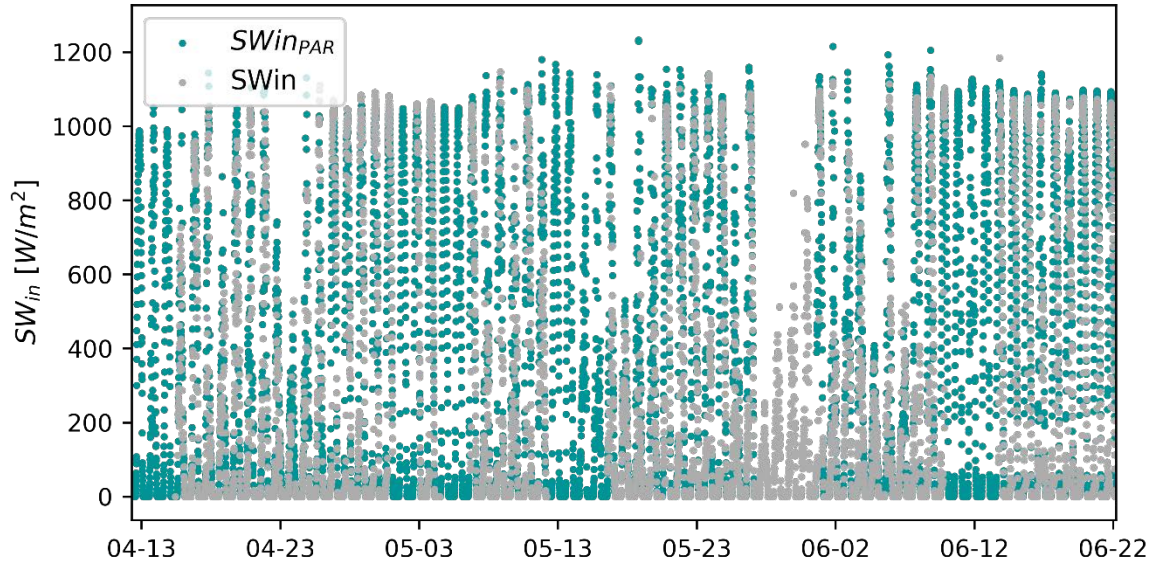


Figure 12-9. Comparison of modeled incoming shortwave time series estimated from PAR records (green dots) and incoming shortwave measurements from USCG (gray dots).

The incoming longwave input needed for the forcing conditions were estimated using Equation (12-2), air temperature records from the NASA buoys as described in Section 7.1.6, and cloud cover estimations following Martin & McCutcheon (1999),

$$LW_{in} = 0.937e^{-5} \times 0.97 \times 5.67e^{-8} \times ((AirT + 273.16)^6) \times (1 + 0.17 \times Cl), \quad (12-2)$$

where $AirT$ is the air temperature in Celsius, and Cl is the cloud cover estimation. Estimated incoming longwave radiation is shown in Figure 12-10 – (g) along the surface boundary conditions applied to the numerical model during the Spring 2011 (Figure 12-10 – (a to f)). The surface boundary conditions were modified by 0.9 and 1.1 for the wind speed and incoming shortwave radiation, respectively. The factors were applied following observed improvement on the model performance during Spring 2011.

In Figure 12-11, we present the comparison of the field records and the numerical results for the evolution of the temperature structure in the water column at MLTP and LTP. The temperature from the numerical model closely follows the onset of the stratification recorded on the field at LTP and MLTP, with a slight underestimation of the temperature at the surface (Figure 12-11 – MLTP 11-06-07). Nonetheless, the numerical model predicts the formation of the epilimnion and continue warming of the water column similarly to results presented in Section 7.1.6 (Figure 12-12).

Moreover, the Error norms, RMSE, and SS estimations indicate that temperature structure is, in overall, accurately predicted by the numerical model (Table 12-3). The SS results fall within the excellent category (Scheu et al., 2018), and Error norms (I_1 , I_2) and RMSE are comparable to available values in the literature (Rueda & Cowen, 2005). The norms I_1 and I_2 are on average 0.062 and 0.078, and the mean of the RMSE is $0.5^\circ C$, with the greatest error observed at TB2 and TB3 with $RMSE < 1^\circ C$.

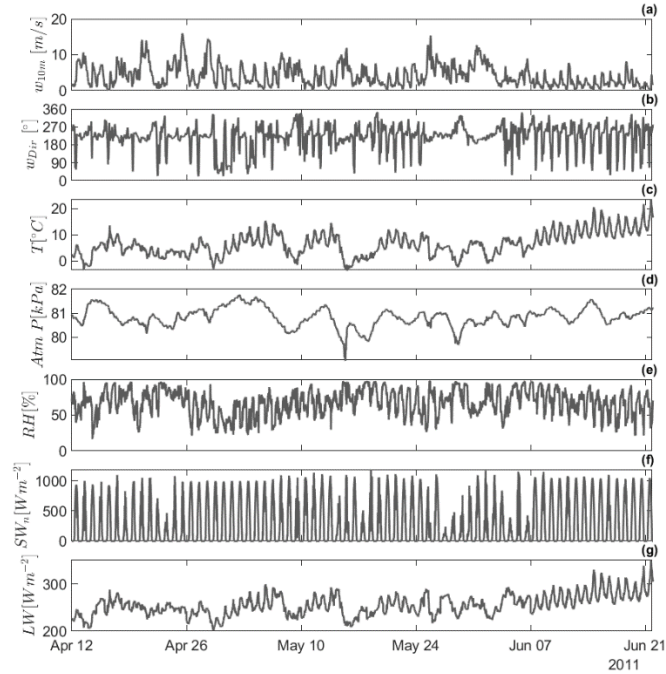


Figure 12-10. Numerical model surface boundary condition parameters from observed meteorological conditions for Spring 2011. Wind speed modified by a factor of 0.9 (a) and incoming shortwave radiation multiplied by 1.1. Time series plot of (a) wind speed, (b) wind direction, (c) air temperature, (d) atmospheric pressure, (e) relative humidity, (f) net shortwave radiation, and (g) incoming longwave.

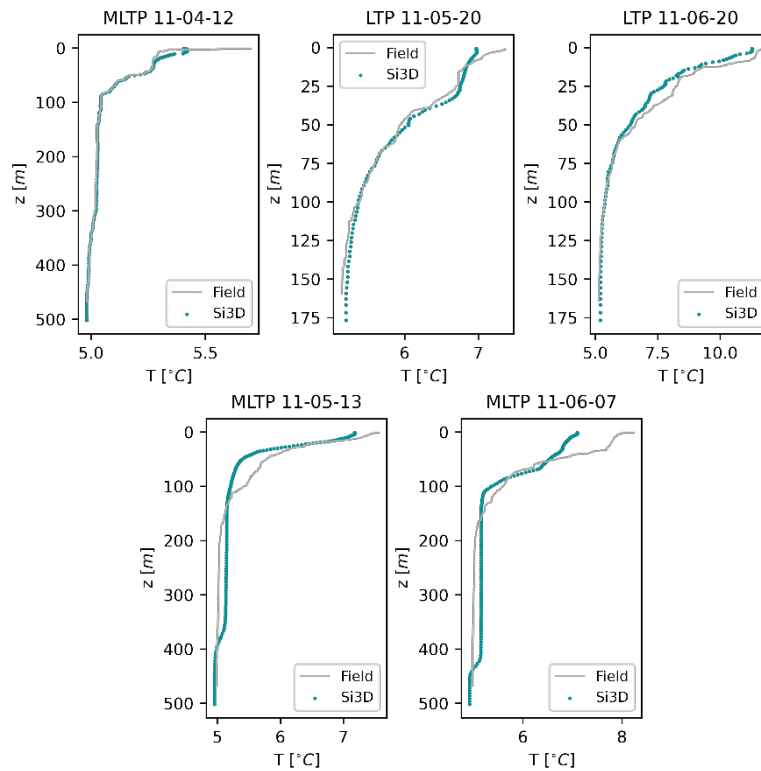


Figure 12-11. Validation of CTD profiles collected at LTP and MLTP. The title of individual plots indicates the site and date of the temperature profile. Snapshots show the vertical temperature structure of the PSi3D results (green dots) and the data collected on site (gray line).

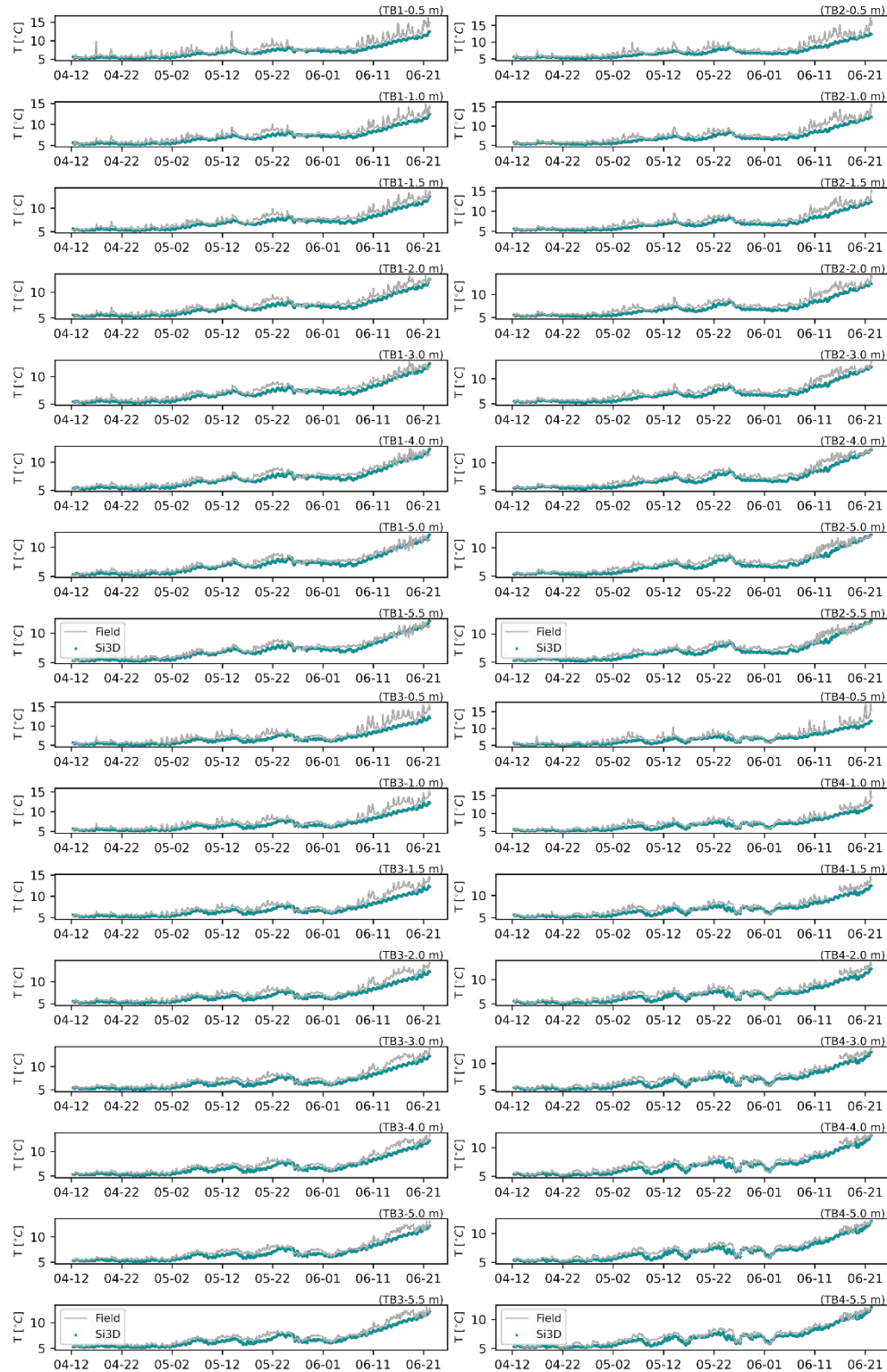


Figure 12-12. Temperature validation of the numerical results (green dots) and field records (gray line). Tile names indicate the site location from Figure 7-1 with the site followed by the depth of the measurement.

Table 12-3. Statistical metric estimations for model performance validation Spring 2011.

Site	SS	I_1	I_2	RMSE (°C)
<i>LTP</i>	0.860	0.018	0.026	0.160
<i>MLTP</i>	0.909	0.020	0.029	0.156
<i>TB1</i>	0.836	0.076	0.093	0.725
<i>TB2</i>	0.808	0.087	0.108	0.857
<i>TB3</i>	0.806	0.095	0.115	0.890
<i>TB4</i>	0.834	0.080	0.096	0.713

12.4. Validation of Summer 2011

During the Summer 2011, surface water temperatures changed from 9 °C to 20 °C, increasing the temperature gradient in the water column (hypolimnetic waters at ≈ 5 °C) and limiting the mixing dynamics and interaction of epilimnion (oxygen rich waters) and hypolimnion (nutrient rich waters). We then focused at predicting the lake hydrodynamics between June 20th and September 05th for which we applied factors of 0.85, 1.1, and 1.1 to the wind speed, incoming shortwave, and incoming longwave records, respectively (Figure 12-13).

In Figure 12-14 and Figure 12-15, we present the field measurements and numerical results for individual profiles of the vertical temperature structure and surface temperature time evolution, respectively, where good agreement in the overall dynamics can be concluded. Figure 12-14 shows the good prediction of P*Si*3D on the increasing surface temperature and strengthening of the stratification. Similarly, to the Summer 2018 validation, surface temperatures are slightly overestimated by ≈ 1.5 °C at the end of the study period. However, this slight overestimation of the surface temperature is only about 15% of the temperature range during the summer, and thus we conclude that the overall lake hydrodynamics during the Summer are properly represented by P*Si*3D-L. Furthermore, the performance metrics agree with those of good numerical model results (Table 12-4). The mean of the metrics used herein for all sites indicate an overall good performance of the lake model, and are consistent with other 3D modeling studies (e.g., $\overline{RMSE} = 1.9$ °C by Valipour et al., (2019a)).

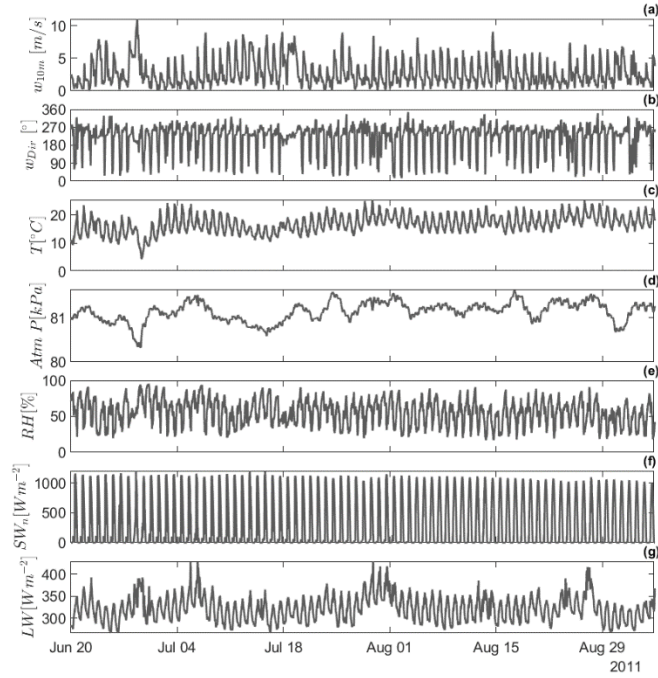


Figure 12-13. Numerical model surface boundary condition parameters from observed meteorological conditions for Summer 2011. Wind speed modified by a factor of 0.85 (a), incoming shortwave radiation multiplied by 1.1, and incoming longwave modified by a factor of 1.1 (g). Time series plot of (a) wind speed, (b) wind direction, (c) air temperature, (d) atmospheric pressure, (e) relative humidity, (f) net shortwave radiation, and (g) incoming longwave.

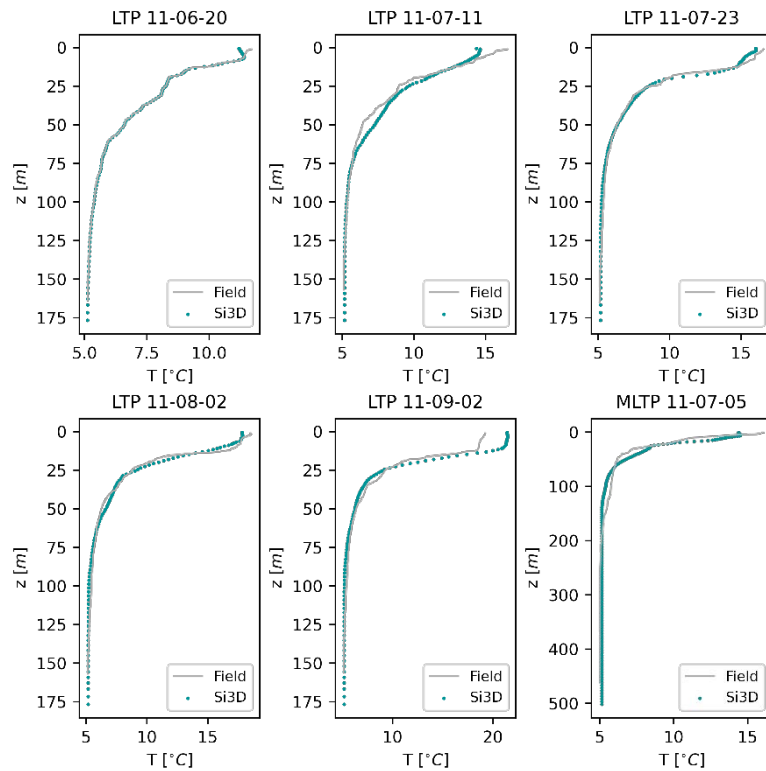


Figure 12-14. Validation of CTD profiles collected at LTP and MLTP. The title of individual plots indicates the site and date of the temperature profile. Snapshots show the vertical temperature structure of the PSi3D results (green dots) and the data collected on site (gray line).

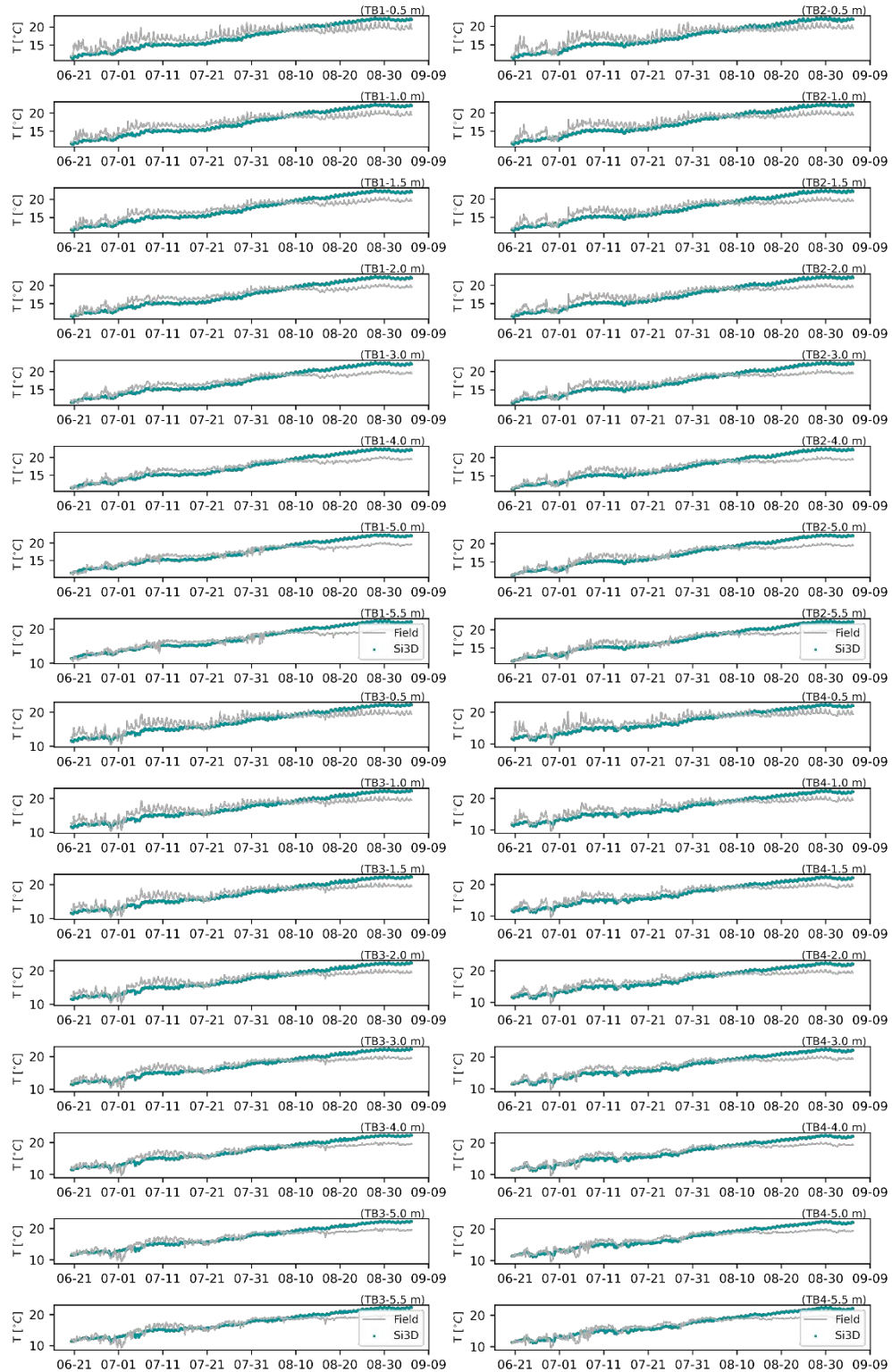


Figure 12-15. Temperature validation of the numerical results (green dots) and field records (gray line). Tile names indicate the site location from Figure 7-1 with the site followed by the depth of the measurement.

Table 12-4. Statistical metric estimations for model performance validation Summer 2011.

Site	SS	I_1	I_2	RMSE (°C)
<i>LTP</i>	0.982	0.031	0.049	0.387
<i>MLTP</i>	0.930	0.045	0.071	0.417
<i>TB1</i>	0.520	0.077	0.088	1.541
<i>TB2</i>	0.539	0.074	0.086	1.502
<i>TB3</i>	0.624	0.074	0.087	1.501
<i>TB4</i>	0.612	0.076	0.087	1.514

12.5. Validation of Fall 2011

Validation of Fall 2011 considers the lake dynamics between September 28th and December 18th to predict the weakening of the stratification and deepening of the thermocline. Similar to Fall 2018, epilimnetic water temperature decreased as atmospheric conditions promoted the heat loss from the water column (Figure 12-16). During Fall 2011, lower incoming shortwave radiation and cooler air temperatures contributed to a cooling of the epilimnion from 18 °C to \approx 7 °C, which resulted in a deepening of the thermocline to about 50 m deep by mid-December. After a sensitivity analysis, numerical results performance increased when applying a 0.9 factor to the wind speed (Figure 12-16).

Comparison of individual vertical temperature profiles at LTP and MLTP show a good agreement on the weakening of the stratification as epilimnetic water temperature decreases and the thermocline deepens (Figure 12-17). The Skill Score (SS) for MLTP and LTP fall within the excellent category, and the error norms and RMSE are comparable to other 3D modeling lake studies (Table 12-5) (e.g., Antenucci et al., (2000); Hodges et al., (2000); Rueda & Cowen, (2005)). In addition, surface temperature cooling at mid-lake locations (TBx in Figure 7-1) is in good harmony with the field observations during the study period (Figure 12-18), and are supported by the good estimates of the statistical metrics used to evaluate the model's performance (Table 12-5).

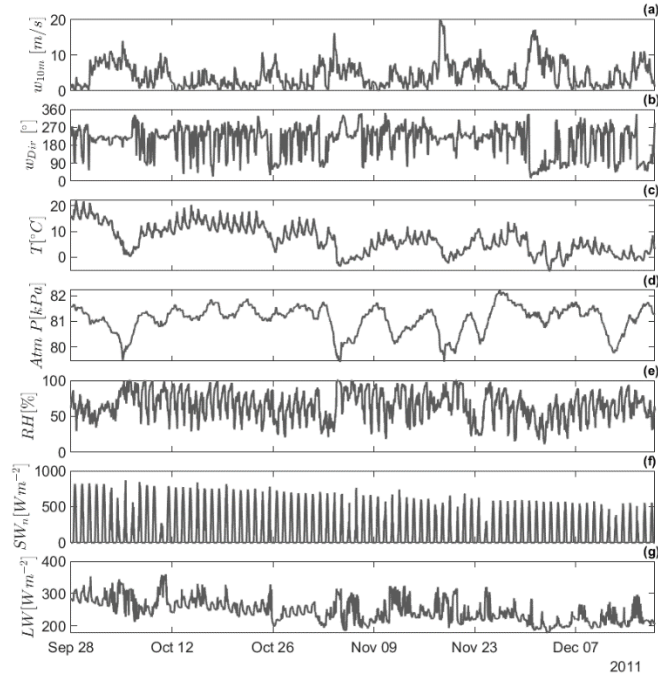


Figure 12-16. Numerical model surface boundary condition parameters from observed meteorological conditions for Fall 2011. Wind speed modified by a factor of 0.9. Time series plot of (a) wind speed, (b) wind direction, (c) air temperature, (d) atmospheric pressure, (e) relative humidity, (f) net shortwave radiation, and (g) incoming longwave.

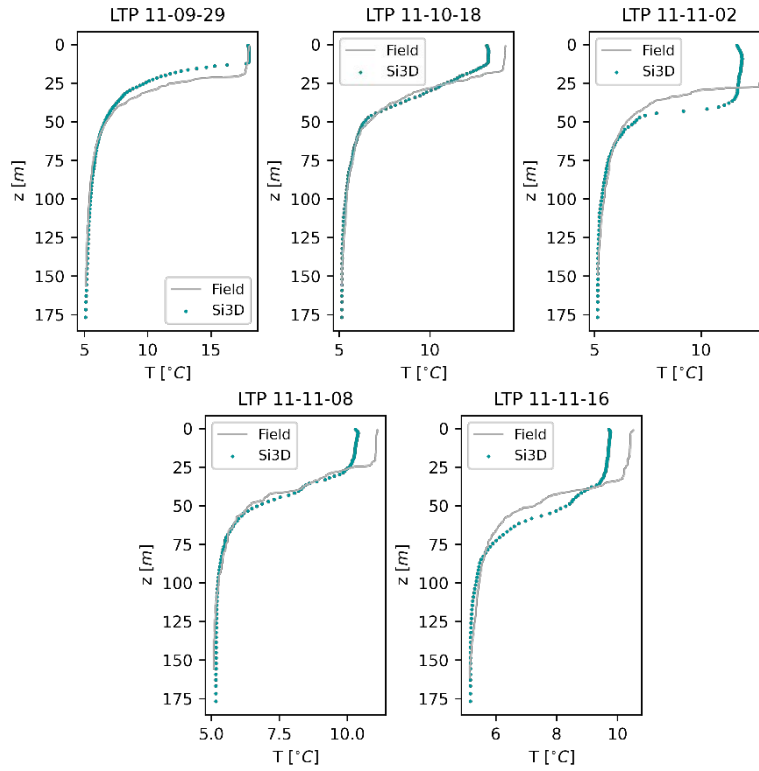


Figure 12-17. Validation of CTD profiles collected at LTP. The title of individual plots indicates the site and date of the temperature profile. Snapshots show the vertical temperature structure of the Psi3D results (green dots) and the data collected on site (gray line).

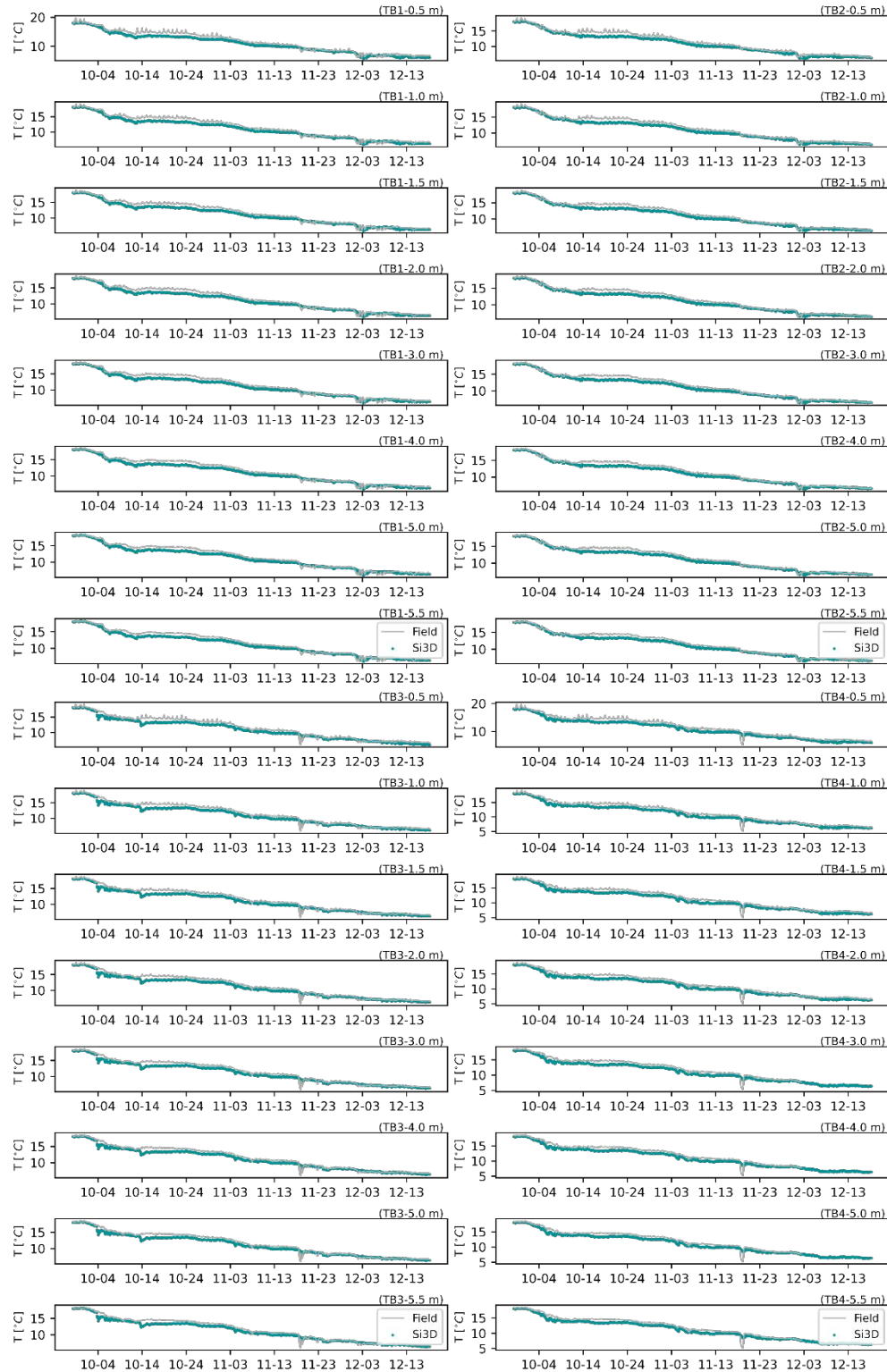


Figure 12-18. Temperature validation of the numerical results (green dots) and field records (gray line). Tile names indicate the site location from Figure 7-1 with the site followed by the depth of the measurement.

Table 12-5. Statistical metric estimations for model performance validation Fall 2011.

Site	SS	I_1	I_2	RMSE (°C)
<i>LTP</i>	0.891	0.051	0.084	0.654
<i>MLTP</i>	0.924	0.018	0.027	0.154
<i>TB1</i>	0.952	0.057	0.065	0.784
<i>TB2</i>	0.956	0.050	0.059	0.715
<i>TB3</i>	0.951	0.055	0.064	0.774
<i>TB4</i>	0.930	0.063	0.070	0.829

13. Appendix D: Biogeochemical and ecological data available for Lake Tahoe

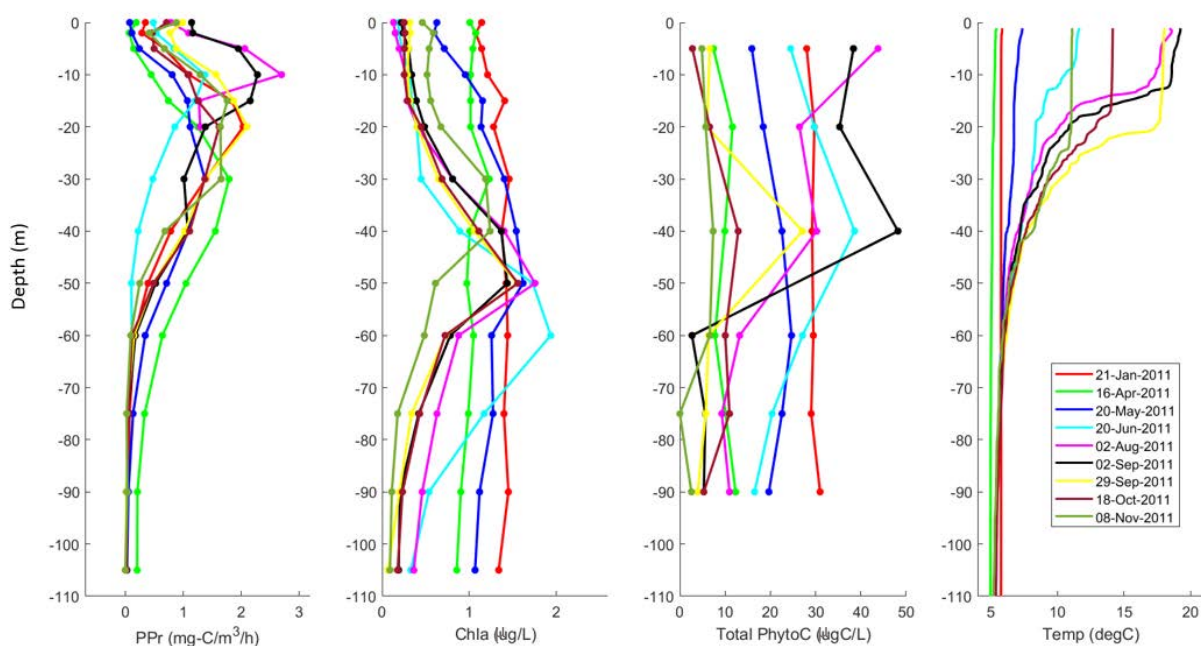


Figure 13-1. Summary key profiles measured at LTP in 2011: Primary productivity of phytoplankton (PPr), chlorophyll-a (Chla), total phytoplankton carbon (PhytoC), and lake temperature (Temp)

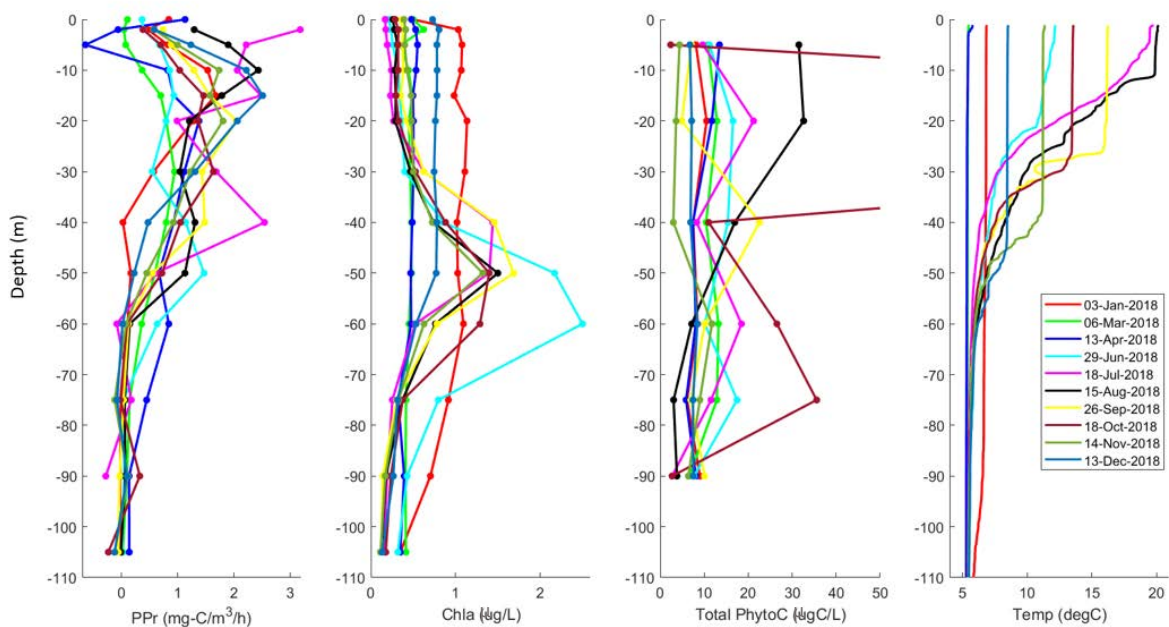


Figure 13-2. Summary key profiles measured at LTP in 2018: Primary productivity of phytoplankton (PPr), chlorophyll-a (Chla), total phytoplankton carbon (PhytoC), and lake temperature (Temp)

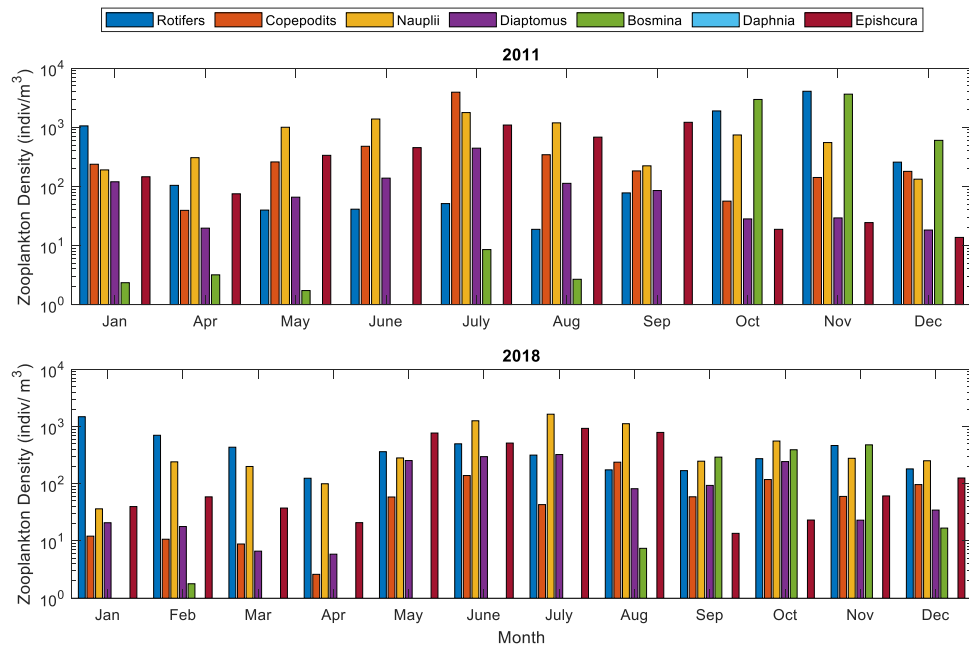


Figure 13-3. Zooplankton densities measured in 2011 (top) and 2018 (bottom).

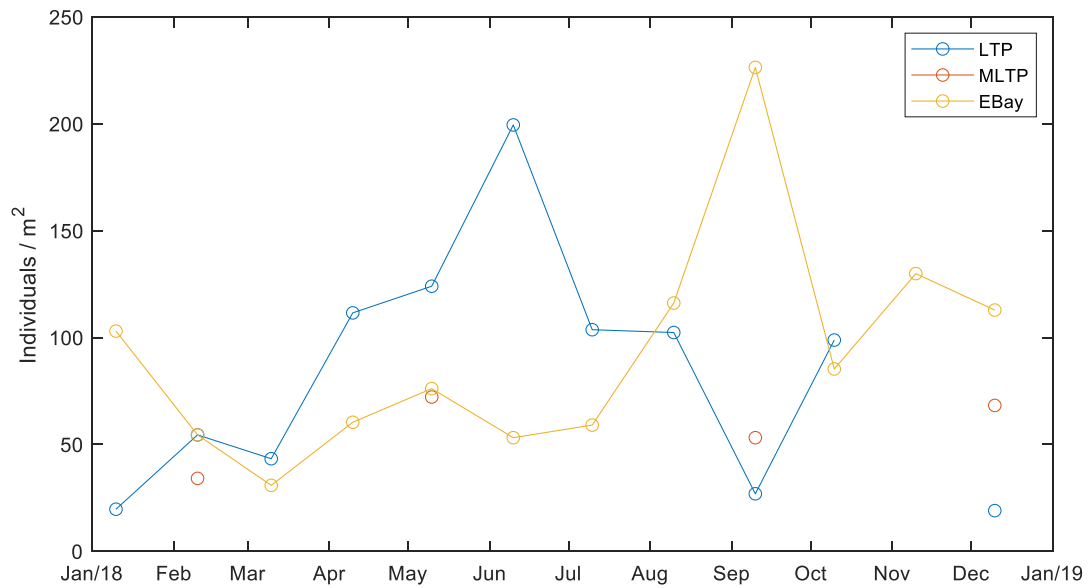


Figure 13-4. Mysis densities measured in 2018 at different sites: LTP, MLTP and Emerald Bay (EBay)

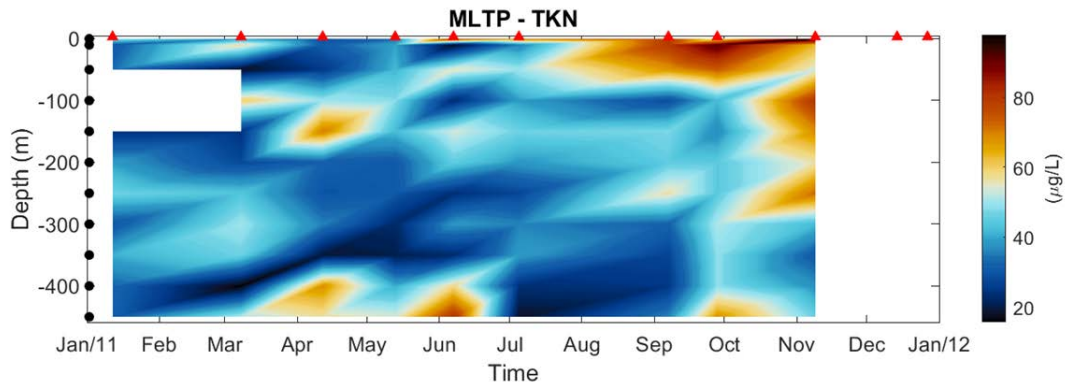


Figure 13-5. Total Kjeldahl nitrogen (TKN) measured at MLTP in 2011

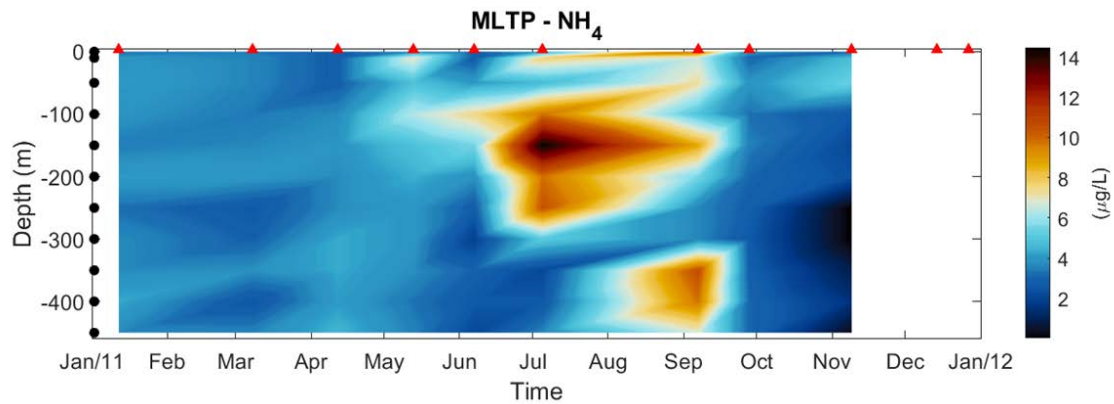


Figure 13-6. Ammonium (NH_4) measured at MLTP in 2011

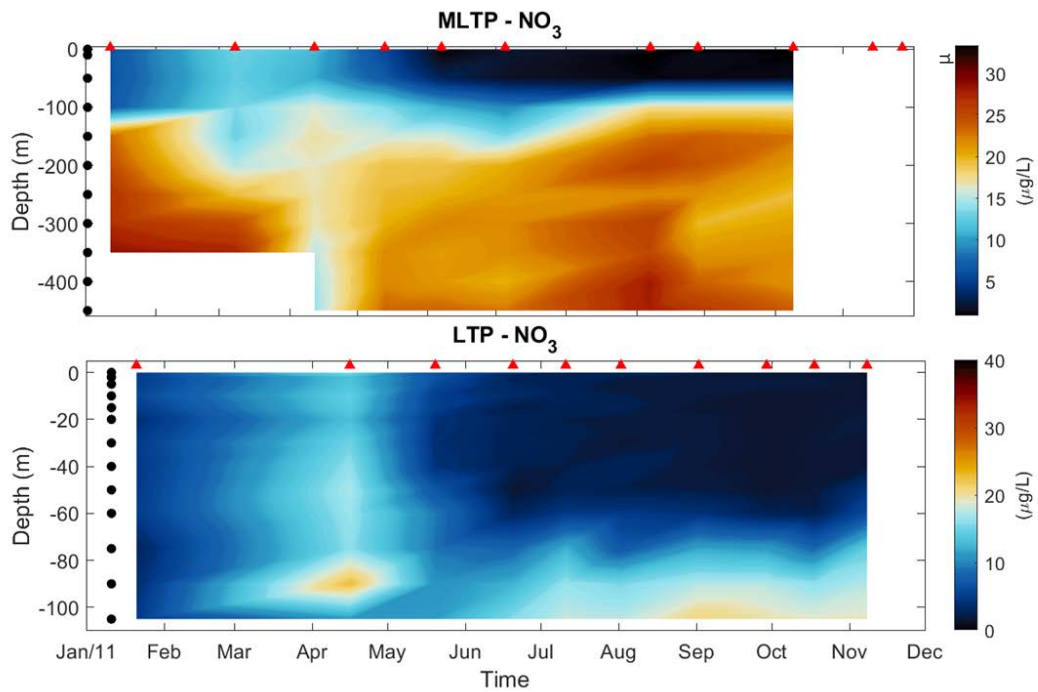


Figure 13-7. Nitrate (NO_3) measured at MLTP (top) and LTP (bottom) in 2011

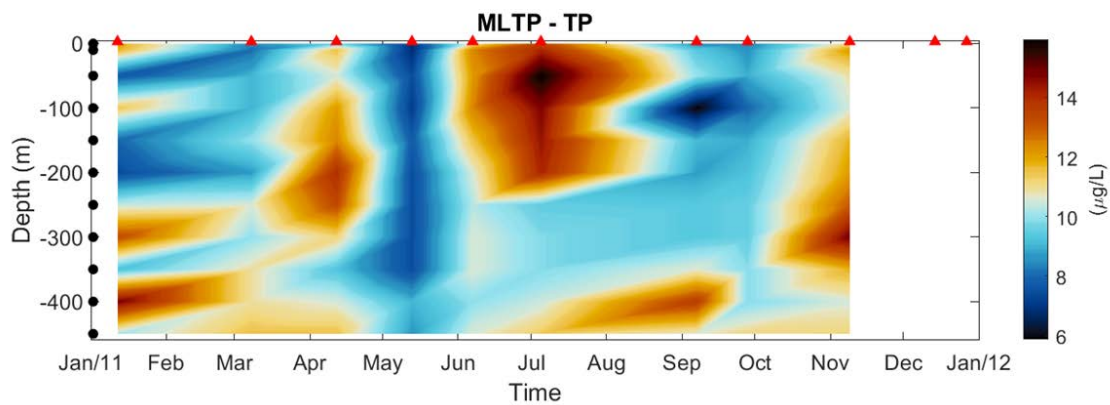


Figure 13-8. Total phosphorus (TP) measured at MLTP in 2011

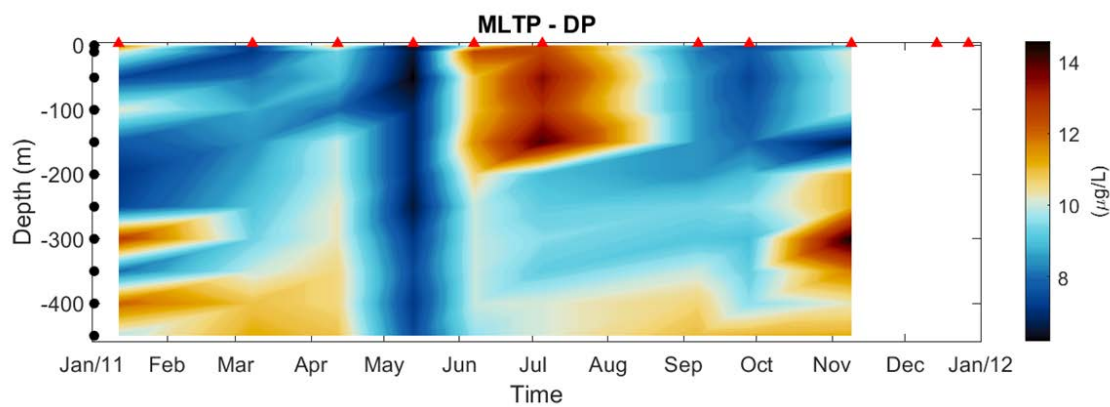


Figure 13-9. Dissolved phosphorus (DP) measured at MLTP in 2011

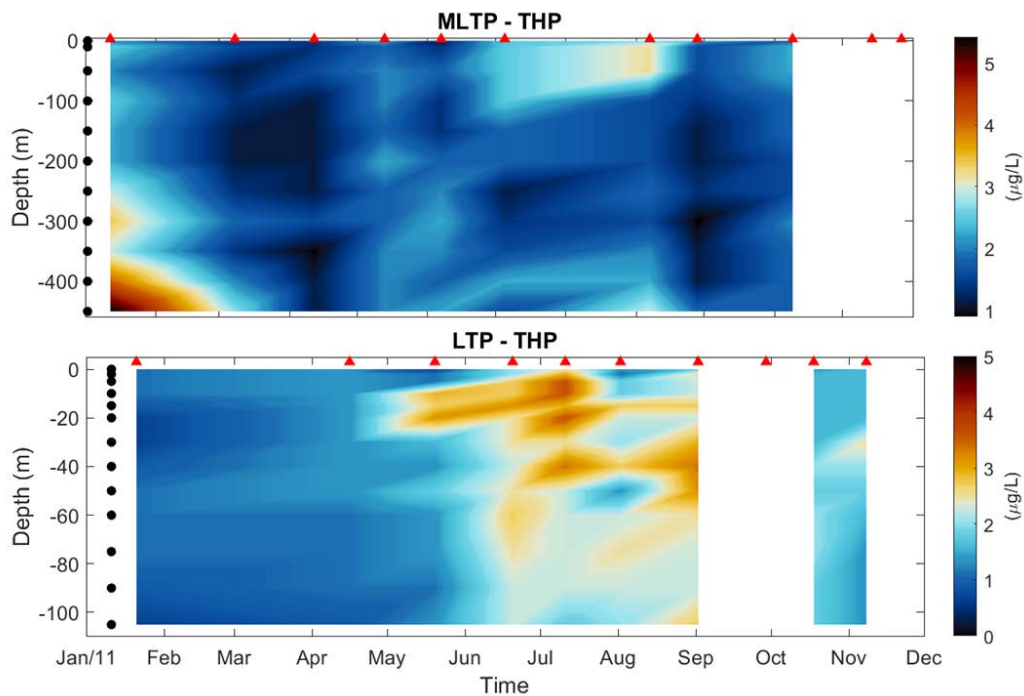


Figure 13-10. Total hydrolyzable phosphorus (THP) measured at MLTP (top) and LTP (bottom) in 2011

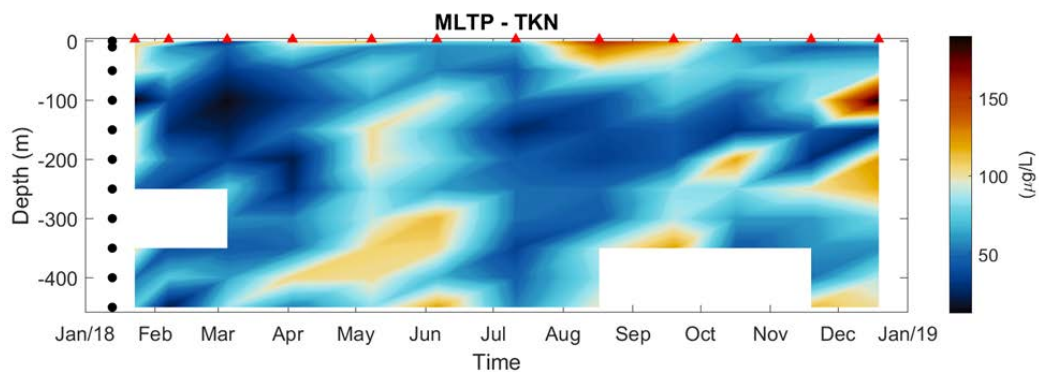


Figure 13-11. Total Kjeldahl nitrogen (TKN) measured at MLTP in 2018

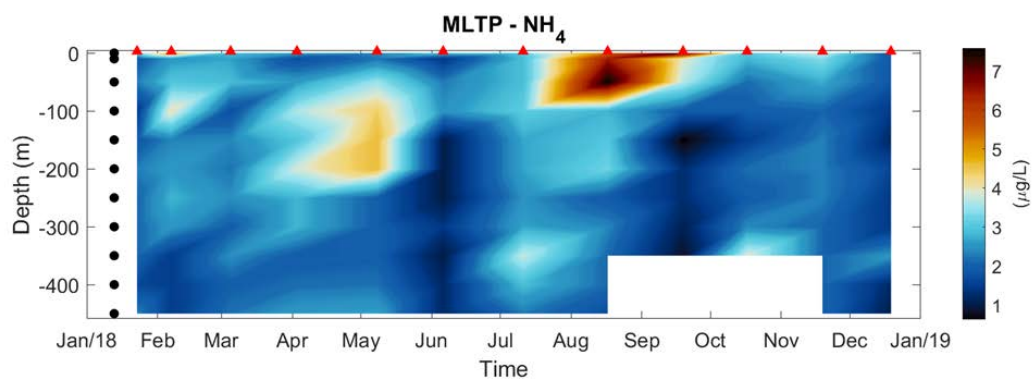


Figure 13-12. Ammonium (NH_4) measured at MLTP in 2018

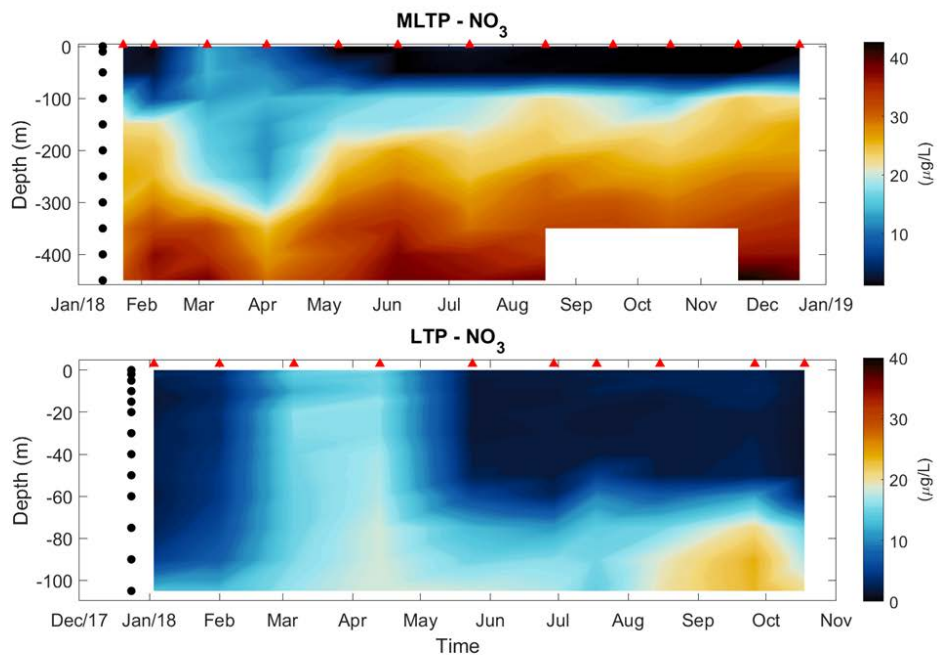


Figure 13-13. Nitrate (NO_3) measured at MLTP (top) and LTP (bottom) in 2018

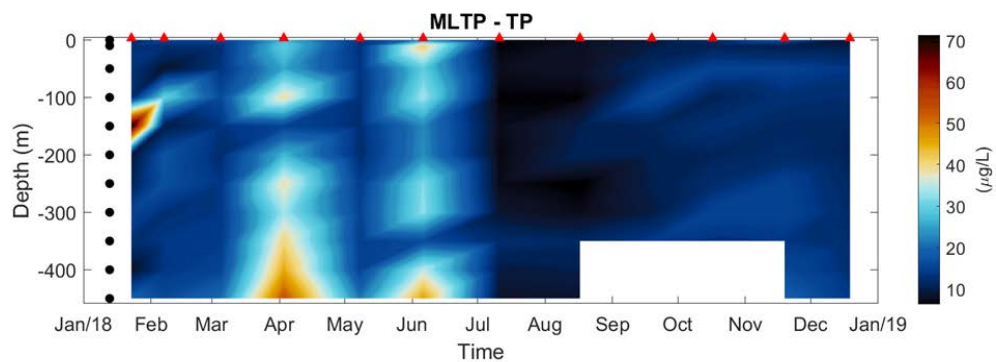


Figure 13-14. Total phosphorus (TP) measured at MLTP in 2018

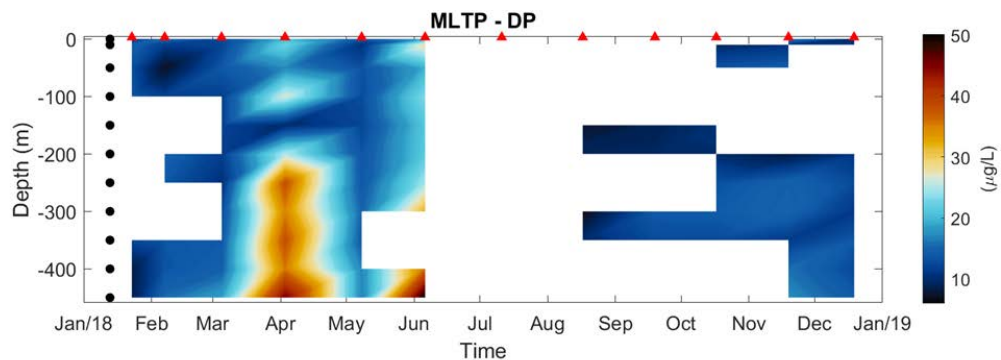


Figure 13-15. Dissolved phosphorus (DP) measured at MLTP in 2018

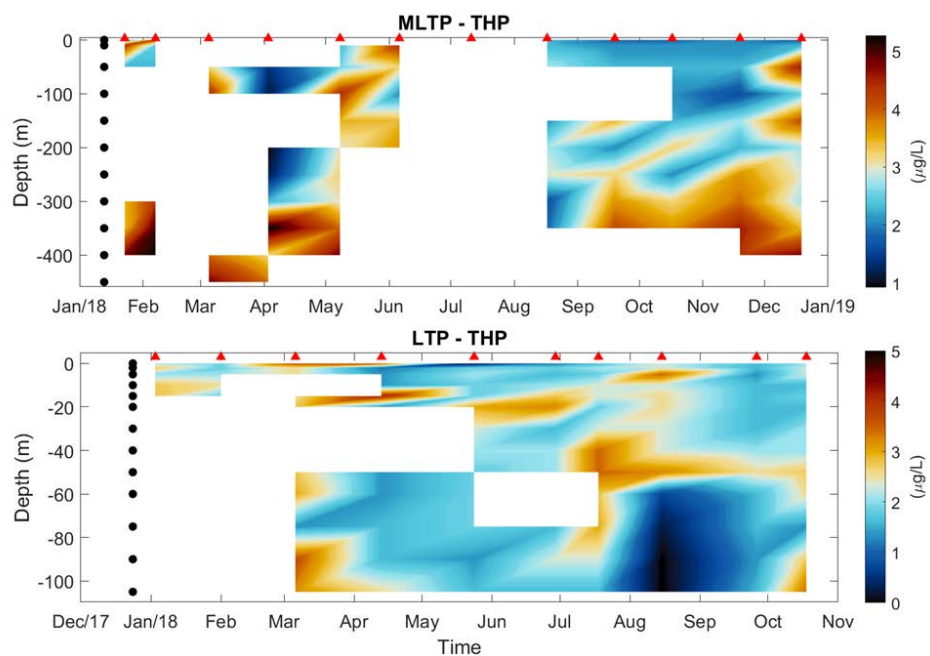


Figure 13-16. Total hydrolyzable phosphorus (THP) measured at MLTP (top) and LTP (bottom) in 2018

14. Appendix E: PSi3D-AEM Model Results

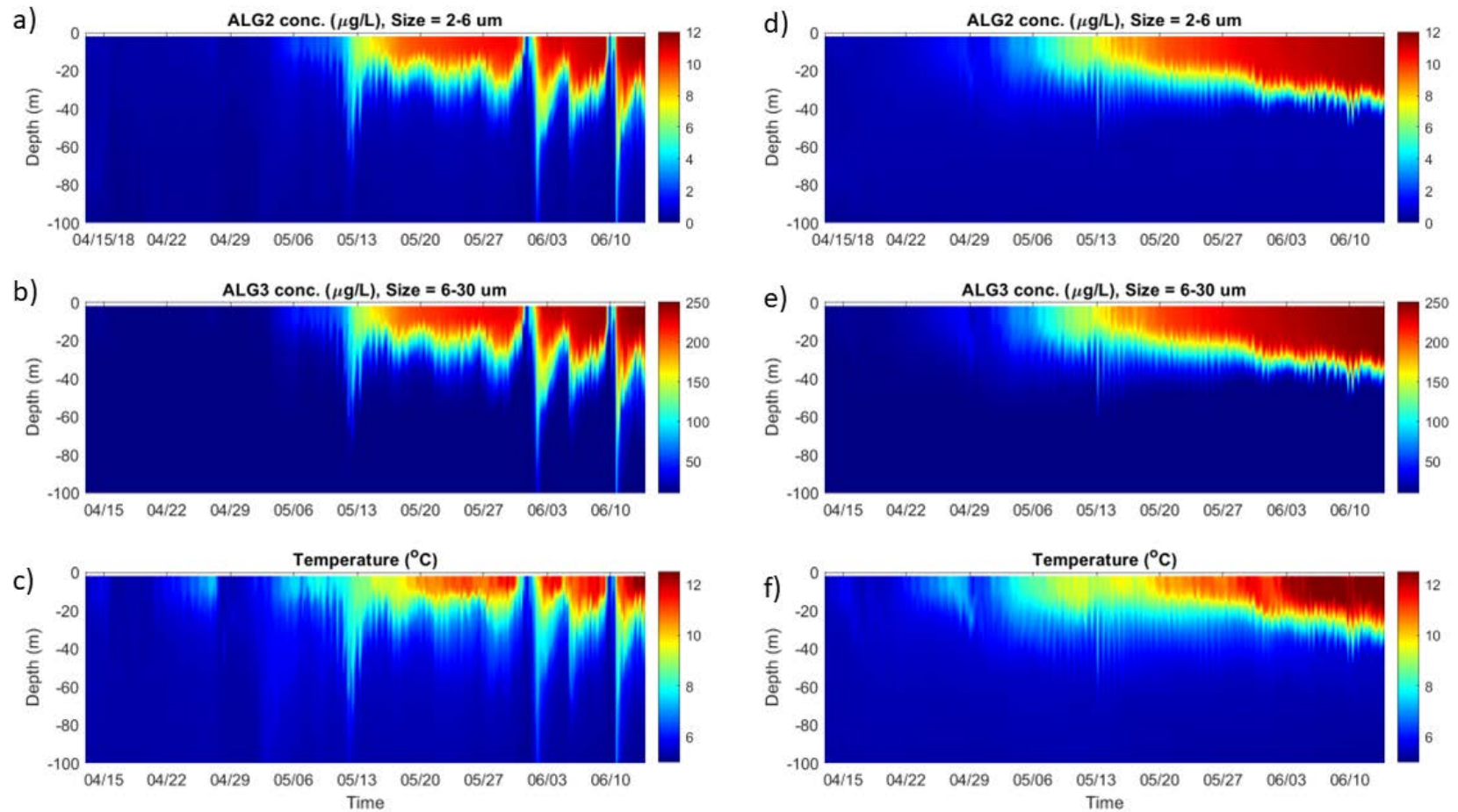


Figure 14-1. Model time series of phytoplankton carbon of group 2 (a,d) and group 3 (b,e) in spring 2018 in the top 100 m at LTP (a-c) and MLTP (d-e) assuming that only growth affects the phytoplankton dynamics. Lake temperatures during the same period at LTP (c) and MLTP (f)

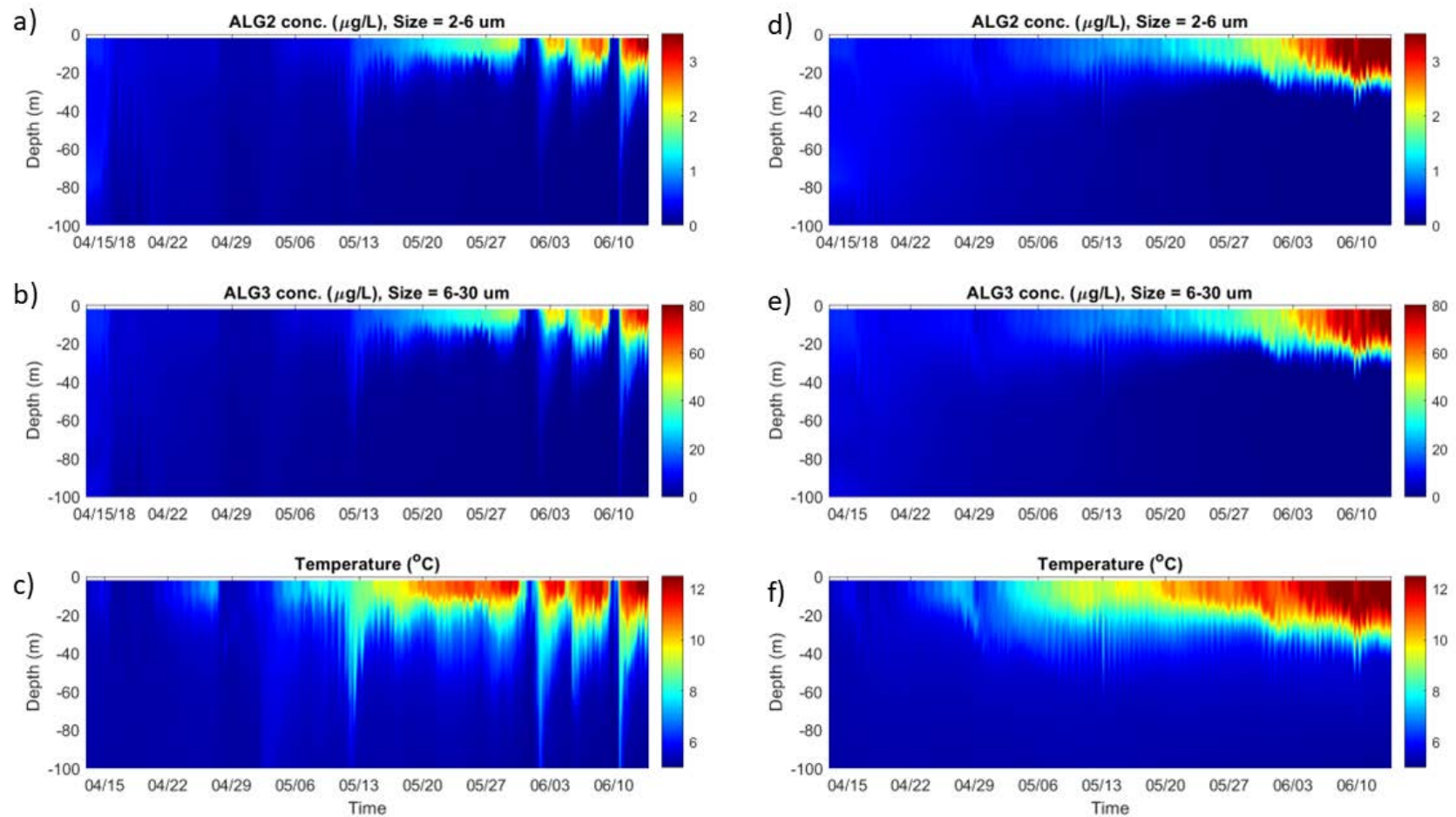


Figure 14-2. Model time series of phytoplankton carbon of group 2 (a,d) and group 3 (b,e) in spring 2018 in the top 100 m at LTP (a-c) and MLTP (d-e) assuming that only growth and mortality affect the phytoplankton dynamics. Lake temperatures during the same period at LTP (c) and MLTP (f)

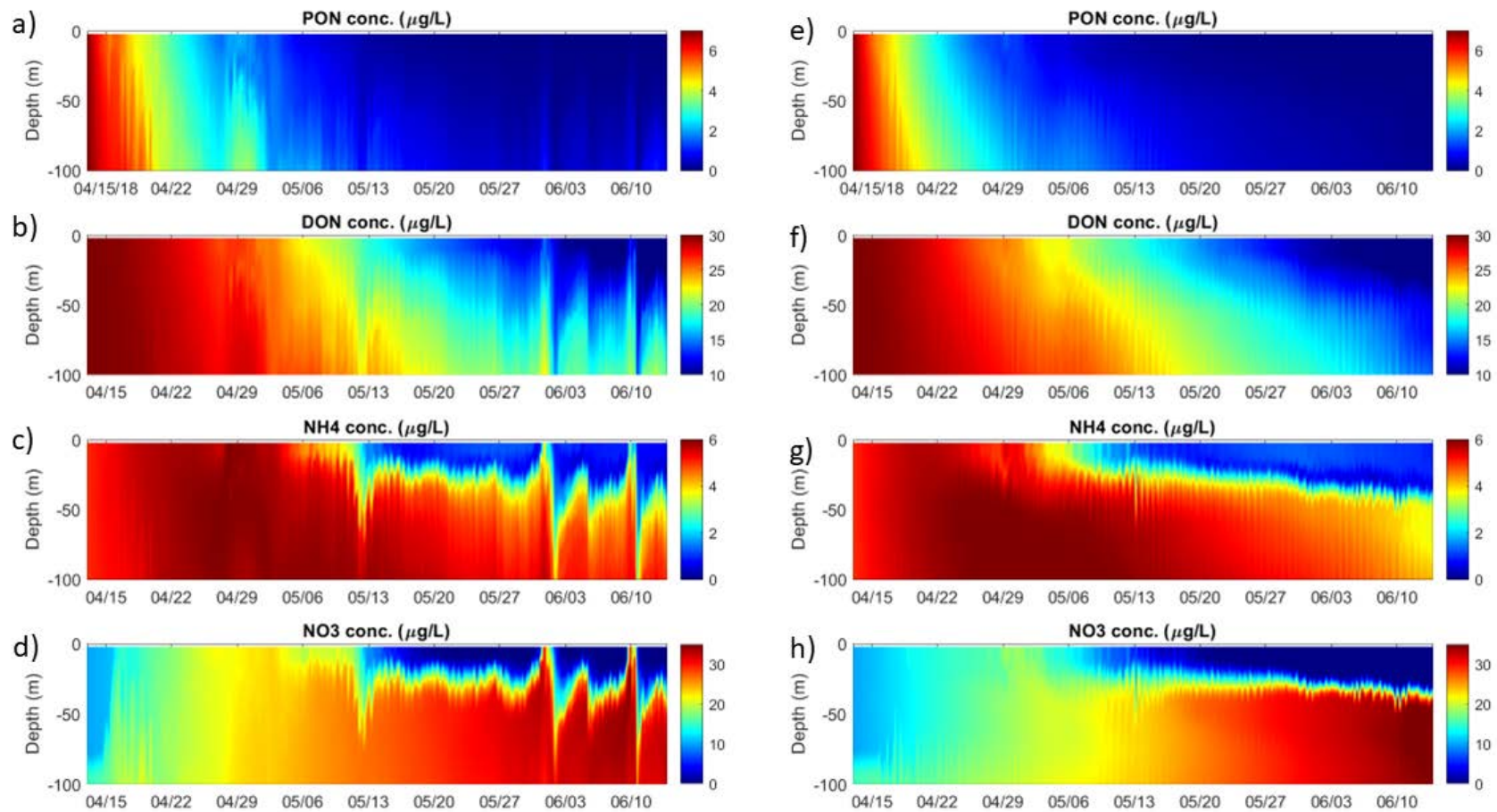


Figure 14-3. Model time series of nitrogen forms: PON (a,e), DON (b,f), NH_4 (c,g), NO_3 (d,h) in spring 2018 in the top 100 m at LTP (a-d) and MLTP (e-h) assuming that only growth affects the phytoplankton dynamics.

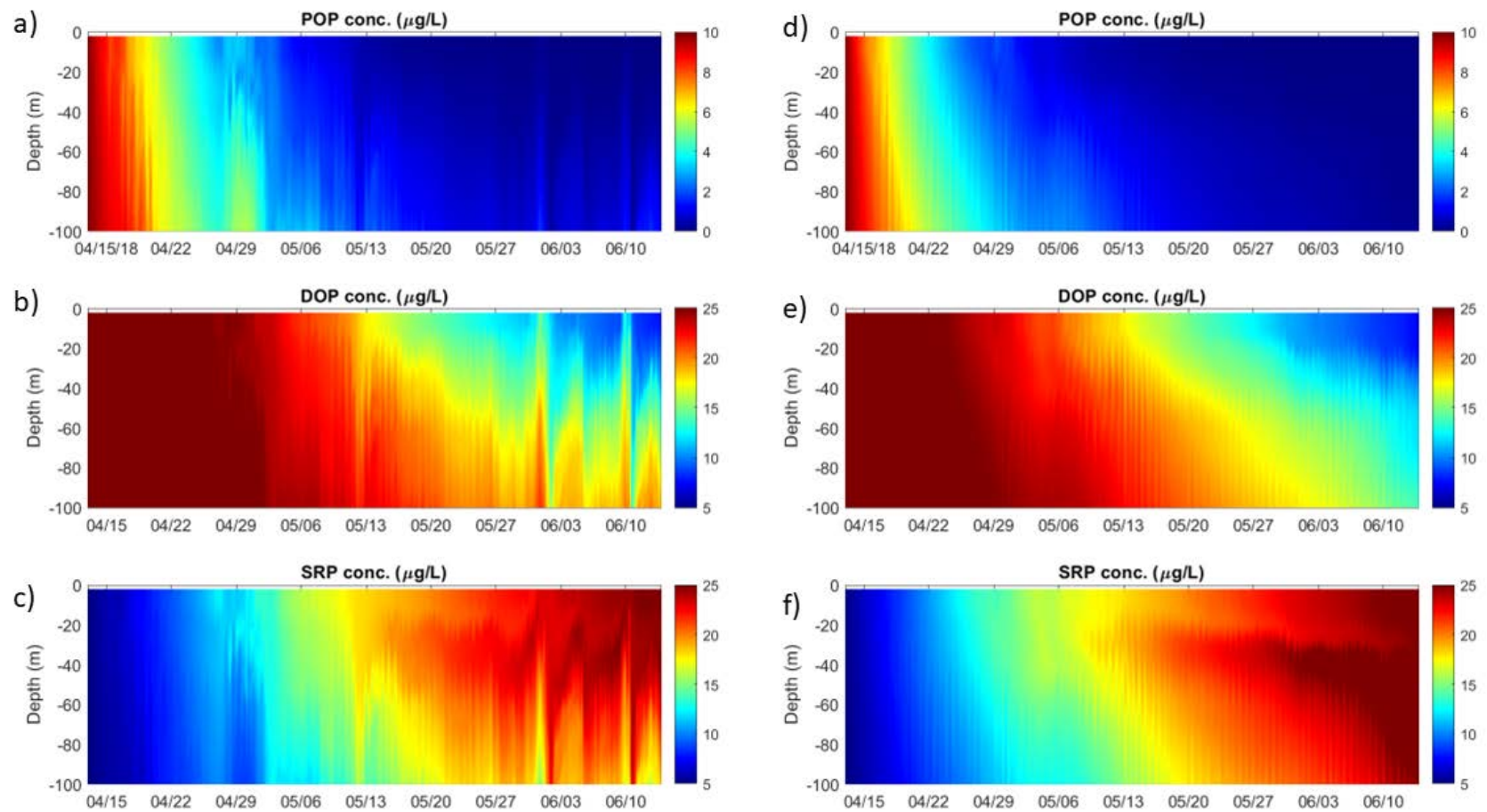


Figure 14-4. Model time series of phosphorus forms: POP (a,d) DOP (b,e), SRP (c,f), in spring 2018 in the top 100 m at LTP (a-e) and MLTP (d-f) assuming that only growth affects the phytoplankton dynamics.

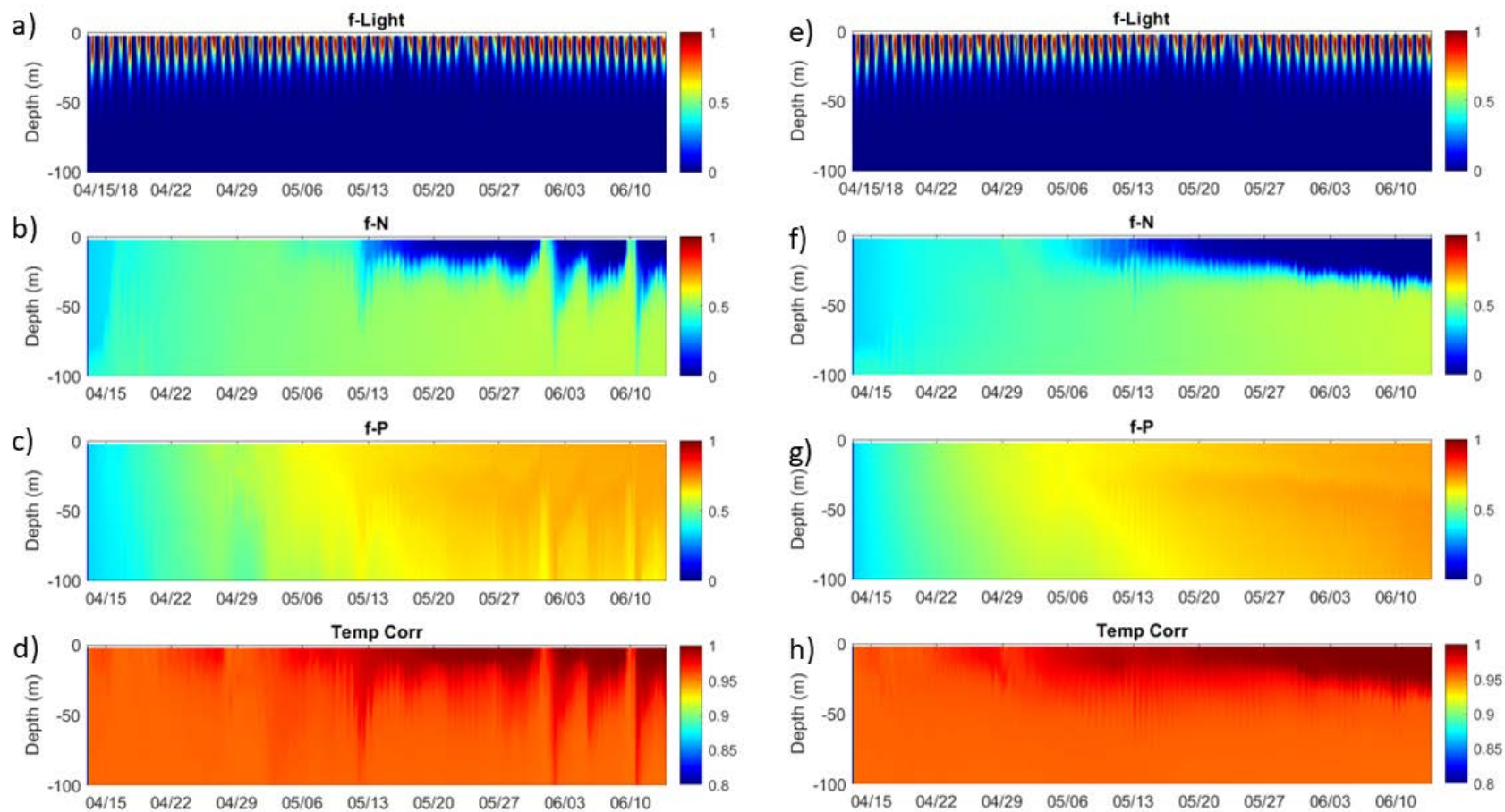


Figure 14-5. Model time series of phytoplankton growth limiting factors: light (a,e), nitrogen (b,f), phosphorus (c,g), temperature (d,h) in spring 2018 in the top 100 m at LTP (a-d) and MLTP (e-h) assuming that only growth affects the phytoplankton dynamics.

15. References

Introduction

- Jorgensen, S.E. and G. Bendoricchio. 2001. Fundamentals of ecological modelling. Applications in Environmental Management and Research. Elsevier
- Losada, J. P. (2001). A deterministic model for lake clarity. Application to management of Lake Tahoe (California-Nevada), USA. PhD dissertation, Universitat de Girona, Spain.
- Mooij, W.M., Trolle, D., Jeppesen, E., Arhonditsis, G., et al. 2010. Challenges and opportunities for integrating lake ecosystem modelling approaches. *Aquatic Ecology* 44: 633–667.
- Naranjo, R.C., Work, P., Heyvaert, A., Schladow, G., Cortes, A., Watanabe, S., Tanaka, L. and Elci, S. 2022. Seasonal and Long-Term Clarity Trend Assessment of Lake Tahoe, California–Nevada. US Geological Survey Scientific Investigations Report 2022-5070.
- Sahoo, G., Schladow, G., Reuter, J. and Coats, R. 2011. Effects of climate change on thermal properties of lakes and reservoirs, and possible implications. *Stochastic Envir. Res. Risk Assess.* 25:445-456
- Sahoo, G., A. Forrest, G. Schladow, J. Reuter, R. Coats, M. Dettinger. 2016. Climate change impacts on lake thermal dynamics and ecosystem vulnerabilities. *Limnol. Oceanogr.* 61: 496-507
- Swift, T.J., J. Losada, G. Schladow, J. Reuter, A. Jassby, C. Goldman. 2006. Water clarity modeling in Lake Tahoe: Linking suspended matter characteristics to Secchi depth. *Aquat. Sci.* 68, 1–15
- TERC 2021. Tahoe: State of the lake report 2021. <https://tahoe.ucdavis.edu/state-lake-archive>

Data Description and Availability

- Brzezinski, M.A. 1987. Colorimetric Determination of Nanomolar Concentrations of Ammonium in Seawater Using Solvent Extraction. *Marine Chemistry* 20: 277-288.
- Environmental Protection Agency, method 350.1
- Environmental Protection Agency, method 351.2
- Environmental Protection Agency, method 365.3
- Fishman M.J. and L.C. Friedman (eds.) 1985. Methods for the Determination of Inorganic Substances in Water and Fluvial Sediments. Open-File Report 85-495. Denver, Colorado.
- Goldman, C.R. 1974. Eutrophication of Lake Tahoe Emphasizing Water Quality. EPA–600/3-74-034. U S. Govt. Printing Office, Washington, D.C. 408pp.
- Greenberg. 1995. Standard Methods for the Examination of Water and Wastewater, 19th Edition, Method 4500-P E.
- Kamphake, L.J., S.A. Hannah, and J.M. Cohen. 1967. Automated analysis for nitrate by hydrazine reduction. *Water Research.* 1:205-216.
- Liddicoat, M.I., S. Tibbits, and E.I. Butler. 1975. The Determination of Ammonia in Seawater. *Limnol. Oceanogr.* 20:131-132.
- Murphy, J. and Riley, J.P. 1962. A Modified Single Solution Method for the Determination of Phosphate in

Natural Waters. *Analytica Chimica Acta* 27:31-36.

Richard J. Wagner, Robert W. Boulger, Jr., Carolyn J. Oblinger, and Brett A. Smith. 2006. Guidelines and Standard Procedures for Continuous Water-Quality Monitors: Station Operation, Record Computation, and Data Reporting. USGS Techniques and Methods 1–D3. <https://pubs.usgs.gov/tm/2006/tm1D3/pdf/TM1D3.pdf>

Solorzano, L. 1969. Determination of Ammonia in Natural Waters by the Phenolhypochlorite Method, *Limnol. Oceanogr.* 14:799-801.

State Water Resources Board. Quick Chem Method No.10-107-06-2-F. Revision: D. Diamond. June 1986.

Strickland, J.D.H. and T.R. Parsons. 1972. A Practical Handbook of Seawater Analysis. Bulletin 167. Fisheries Research Board of Canada. Ottawa, Ontario, Canada.

Turnipseed, P. and Vernon B. Sauer. 2010. Discharge Measurements at Gaging Stations. USGS Techniques and Methods 3-A8. (<https://pubs.usgs.gov/tm/tm3-a8/tm3a8.pdf>)

Phytoplankton

Goldman, C. R. 1963, Proc. Cony. Prim. Product. Meas., Marine and Freshwater (M. S. Doty, ed.), 103-113. Div. Teeh. Information Report, TID-7633, U.S. Atomic Energy Commission

Hasle, G. R. 1978. Using the inverted microscope. In Sournia, A. (ed.), *Phytoplankton Manual*. Unesco, Paris, pp. 191–196.

Lavorel, S., S. McIntyre J. Landsberg, and T. D. A. Forbes. 1997. Plant functional classifications: from general groups to specific groups based on response to disturbance. *Trends Ecol. Evol.* 12:474–78.

Litchman, E., P. T. Pinto, C. A. Klausmeier, M. K. Thomas and K. Yoshiyama. 2010. Linking traits to species diversity and community structure in phytoplankton. *Hydrobiologia* 653:15–28.

McGill, B. J., Brian J. Enquist, Evan Weiher and Mark Westoby. 2006. Rebuilding community ecology from functional traits. *TRENDS in Ecology and Evolution* 21(4):178-184.

Reynolds, C. S. 1984. *The Ecology of Freshwater Phytoplankton*. Cambridge University Press, Cambridge, 384 pp.

Rocha, O. and A. Duncan. 1985. The relationship between cell carbon and cell volume in freshwater algal species used in zooplanktonic studies. *J. Plankton Research*. 7(2): 297-294

Utermöhl, H. 1958. Zur Vervollkommnung der quantitativen Phytoplankton-Methodik. *Internationale Vereinigung für Theoretische und Angewandte Limnologie: Mitteilungen* 9:1, 1-38.

Winder, M. 2009. Photosynthetic picoplankton dynamics in Lake Tahoe: temporal and spatial niche partitioning among prokaryotic and eukaryotic cells. *Journal of Plankton Research*. Volume 30(11):1307–1320.

Zooplankton

APHA, 1998. *Standard Methods for Examination of Water and Wastewater*. American Public Health Association, Washington.

Balcer, M.D., N.L. Korda & S.I. Dodson, 1984. *Zooplankton of the Great Lakes. A guide to the identification and ecology of the common crustacean species*. University of Wisconsin Press, Madison.

- Beeton, AM. 1959. Photoreception in the opossum shrimp, *Mysis relicta* Lovén. *Biological Bulletin* 116(2): 204-216.
- Bess, Z, S. Chandra, S. Kelson, E. Suenaga, A. Heyvaert. 2021. Zooplankton influences on the phytoplankton, water clarity, and nutrients in Lake Tahoe. *Aquatic Sciences*. 83(2). DOI: 10.1007/s00027-020-00772-6
- Bleiwas, A.H., P.M. Stokes. 1985. Collection of large and small food particles by *Bosmina*. *Limnology and Oceanography*. 30(5): 1090-1092.
- Boscarino B, Rudstam LG, Minson MA, & Freud EA. 2010. Laboratory-derived light and temperature preferences of juvenile mysid shrimp, *Mysis diluviana*. *Journal of Great Lakes Research* 36: 699-706.
- Bowers, J.A., and N.E. Grossnickle, 1978, The herbivorous habits of *Mysis relicta* in Lake Michigan. *Limnology & Oceanography* 23(4): 767-776
- Brooks, J.L., 1959. Cladocera. In: Edmondson, W.T. (ed.), *Freshwater Biology*. Wiley, New York: 587-656.
- Burns, C. and F.H. Rigler, 1967, Comparisons of Filtering of *Daphnia rosea* in Lake Water and Suspensions of Yeast. *Limnology and Oceanography*. <https://doi.org/10.4319/lo.1967.12.3.0492>
- Burgi, H-R., J.J. Elser, R.C. Richards, and C.R. Goldman, 1993, Zooplankton patchiness in Lake Tahoe and Castle Lake USA. *Vereinigung für Theoretische und Angewandte Limnologie*, 25:378-382. <https://doi.org/10.1080/03680770.1992.11900140>
- Byron E., P. Sawyer, C.R. Goldman, 1986, The recurrence of *Daphnia rosea* in Lake Tahoe: analysis of a population pulse. *J Plankton Res* 8:771–783. <https://doi.org/10.1093/plankt/8.4.771>
- Cooper S & Goldman CR. 1980. Opossum shrimp (*Mysis relicta*) predation on zooplankton. *Canadian Journal of Fisheries and Aquatic Sciences* 37(6):909-919.
- De Melo, R. & P.D.N. Hebert, 1994. A taxonomic reevaluation of North American Bosminidae. *Canadian Journal of Zoology* 72: 1808-1825.
- DeMott WR (1982) Feeding selectivities and relative ingestion rates of *Daphnia* and *Bosmina*. *Limnol Oceanogr* 27:518–527. <https://doi.org/10.4319/lo.1982.27.3.0518>
- Elser J.J., H.J. Carney, C.R. Goldman, 1990 The zooplankton-phytoplankton interface in lakes of contrasting trophic status: an experimental comparison. *Hydrobiologia* 200(201):69–82. <https://doi.org/10.1007/BF02530330>
- Elser J.J., C.R. Goldman, 1991, Zooplankton effects on phytoplankton in lakes of contrasting trophic status. *Limnology & Oceanography* 36:64– 90. <https://doi.org/10.4319/lo.1991.36.1.0064>
- Folt, C.L. 1982. The effects of species interactions on the feeding and mortality of zooplankton. Ph.D. thesis, University of California Davis.
- Folt, C., and C.R. Goldman, 1981, Allelopathy between Zooplankton: A Mechanism for Interference Competition. *Science* 203(4512): 1133-135. <https://www.jstor.org/stable/1686665>
- Folt, C., and P.C. Shulze, 1993, Spatial patchiness, individual performance and predator impacts. *Oikos*, 68(3): 560-566
- Goldman, C. R., 1974. Eutrophication of Lake Tahoe emphasizing water quality. U.S. EPA, EPA-660/3-74-034. U.S. GPO.

- Goldman, C.R., 1979, A population dynamics analysis of the cladoceran disappearance from Lake Tahoe, California-Nevada. *Limnology & Oceanography* 24(2): 289-297.
- Goldman, C. R., 1981, Lake Tahoe: Two decades of change in a nitrogen-deficient oligotrophic lake. *Verhandlungen der Internationalen Vereinigung für Theoretische und Angewandte Limnologie* 21: 45-70.
- Heine, K.B., A. Abebe, A.E. Wilson, and W.R. Hood, 2019, Copepod respiration increases by 7% per °C increase in temperature: A meta-analysis. *Limnology & Oceanography Letters*, 4(3): 53-61 <https://doi.org/10.1002/lol2.10106>
- Ikeda, T., 1974, Nutritional Ecology of Marine Zooplankton. *Memoirs of the Faculty of Fisheries Hokkaido University*, 22(1): 1-97.
- Ikeda, T., 1978, The study of metabolic activities of marine zooplankton, with particular emphasis on the relationship to body size. *Journal of the Oceanographical Society of Japan*, 34(4): 173-180
- Jorgensen. 1979. *Handbook of environmental data and ecological parameters*. Environmental Sciences and Applications. Elsevier Ltd.
- Koste, W. 1978. *Rotatoria*. II Tafelband. Berlin, Stuttgart, Gebrüder Borntraeger. 234p.
- Lehtiniemi M, Kiljunen M, & Jones RI. 2009. Winter food utilisation by sympatric mysids in the Baltic Sea, studied by combined gut content and stable isotope analyses. *Marine Biology* 156: 619–628.
- Linden E & Kuosa H. 2004. Effects of grazing and excretion by pelagic mysids (*Mysis* spp.) on the size structure and biomass of the phytoplankton community. *Hydrobiologia* 514(1): 73-78.
- Marshall, S.M. 1973. Respiration and feeding in copepods. *Advances in Marine Biology* 11, 57-120.
- Mauchline, J. 1998. *The Biology of Calanoid Copepods*. Academic Press.
- McCauley, E. 1984. Chapter 7. The estimation of the abundance and biomass of zooplankton in samples. In: Downing, J.A. and Rigler, F.H. (eds.) *A manual on methods for the assessment of secondary production in fresh waters*. 2nd edition. IBP Handbook 17. Blackwell Scientific Publications.
- Richards, R.C., C.R. Goldman, T.C. Frantz & R. Wickwire, 1975. Where have all the *Daphnia* gone? The decline of a major cladoceran in Lake Tahoe. *Verhandlungen der Internationalen Vereinigung für Theoretische und Angewandte Limnologie* 19: 835-842.
- Ross, P.E., and H.C. Duthie, 1978, Preliminary results of an investigation of the phytoplankton, primary production, and ultraplankton-zooplankton dynamics at Matamek Research Station in 1977, pp. 68-78. In *Woods Hole Oceanographic Institution Technical Report*. WH 01 78-92.
- Ross, P.E., and R. Munawar. 1981. Preference for nanoplankton size fractions in Lake Ontario zooplankton grazing. *Journal of Great Lakes Research*, 7(1): 65-67
- Rudstam, L.G., 1989, A bioenergetic model for *Mysis* growth and consumption applied to a Baltic Population of *Mysis mixta*. *Journal of Plankton Research*, 11(5): 971-983 DOI:10.1093/plankt/11.5.971
- Sierszen ME & Brooks AS. 1982. The release of dissolved organic carbon as a result of diatom fragmentation during feeding by *Mysis relicta*. *Hydrobiologia* 93: 155-161.
- Threlkeld, S.T., J.T. Rybock, M.D. Morgan, C.L. Folt, & C.R. Goldman, 1980. The effects of an introduced

- invertebrate predator and food re- source variation on zooplankton dynamics in an ultraoligotrophic lake. American Society Limnology and Oceanography Special Symposium 3: 555-568.
- Uitto, A. 1996. Summertime herbivory of coastal mesazooplankton and metazoan microplankton in the northern Baltic. Marine Ecology Progress Series, 132: 47-56.
- USEPA, 2003. Standard Operating Procedure for Zooplankton Analysis. LG 403.
- Yurista PM. 1999. A model for temperature correction of size-specific respiration in *Bythotrephes cederstroemi* and *Daphnia middendorffiana*. Journal of Plankton Research 21(4): 721-734.
- Wen, Y.H., R.H. Peters. 1994. Empirical models of phosphorus and nitrogen excretion rates by zooplankton. Limnology and Oceanography. 39(7): 1669-1679.
- Winder, M. and D.A. Hunter, 2008. Temporal organization of phytoplankton communities linked to physical forcing. Oecologia 156:179–192.
- Winder, M., J.E. Reuter & S.G. Schladow, 2009. Climate warming favours small-sized pelagic diatoms. Proceedings of the Royal Society B. 276: 427-435.

Lake Clarity Model (1D Model)

- Fleenor, W.E. (2001). Effects and Control of Plunging Inflows on Reservoir Hydrodynamics and Downstream Releases. PhD Dissertation, University of California Davis.
- Lehman, J.T., Bokin, D.B., & Likens, G.E. (n.d.). *The assumptions and rationales of a computer model of phytoplankton population dynamic?* <https://doi.org/10.4319/lo.1975.20.3.0343>
- Hamilton, D.P., Schladow, S.G., (1997). Prediction of water quality in lakes and reservoirs. Part I- model description. Ecological Modelling, 96: 91-110.
- Hirsch, R.M., Moyer, D.L., and Archfield, S.A. (2010). Weighted Regressions on Time, Discharge, and Season (WRTDS), With an Application to Chesapeake Bay River Inputs. *Journal of the American Water Resources Association (JAWRA)*, 46(5), 857–880. <https://doi.org/10.1111>
- Hogan, C.M., Papineau, M., et al. (1987) Development of a dynamic water quality simulation model for the Truckee River, Earth Metrics Inc., Environmental Protection Agency Technology Series, Washington D.C.
- Imberger, J., Patterson, J.C., Hebbert, B., Loh, I., (1978). Dynamics of reservoirs of medium size. Journal of Hydraulic Division, 104: 725-743.
- Imberger, J. and Patterson, J.C. (1981), 'A Dynamic Reservoir Simulation Model –DYRESM: 5', Transport Models for Inland and Coastal Water, pp. 310-361.
- Perez-Losada, J. (2001), A Deterministic Model for Lake Clarity: Application to Management of Lake Tahoe, California-Nevada, PhD Dissertation, University of Girona, Spain.
- Sahoo, G.B., Schladow, S.G., Reuter, J.E. (2010) Effect of Sediment and Nutrient Loading on Lake Tahoe (CA-NV) Optical Conditions and Restoration Opportunities Using a Newly Developed Lake Clarity Model. Water Resources Research, 46, doi:10.1029/2009WR008447.
- Schladow, S.G., Sahoo, G. B., Pyramid Lake Hydrodynamic Modeling Study Report. Report, UC Davis Tahoe Environmental Research Center.

- Sommer, U., Gliwicz, Z. M., Lampert, W. and Duncan, A. (1986). The PEG-model of seasonal succession of planktonic events in fresh waters. *Arch. Hydrobiol*, 106(4), 433–471.
- Sommer, U., Adrian, R., de Senerpont Domis, L., Elser, J. J., Gaedke, U., Ibelings, B., Jeppesen, E., Carlos Molinero, J., Mooij, W. M., van Donk, E. and Winder, M. (2012). Beyond the Plankton Ecology Group (PEG) Model: Mechanisms Driving Plankton Succession. *Annu. Rev. Ecol. Evol. Syst*, 43, 429–477. <https://doi.org/10.1146/annurev-ecolsys-110411-160251>
- Swift, T.J. et al., (2006). Water Quality Modeling in Lake Tahoe: linking suspended matter characteristics to Secchi depth. *Aquatic Sciences*, 68: 1-15.
- Trommer S., S Geoffrey Schladow, & Goloka Behari Sahoo. (2019). Dynamic Lake and Water Quality Model: Pyramid Lake-Technical User Manual DLMPYR 3.0.
- TERC 2021. Tahoe: State of the Lake Report
- Winder, M., Reuter, J.E., and Schladow, S.G. (2008). Lake warming favours small-sized planktonic diatom species. *Proc. R. Soc. B*, 276, 427–435. <https://doi.org/10.1098/rspb.2008.1200>
- Winder, M. (2009). Photosynthetic picoplankton dynamics in Lake Tahoe: temporal and spatial niche partitioning among prokaryotic and eukaryotic cells. *Journal of Plankton Research*, 31(11), 1307–1320. <https://doi.org/10.1093/plankt/fbp074>
- Yeates, P. S., & Imberger, J. (2003). Pseudo two-dimensional simulations of internal and boundary fluxes in stratified lakes and reservoirs. *International Journal of River Basin Management*, 1, 1-23. <http://dx.doi.org/10.1080/15715124.2003.9635214>

Hydrodynamic 3D Model

- Amorocho, J., & DeVries, J. (1980). A new evaluation of the wind stress coefficient over water surfaces. *Journal of Geophysical Research*, 85(C1). <https://doi.org/10.1029/JC086iC05p04307>
- Antenucci, J. P., Imberger, J., & Saggio, A. (2000). Seasonal evolution of the basin-scale internal wave field in a large stratified lake. *Limnology and Oceanography*, 45(7), 1621–1638. <https://doi.org/10.4319/lo.2000.45.7.1621>
- Blumberg, A. (1986). Turbulent Mixing Processes in Lakes, Reservoirs, and Impoundments. In W. G. Gray (Ed.), *Physics-Based Modeling of Lakes, Reservoirs, and Impoundments ASCE* (pp. 79–104). Mahwah.
- Blumberg, A. F., & Mellor, G. L. (1987). A description of a three-dimensional coastal ocean circulation model. In *American Geophysical Union* (pp. 1–16). <https://doi.org/10.1029/CO004p0001>
- Britton, C. M., & Dodd, J. D. (1976). Relationships of Photosynthetically Active Radiation. *Agricultural Meteorology*, 17(1), 1–7.
- Corman, J. R., McIntyre, P. B., Kuboja, B., Mbemba, W., Fink, D., Wheeler, C. W., ... Flecker, A. S. (2010). Upwelling couples chemical and biological dynamics across the littoral and pelagic zones of Lake Tanganyika, East Africa. *Limnology and Oceanography*, 55(1), 214–224. <https://doi.org/10.4319/lo.2010.55.1.0214>
- Dorostkar, A., Boegman, L., & Pollard, A. (2017). Three-dimensional simulation of high-frequency nonlinear internal wave dynamics in Cayuga Lake. *Journal of Geophysical Research: Oceans*, 122(3),

2183–2204. <https://doi.org/10.1002/2016JC011862>

- Gardner, J. V., Mayer, L. A., & Hughs Clarke, J. E. (2000). Morphology and processes in Lake Tahoe (California-Nevada). *Geological Society of America Bulletin*, 112(5), 736–746. [https://doi.org/10.1130/0016-7606\(2000\)112<736:MAPILT>2.0.CO;2](https://doi.org/10.1130/0016-7606(2000)112<736:MAPILT>2.0.CO;2)
- Hodges, B. R., Imberger, J., Saggio, A., & Winters, K. B. (2000). Modeling basin-scale internal waves in a stratified lake. *Limnology and Oceanography*, 45(7), 1603–1620. <https://doi.org/10.4319/lo.2000.45.7.1603>
- Hoyer, A. B., Schladow, S. G., & Rueda, F. J. (2015). A hydrodynamics-based approach to evaluating the risk of waterborne pathogens entering drinking water intakes in a large, stratified lake. *Water Research*, 83, 227–236. <https://doi.org/10.1016/j.watres.2015.06.014>
- MacIntyre, S., & Melack, J. M. (1995). Vertical and Horizontal Transport in Lakes: Linking Littoral, Benthic, and Pelagic Habitats. *Journal of the North American Benthological Society*, 14(4), 599–615. <https://doi.org/10.2307/1467544>
- Martin, J. L., & McCutcheon, S. C. (1999). *Hydrodynamics and transport for water quality modeling*. (S. Wood, Ed.) (Vol. 1). Boca Raton: CRC Press. <https://doi.org/10.1128/AAC.03728-14>
- Murphy, A. H., & Epstein, E. S. (1989). Skill Scores and Correlation Coefficients in Model Verification. *Monthly Weather Review*, 117(3), 572–582. [https://doi.org/10.1175/1520-0493\(1989\)117<0572:SSACCI>2.0.CO;2](https://doi.org/10.1175/1520-0493(1989)117<0572:SSACCI>2.0.CO;2)
- Rao, Y. R., & Schwab, D. J. (2007). Transport and Mixing Between the Coastal and Offshore Waters in the Great Lakes: A Review. *Journal of Great Lakes Research*, 33(1), 202–218. [https://doi.org/10.3394/0380-1330\(2007\)33](https://doi.org/10.3394/0380-1330(2007)33)
- Roberts, D. C., Egan, G. C., Forrest, A. L., Largier, J. L., Bombardelli, F. A., Laval, B. E., ... Schladow, G. (2021). The setup and relaxation of spring upwelling in a deep, rotationally influenced lake. *Limnology and Oceanography*, 66(4), 1168–1189. <https://doi.org/10.1002/lno.11673>
- Rueda, F. J. (2001). *A three-dimensional hydrodynamic and transport model for lake environments*. University of California Davis. University of California Davis.
- Rueda, F. J., & Cowen, E. A. (2005). Residence time of a freshwater embayment connected to a large lake. *Limnology and Oceanography*, 50(5), 1638–1653. <https://doi.org/10.4319/lo.2005.50.5.1638>
- Rueda, F. J., & MacIntyre, S. (2009). Flow paths and spatial heterogeneity of stream inflows in a small multibasin lake. *Limnology and Oceanography*, 54(6), 2041–2057. <https://doi.org/10.4319/lo.2009.54.6.2041>
- Rueda, F. J., & Schladow, S. G. (2003). Dynamics of Large Polymictic Lake. II: Numerical Simulations. *Journal of Hydraulic Engineering*, 129(2), 92–101. [https://doi.org/10.1061/\(ASCE\)0733-9429\(2003\)129:2\(92\)](https://doi.org/10.1061/(ASCE)0733-9429(2003)129:2(92))
- Rueda, F. J., Schladow, S. G., Monismith, S. G., & Stacey, M. T. (2005). On the effects of topography on wind and the generation of currents in a large multi-basin lake. *Hydrobiologia*, 532(1), 139–151. <https://doi.org/10.1007/s10750-004-9522-4>
- Rueda, F. J., Schladow, S. G., & Pálmarrsson, S. Ó. (2003). Basin-scale internal wave dynamics during a winter cooling period in a large lake. *Journal of Geophysical Research*, 108(C3), 3097.

<https://doi.org/10.1029/2001JC000942>

Scheu, K. R., Fong, D., Monismith, S. G., & Fringer, O. B. (2018). Modeling Sedimentation Dynamics of Sediment-Laden River Intrusions in a Rotationally-Influenced, Stratified Lake. *Water Resources Research*, 54(6), 4084–4107. <https://doi.org/10.1029/2017WR021533>

Smagorinsky, J., Manabe, S., & Holloway, J. L. (1965). Numerical Results from a Nine-Level General Circulation Model of the Atmosphere. *Monthly Weather Review*, 93(12), 727–768. [https://doi.org/10.1175/1520-0493\(1965\)093<0727:NRFANL>2.3.CO;2](https://doi.org/10.1175/1520-0493(1965)093<0727:NRFANL>2.3.CO;2)

Smith, P. (2006). A semi-implicit, three-dimensional model for estuarine circulation. *USGS Report*, 176.

TERC 2021. Tahoe: State of the Lake Report

Valbuena, S. A., Roberts, D. C., Cortés, A., Largier, J. L., Bombardelli, F. A., Forrest, A., & Schladow, G. S. (2021). *3D flow structures during upwelling events in rotationally influenced lakes (In Review)*. Davis.

Valipour, R., Rao, Y. R., León, L. F., & Depew, D. (2019a). Electronic Supplementary Material: Nearshore-offshore exchanges in multi-basin coastal waters: Observations and three-dimensional modeling in Lake Erie. *Journal of Great Lakes Research*, 45(1), 50–60. <https://doi.org/10.1016/j.jglr.2018.10.005>

Valipour, R., Rao, Y. R., León, L. F., & Depew, D. (2019b). Nearshore-offshore exchanges in multi-basin coastal waters: Observations and three-dimensional modeling in Lake Erie. *Journal of Great Lakes Research*, 45(1), 50–60. <https://doi.org/10.1016/j.jglr.2018.10.005>

Aquatic Ecological 3D Model

Boegman, L., Loewen, M.R., Culver, D.A., Hamblin, P.F., Charlton, M.N. (2008). Spatial-Dynamic Modeling of Algal Biomass in Lake Erie: Relative Impacts of Dreissenid Mussels and Nutrient Loads. *J. Environ. Eng. ASCE*, 134, 456–468.

Bowie, G., W. Mills, D. Porcella, C. Campbell, J. Pagenkopf, G. Rupp, K. Johnson, and others. (1985). Rates, constants, and kinetics formulations in surface water quality modeling. Tetra Tech, Incorporated. U.S. Environmental Protection Agency. 455p.

Bruce, L., D. Hamilton, J. Imberger, G. Gal, M. Gophen, T. Zohary, and K. Hambright. (2006). A numerical simulation of the role of zooplankton in C, N and P cycling in Lake Kinneret, Israel. *Ecol. Model.* 193, 412–436

Bruce, L.C., Frassl, M.A., Arhonditsis, G.B., Gal, G., Hamilton, D.P., Hanson, P.C., Hetherington, A.L., Melack, J.M., Read, J.S., Rinke, K., et al. (2018). A multi-lake comparative analysis of the General Lake Model (GLM): Stress-testing across a global observatory network. *Environ. Model. Softw.* 102, 274–291.

Chapra, S. C. (1997) *Surface water-quality modeling*. McGraw-Hill, New York, 844p

Chen, C., Ji, R., Schwab, D.J., Beletsky, D., Fahnenstiel, G.L., Jiang, M., Johengen, T.H., Vanderploeg, H., Eadie, B., Budd, J.W. (2002). A model study of the coupled biological and physical dynamics in Lake Michigan. *Ecol. Model.* 152, 145–168

Hamilton, D.P., Schladow, S.G. (1997). Prediction of water quality in lakes and reservoirs. Part I—Model description. *Ecol. Model.* 96, 91–110

Hipsey, M.R., Gal, G., Antenucci, J.P., Zohary, T., Makler, V., Imberger, J. (2006). Lake Kinneret Water

Quality Management System

- Hipsey, M., Bruce, L., Hamilton, D. (2013). Aquatic Ecodynamics (AED) Model Library Science Manual; The University of Western Australia Technical Manual: Perth, Australia, Volume 34.
- Hipsey, M.R., Bruce, L.C., Boon, C., Busch, B., Carey, C.C., Hamilton, D.P., Hanson, P.C., Read, J.S., De Sousa, E., Weber, M. A General Lake Model (GLM 3.0) for linking with high-frequency sensor data from the Global Lake Ecological Observatory Network (GLEON). (2019). *Geosci. Model Dev.*, 473–52
- Hodges, B.R., Imberger, J., Saggio, A., Winters, K.B. (2000). Modeling basin scale waves in a stratified lake. *Limnol. Oceanogr.* 45, 1603–1620
- Jassby, D. (2006), Modeling and microscopy—An attempt to model the particle size distribution of Lake Tahoe particles, MS thesis, 104 pp., Dep. of Environ. and Civil Eng., Univ. of Calif., Davis.
- Leon, L.F., Smith, R.E., Hipsey, M.R., Bocaniov, S.A., Higgins, S.N., Hecky, R.E., Antenucci, J.P., Imberger, J.A., Guildford, S.J. (2011). Application of a 3D hydrodynamic–biological model for seasonal and spatial dynamics of water quality and phytoplankton in Lake Erie. *J. Great Lakes Res.*, 37, 41–53
- Losada, J. P. (2001). A deterministic model for lake clarity. Application to management of Lake Tahoe (California-Nevada), USA. Universitat de Girona.
- Marti CL, Schroth AW, and Zia A. 2019. Physical and biogeochemical processes across seasons in Missisquoi Bay, Lake Champlain: Insights from a three-dimensional model. AGU Fall Meeting, 9-13 December 2019, San Francisco, USA. Oral session. H34C-04
- Missaghi, S. and M. Hondzo. (2010). Evaluation and application of a three-dimensional water quality model in shallow lake with complex morphometry. *Ecol. Model.* 221, 1512-1525
- Pollingher, U., Berman, T. (1982). Relative contributions of net and nano phytoplankton to primary production in Lake Kinneret (Israel). *Arch. Hydrobiol.* 96, 33–46.
- Redfield, A. C. (1958). The biological control of chemical factors in the environment. *Am. Sci.* 46, 205–221.
- Riley, M.J., Stefan, H.G., (1988). MINILAKE: A dynamic lake water quality simulation model. *Ecol. Model.* 43, 155–182
- Romero, J.R., Antenucci, J.P., Imberger, J. (2004). One-and three-dimensional biogeochemical simulations of two differing reservoirs. *Ecol. Model.* 174, 143–160.
- Schladow, S.G., Hamilton, D.P. (1997). Water quality in lakes and reservoirs. Part II—model calibration, sensitivity analysis and application. *Ecol. Model.* 96, 111–123
- Steele, J.H. (1982). Environmental control of photosynthesis in the sea. *Limnol. Oceanogr.* 7, 137-150.
- Swift, T.J., J. Losada, G. Schladow, J. Reuter, A. Jassby, C. Goldman. 2006. Water clarity modeling in Lake Tahoe: Linking suspended matter characteristics to Secchi depth. *Aquat. Sci.* 68, 1–15
- Wang, Q. and L. Boegman. (2021). Multi-year simulation of western Lake Erie hydrodynamics and biogeochemistry to evaluate nutrient management scenarios. *Sustainability* 2021, 13, 7516.